Growth and characterization of high-quality bulk hexagonal boron nitride crystals

by

Jiahan Li

B.S., Wuhan University, 2002
PhD, Wuhan University, 2012

AN ABSTRACT OF A DISSERTATION

Submitted in partial fulfillment of the requirements for the degree

DOCTOR OF PHILOSOPHY

Department of Chemical Engineering
Carl R. Ice College of Engineering

KANSAS STATE UNIVERSITY
Manhattan, Kansas

2019

Abstract

While hexagonal boron nitride (hBN) in polycrystalline form has met demand for its mechanical, chemical, and thermal applications, its new electronic, optoelectronic, and nanophotonic applications required single crystals with low residual impurity concentrations. Grain boundaries and impurities need to be minimized, as they degrade the properties of hBN that are important for these new applications. The present study was undertaken to develop large area, high quality hBN single crystals at low cost, and with control over its boron isotope concentrations. Furthermore, a preliminary study was undertaken to determine if the properties of hBN could be advantageously altered by irradiation.

In this study, four processes to grow and manipulate the properties of hBN single crystals were developed. First, high-quality hBN crystals were grown from an iron metal flux. The quality of crystals produced by this novel, low cost and high purity solvent was equivalent to the best reported in the literature, as verified by Raman spectroscopy, photoluminescence, defect density assessment, and current-voltage measurements. Second, hBN crystals were grown via temperature gradient method with iron-chromium flux. This method has the potential to produce larger, higher quality crystals than the slow cooling method. The maximum crystal domain size was up to 4 mm. Both in- and out-plane thermal conductivity was significantly higher than the hBN grown by slow cooling, indicating improved crystallinity. Third, monoisotopic boron hBN ($h^{10}BN$ and $h^{11}BN$) was grown from both Fe and Fe-Cr fluxes. Raman and photoluminescence spectra show the quality of crystal grown from Fe and Fe-Cr fluxes was comparable. Fourth, neutron transmutation doping was studied as a possible method of altering the electrical and optical

properties of hBN single crystals. Raman spectroscopy, photoluminescence, and electron paramagnetic resonance spectroscopies established that the effects of neutron irradiation were more pronounced on $h^{10}BN$ than $h^{11}BN$. Together, these studies demonstrate the versatility of methods available to produce high quality hBN single crystal with specific properties.

Growth and characterization of high-quality bulk hexagonal boron nitride crystals

by

Jiahan Li

B.S., Wuhan University, 2002
PhD, Wuhan University, 2012

A DISSERTATION

Submitted in partial fulfillment of the requirements for the degree

DOCTOR OF PHILOSOPHY

Department of Chemical Engineering
Carl R. Ice College of Engineering

KANSAS STATE UNIVERSITY
Manhattan, Kansas

2019

Approved by:

Major Professor
James H. Edgar

Copyright

Abstract

While hexagonal boron nitride (hBN) in polycrystalline form has met demand for its mechanical, chemical, and thermal applications, its new electronic, optoelectronic, and nanophotonic applications required single crystals with low residual impurity concentrations. Grain boundaries and impurities need to be minimized, as they degrade the properties of hBN that are important for these new applications. The present study was undertaken to develop large area, high quality hBN single crystals at low cost, and with control over its boron isotope concentrations. Furthermore, a preliminary study was undertaken to determine if the properties of hBN could be advantageously altered by irradiation.

In this study, four processes to grow and manipulate the properties of hBN single crystals were developed. First, high-quality hBN crystals were grown from an iron metal flux. The quality of crystals produced by this novel, low cost and high purity solvent was equivalent to the best reported in the literature, as verified by Raman spectroscopy, photoluminescence, defect density assessment, and current-voltage measurements. Second, hBN crystals were grown via temperature gradient method with iron-chromium flux. This method has the potential to produce larger, higher quality crystals than the slow cooling method. The maximum crystal domain size was up to 4 mm. Both in- and out-plane thermal conductivity was significantly higher than the hBN grown by slow cooling, indicating improved crystallinity. Third, monoisotopic boron hBN (h^{10}BN and h^{11}BN) was grown from both Fe and Fe-Cr fluxes. Raman and photoluminescence spectra show the quality of crystal grown from Fe and Fe-Cr fluxes was comparable. Fourth, neutron transmutation doping was studied as a possible method of altering the electrical and optical

properties of hBN single crystals. Raman spectroscopy, photoluminescence, and electron paramagnetic resonance spectroscopies established that the effects of neutron irradiation were more pronounced on h^{10}BN than h^{11}BN. Together, these studies demonstrate the versatility of methods available to produce high quality hBN single crystal with specific properties.

Table of Contents

List of Figures

List of Tables

Acknowledgements

I want to thank several people who made this project possible. First, I thank my advisor, Dr. James Edgar; without his ideas and patience, this project and my educations would not have been possible. I hope that this work benefits future students studying hexagonal boron nitride in the Edgar group.

Thanks to my committee members, Dr. Christine Aikens, Dr. Bin Liu, Dr. John Schlup and Dr. Gurpreet Singh. Their suggestions and imputs helped me to improve this work.

Thanks to the graduate students in the Edgar group, Timothy Hoffman, Song Liu, Hayder Al-Atabi and Eli Janzen. Hayder was very busy, but he sacrificed his time to help on this project without complaint.

I want to thank my undergraduate assistant, Dylan Evans. He did vital work for this project. I hope that he will continue his research and education at KSU.

I want to thank researchers who I collaborated with outside of the department, including Dr. Rui He of Texas Tech University, who did Raman spectra measurements; Christine Elias, Dr. Guillaume Cassabois, Dr. Bernard Gil and Dr. Pierre Valvin of Université de Montpellier, who performed photoluminescence measurements; Junyong Wang and Dr. Goki Eda of National University of Singapore, who fabricated hBN devices; Xiaotian Zhang and Dr. Joan Redwing of The Pennsylvania State University, who deposited WSe_2 on my hBN crystals; Chao Yuan and Dr. Martin Kuball of the University of Bristol, who did the thermal conductivity measurements; Dr. Evan Glaser at the US Naval Research Laboratory, who took EPR spectra and did a lot of analysis to my benefit; and Dr. Susan White of The Ohio State University, who did neutron irradiation doping.

Thanks to David Threewit of the KSU Chemical Engineering Department, James Hodgson of the KSU Chemistry Department, and Chris Aikens of the KSU Physics Department, who solved a lot of technical problems.

A hearty thanks to all!

Dedication

I dedicate this work to my wife, Xiaorong Liu. She is always supporting me without complaint. I also dedicate this work to my friends, Jiaxin Dong, Yu Sun and Zhou Yu. Without your support, this would not have been possible. Thank you.

Chapter 1 - Motivation

As an graphene-analogue, hexagonal boron nitride (hBN) has may applications, including a substrate for nanoelectronic devices,[1] an encapsulant for other 2D materials,[2] and a platform for nanophotonic hyperbolic devices,[3] deep ultraviolet light emitters[4] and single photo emitters.[5-7] Monoisotopic hBN with a single boron isotope instead of the two as found in natural boron has enhanced properties and additional applications including heat management,[8] nanophotonics,[9-12] and thermal neutron detection.[13] To realize the best device performance, hBN single crystals with few structural imperfections are required. This study not only produced hBN crystals for optoelectronics and nanophotonics that requires the best quality materials, but also provided a source material for defect engineering to achieve desired properties.

This dissertation investigates the growth of high quality hBN crystals using metal flux method. It is organized into seven standalone chapters that each focus on a specific topic. Chapter 2 introduces the properties, applications, and characterization method of hBN. This provides the background for understating the subsequent chapters.

Chapter 3 describes hBN single crystal growth using pure iron. Iron is a novel, simple, single component solvent that hasn't been used previously for hBN crystal growth. Iron is also inexpensive and available in higher purities (lower carbon concentrations) than nickel. Raman spectroscopy and photoluminescence spectra revealed that the resulting hBN were equal to the highest quality crystals reported in the literature. The hBN has a low defect density. The hBN crystals were up to 3 cm^2 in area.

Chapter 4 demonstrates the growth of hBN using a temperature gradient along the length of the solvent. The goal was to dissolve source material in the hot zone and

precipitate crystals in the cool zone. Prior studies used uniform cooling of the solvent which leads to crystals forming over a wide range of temperatures. The temperature gradient method has the potential to grow larger, higher quality crystals than the slow cooling method previously used. Raman spectroscopy and photoluminescence spectra showed that the hBN was highly crystalline. The high thermal conductivity of crystals produced in this manner higher than crystals grown by uniform cooling, suggesting revealed that they had few defects.

Chapter 5 discusses the growth of monoisotopic hBN from both Fe and Fe-Cr fluxes. These were both new solvents that had not previously been used with pure boron source of ^{10}B and ^{11}B. Iron solvent is inexpensive and available in higher purities (lower carbon concentrations) than chromium. The goal of chapter 5 was to investigate the solvent effects on hBN quality. Raman spectroscopy and photoluminescence spectra showed that the crystal quality grown from both Fe and Fe-Cr fluxes was comparable.

Chapter 6 achieved the defect engineering of hBN single crystal using neutron transmutation doping. The goal was to alter the electronic and optical properties of hBN by introducing point defects and impurities into highly crystalline hBN single crystals. hBN is a wide-bandgap semiconductor with fixed optical and electrical properties, which limits its applications in some electronic and optoelectronic devices. Neutron transmutation doping has the potential to produce boron vacancies and lithium doping. As expected due to ^{10}B stronger neutron absorption than ^{11}B, The neutrons damage the h^{10}BN much more strongly than h^{11}BN. Electron paramagnetic resonance spectra suggests that neutron-irradiation produces boron vacancies. Annealing helped to recover the properties of hBN.

Chapter 2 - Properties, applications, and characterization of hexagonal boron nitride

Hexagonal boron nitride (hBN) is a structural analogue of graphite, but with vastly different properties. Traditionally, hBN has been widely used in applications exploiting its excellent thermal and chemical stability,[14] high thermal conductivity,[15] lubricity[16] and corrosion resistance[17] in high temperature and oxidative environments.[18] For those established applications, polycrystalline hBN is sufficient. Recently, hBN single crystals have gained attention for their potential applications, including solid state semiconductor devices, such as deep ultraviolet emitters[19], substrates and dielectrics for graphene transistors[20-23] and high-efficiency solid state neutron detectors.[24] These new applications demand high quality crystals that are large in area and thickness.

This chapter provides an overview of the properties and applications of hBN. Common techniques to characterize the quality of hBN such as Raman and photoluminescence spectra are introduced. Prior studies on the growth of hBN single crystal from metal fluxes are also reviewed.

Boron nitride compound

Boron nitride bond forms multiple structures that have various atom arrangements: amorphous form (a-BN), wurtzite form (wBN), cubic form (cBN) and hexagonal form (hBN). Among them, aBN is non-crystalline. The crystal structure of cBN, with sp3 bonding, is similar to diamond (Figure 2.1). In the cBN all rings are in the chair configuration. However, the rings with boat configuration in wBN (Figure 2.2). Besides these, boron nitride bonds can form nano-structures such as single-wall BN-nanotubes (Figure 2.3)[25] and multiply-wall BN-nanotubes.[26-28]
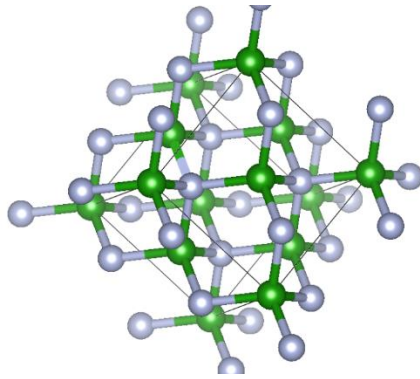
Figure 2.1 Structure of cBN.
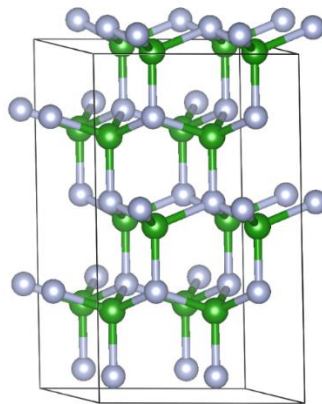
Figure 2.2 wBN structure
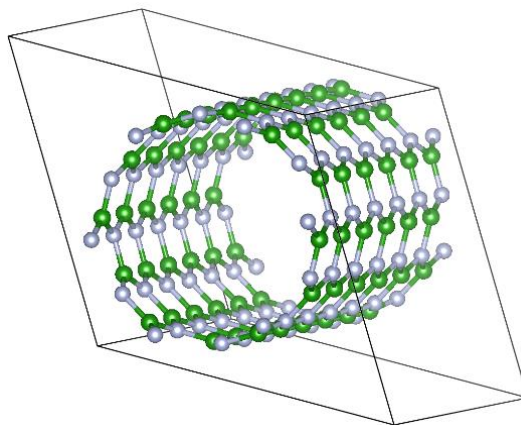
Figure 2.3 Single-wall boron nitride nanotube structure

Properties of hexagonal boron nitride

Hexagonal boron nitride (hBN) is a two-dimensional material with the honeycomb crystal structure (as illustrated in Figure 2.4). Each plane of hBN is composed of boron and nitrogen atoms with strong sp^2 hybridization bonds. Bonding between layers is weaker Van der Waals interactions. The intralayer interaction between B and N is a polar covalent bond; this leads to Coulomb interactions between atoms located in neighboring layers. Therefore, the energetically favorable structure of hBN is AA' stacking: the nitrogen atom (green color) in the upper layer is above the boron atom (gray color) in the lower layer.[29] The atomic weight of boron is 10.811 g/mol, and nitrogen is 14.007 g/mol, thus hBN is a light, low density 2.1 g/cm^3 (Table 2.1) material. The strong sp^2 hybridization bond of B-N atoms imparts it with a high melting temperature. Because of the different chemical bond types, high strength sp^2 bonds in-plane and the weaker Van der Waals interaction between planes, single crystal hBN has highly anisotropic properties. For example, its thermal conductivity in the *c*-direction is approximately 1/133 times that in the *a*-direction.
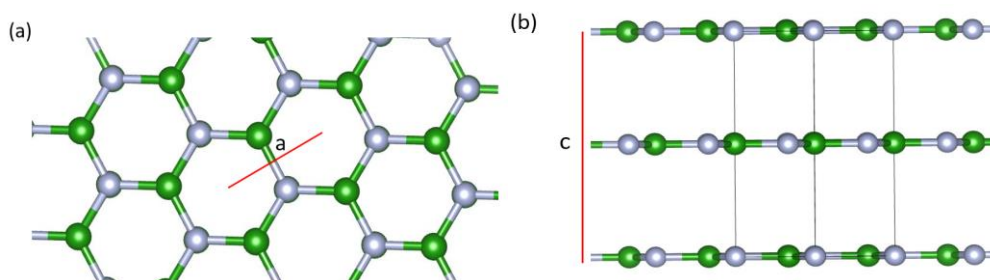
Figure 2.4 hBN crystal structure. The structure file is downloaded from Crystallography Open Database. Boron and nitrogen atoms are represented by green and gray spheres, respectively. (a) top view, (b) side view. The honeycomb crystal structure and AA' stacking can be seen clearly from Figure (a) and (b), respectively.

hBN is electrically insulating. Thin hBN layers show a tunneling behavior. Figure 2.5 illustrates a three layers metal-insulator-metal junction diode with hBN.[30] At direct

current bias voltage (V_{dc}) < ±100 mV, the current-voltage curves show a linear ohmic dependence. At higher bias voltage, the I−V characteristics demonstrates nonlinearity. The breakdown electric field for crystalline hBN 8-15 nm thick was between 2 and 4 MV cm^{-1}.[31]

Table 2.1 Physical properties of hBN.

Property	Value
Melting point (°C)	3000
Thermal conductivity (W/mK) at 300K	ab axis: 408. c axis:3.3.[32]
Energy bandgap(eV)	5.9(indirect)
Young's modulus (TPa)	1.16 [31]
Density(g/cm^3)	2.1 [29]
Resistance temperature to oxidation (°C)	1000[33]
Optical color	colorless
Resistivity(Ω)	$10^8 \sim 10^{13}$ [29]
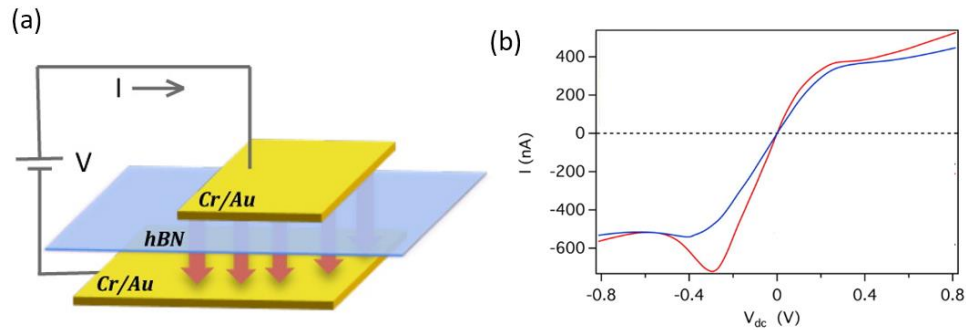
Figure 2.5 (a) Schematic for an exfoliated hBN tunnel devices with Cr/Au electrodes. (b) Tunnel current (I) as a function of dc bias (V_{dc}) for a typical thin hBN device with 3 layers. Reprinted with permission from reference[30]. Copyright (2015) American Chemical Society.

In addition to nanoelectronics, thin hBN layers also possess interesting properties that are useful for nanophotonics. As a natural hyperbolic material, hBN can produce

6

phonon polaritons. [34] Quasiparticles are generated in polar medium because of the coupling

of photons with lattice vibrations. Through this coupling, the wavelength of light can be

compressed by more than a factor of one hundred. This offers the promise of a broad range

of applications, including photodetection, color filters and optomechanics.[35] Hyperbolic

phonon polaritons can be observed in hBN with a scattering-type scanning near-field

optical microscope image because of propagating electromagnetic waves. Figure 2.6

illustrates this method.[36] In this technique, an atomic force microscopy tip conveys the

energy of the incident photons and launches polaritons in the hBN. The polaritons

propagate in the hBN and are observed as periodic oscillations (fringes).
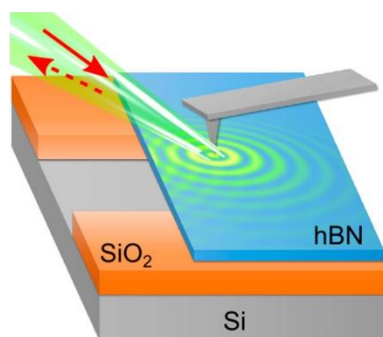
Figure 2.6 Schematic of how hyperbolic phonon polaritons are imaged in hexagonal boron nitride. A hBN flake was transferred onto the Si/SiO_2 substrate with an air trench such that part of the hBN was suspended. The polaritons were launched by indent laser beam (red solid arrow). The backscattered IR signal was (red dashed arrow) collected. Reprinted with permission from reference[36]. Copyright (2018) American Chemical Society.

Applications of hexagonal boron nitride

Polycrystalline hBN has been widely used for diverse applications, such as heat resistant crucibles because of its high thermal and chemical stability and insulators or thermocouple protectors because of its high electrical resistivity. hBN is also an excellent oxidation-resistant coating. Zheng et al.[37] demonstrated that an ultrathin hBN layer coating resists oxidation up to 1,100 °C in oxygen.

In addition to tunnel layer in nanoelectronics and polariton-generation in nanophotonics, highly crystalline hBN has other potential applications.

Deep ultraviolet emission. The bandgap of hBN is about 5.9 eV, which corresponds to the wavelength of 210 nm. Therefore, hBN is of interest for deep ultraviolet emission (wavelengths from 280 to 198 nm) devices.[38] Despite having an indirect bandgap, hBN's luminescence efficiency is quite high. Watanabe et al. [39] fabricated a battery-driven far-ultraviolet plane-emission device based on hBN, with output power of 0.2mW at 225 nm.

Substrate for graphene-based devices. hBN and graphene have a similar crystal structure and a small lattice constant mismatch. The a-lattice constants for hBN and graphene are very similar (2.5 Å and 2.46 Å, respectively). Hence, hBN is a good substrate for sp^2 hybridization graphene-based devices.[40-42] Compared to SiO_2, the most common substrate used with graphene, the charge concentration fluctuations were reduced by two orders of magnitude on hBN.[43] Traditional graphene devices use SiO_2 as the insulating substrate but it has some disadvantages, such as a rough substrate surface, dangling bonds, and it contains impurities that adversely affect the properties of graphene, so the graphene devices exhibit poor performance. In contrast, hBN is a much better substrate: it is

smoother and has lower interface trap densities. Wang *et al.*[44] fabricated graphene devices on hBN substrates exhibiting mobility up to 140,000 cm^2/Vs at room temperature. For comparison, for graphene on SiO_2, the value was 4500 cm^2/Vs.[45]

Single photon emitter. Single photon emitter emits one photon at a time. This is useful to control the photon's quantum properties for information storage and transmission.[46] Single photon emitters have been produced by atomic defects in hBN at room temperature.[47, 48] The are extremely robust, stable and spectral tunable, which makes hBN a promising platform for quantum information processing devices.

Neutron detector. hBN is also potentially useful as a high-efficiency neutron detector material, due to the ^{10}B isotope's large thermal neutron absorption cross section.[49] Natural boron has two isotopes: the ^{10}B content is around 20% and the remainder is ^{11}B. If a neutron is captured by ^{10}B atom, the nuclear reactions are: [49]

$$^{10}B + {}_0^1n \rightarrow {}^7Li\,(1.015\text{ MeV}) + \alpha\,(1.777\text{ MeV}) \quad 6\%$$

$$^{10}B + {}_0^1n \rightarrow {}^7Li^*\,(0.840\text{MeV}) + \alpha\,(1.470\text{MeV}) \quad 94\%$$
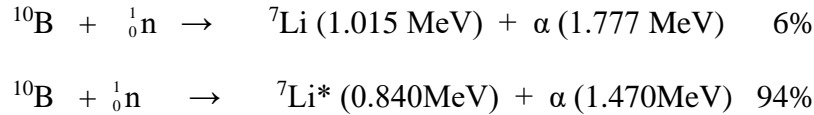
The energetic α particles and ^{7}Li ions produce electron-hole pairs by inelastic scattering. Thermal neutron detectors based on hBN can capture neutrons, generate charge, and produce an electrical signal in one single layer. Therefore, hBN neutron detectors are expected to possess many advantages: low leakage currents, low gamma sensitivity and fast response, and the ability to be fabricated in large areas.[50]

To capture neutrons and generate a signal requires high quality, large area, thick hBN single crystals. For example, the thermal neutron absorption length in natural hBN layer is around 230 µm. With ^{10}B enriched hBN, the thickness needed to capture all neutrons is less, approximately 90 µm.[24]

Substrate for 2D materials growth. hBN is an ideal substrate for 2D material growth because of its excellent physical and chemical stability and atomically smooth surface, which is free of dangling bonds. hBN has been used as a substrate for a wide variety of thin films including graphene,[51] MoS_2,[52] $MoSe_2$,[53] and black phosphorus as examples. On hBN, the quality of 2D materials is consistently better than other materials: they have higher electron mobilities and more intense, narrower photoluminescence peaks.[54] Zhang *et al.*[54] reported that a hBN single crystal substrate orientates the growth of WSe_2. Single-atom vacancies on the hBN surface trap W atoms, leading to a reduced formation energy for WSe_2 domains. Compared to traditional sapphire substrate, the nucleation density of WSe_2 on hBN substrate is much lower (Figure 2.7).

Heat management layer in nano-electronics. With the rapid development of nano-scale integrated circuits, high power becomes confined to smaller and smaller volumes. Hot spots can develop which can degrade the devices performance until it ultimately fails. To avoid this, efficient heat removal is highly desired. The in-plane thermal conductivity of bulk hBN is 408 ± 60 W m^{-1} K^{-1} at room temperature. This value is several hundred times higher than SiO_2 (1.1 W m^{-1} K^{-1}).[55] In contrast, the cross-plane thermal conductivity (TC) of bulk hBN is around 3.3 ± 0.8 W m^{-1} K^{-1}. The thermal conductivity of hBN with a single boron isotope is even higher. For boron-monoisotopic hBN, due to reduced phonon scattering, the room-temperature in-plane thermal conductivity of h^{10}BN and h^{11}BN are 585 ± 80 and 550 ± 75 W m^{-1} K^{-1}.[32] In contrast, the cross-plane thermal conductivity of h^{10}BN and h^{11}BN are 3.5 ± 0.8 and 4.5 ± 0.8 W m^{-1} K^{-1}, respectively. This anisotropic thermal conductivity makes hBN a great candidate for heat management layer in nano electronics. Figure 2.8 is a schematic showing how hBN

works as a heat dissipation layer. Figure 2.8a shows that heat flow (black arrow) can dissipate both laterally (along the surface of the SiO_2 substrate) and vertically (into the SiO_2 substrate). However, if hBN film coated on the SiO_2 substrate (Figure 2.8b), the heat flow mainly dissipates between source and drain due to high in-plane TC. The heat spreading in the vertical direction is decreased due to low cross-plane TC.
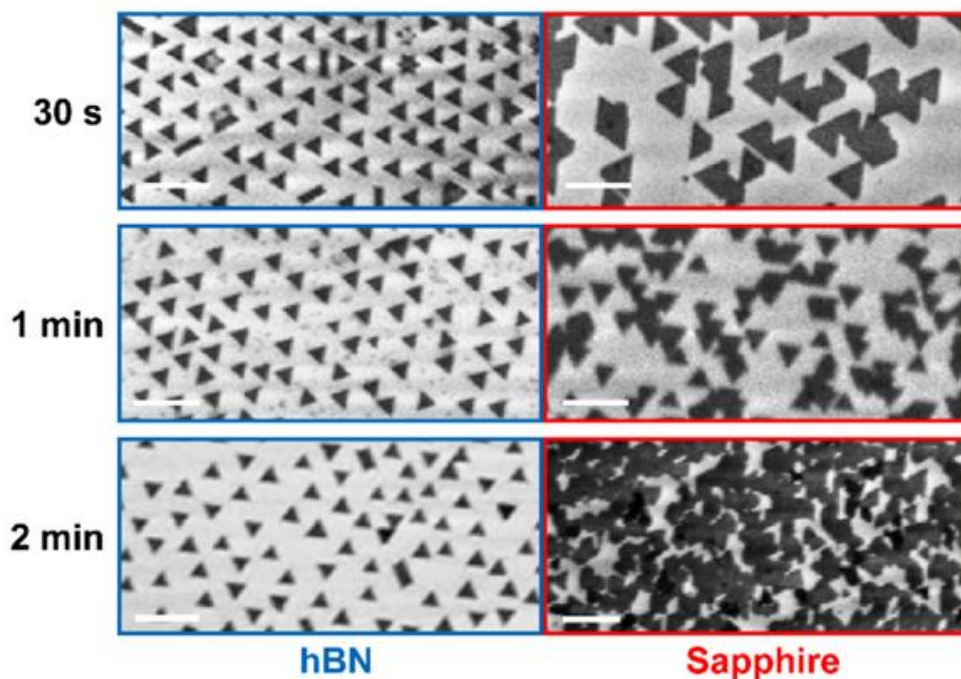
Figure 2.7 SEM images of WSe_2 grown on different substrates: hBN (left) and sapphire (right). Nucleation time were 30 s, 1 min, and 2 min. Scalebar is 1μm. Reprinted with permission from reference[56]. Copyright (2019) American Chemical Society.
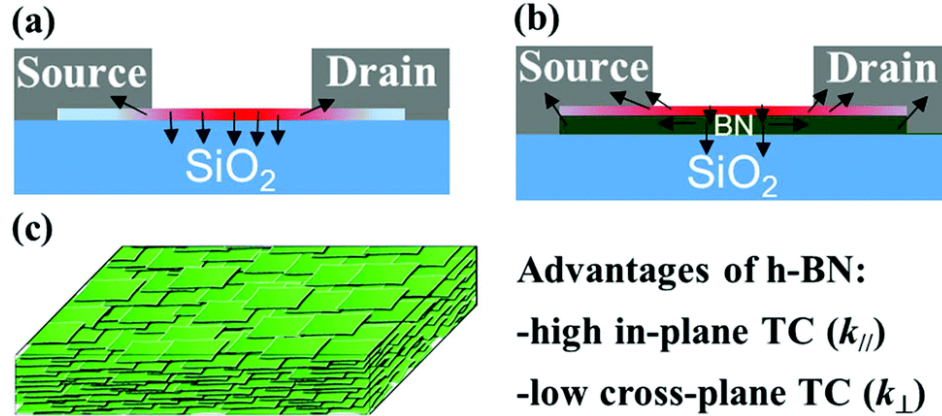
Figure 2.8 Schematic of hBN film as a thermal management material. (**a**) Heat generated on a SiO$_2$ substrate. (**b**) Heat generated on a hBN thin film coated SiO$_2$ substrate. (**c**) hBN thin film comprised of layer-by-layer laminated h-BN nanosheets. Reproduced with permission from reference[57], the Royal Society of Chemistry.

Characterization of hBN

The goal of characterization is to assess the quality of the material and to measure its properties (electrical, optical, thermal, mechanical, etc.), often when it is combined with other materials. This is necessary to determine if the material has the properties needed for a specific device function. Scientific studies of hBN properties and the development of technological application require excellent characterization of the material to understand its properties. In this regards, Raman and photoluminescence spectra are especially important tools for characterizing hBN.

Raman spectroscopy

Raman spectroscopy is widely used to characterize semiconductor materials and their crystal quality. In a Raman measurement, the inelastically scattered light is analyzed. Suppose $\hbar$ is the Planck constant, and v_i , v_s, and v_p are the frequencies of incoming

photons, scattered photons, and phonons, respectively. A photon of energy $\hbar\,\upsilon_i$ is scattered by a phonon of energy $\upsilon_p\hbar$, resulting in the energy of the scattered photon being

$$\hbar\upsilon_s = \hbar\,\upsilon_i \pm \hbar\,\upsilon_p.$$

Phonon absorption corresponds to the positive sign, while the phonon excitation corresponds to the negative sign. The Raman shift is the energy difference between the incoming and scattered energy. Numerically, it is defined as the reciprocal difference of the wavelength between of the incident and scattered light. From the above equation, we derive that the Raman shift is proportional to the energy of the excited (or absorbed) phonons.

Three parameters (the peak intensity, peak position and full width at half maxima (FWHM)) can be used to evaluate the properties of hBN. The peak intensity increases with the number of hBN layers. Figure 2.9 shows an example of this.
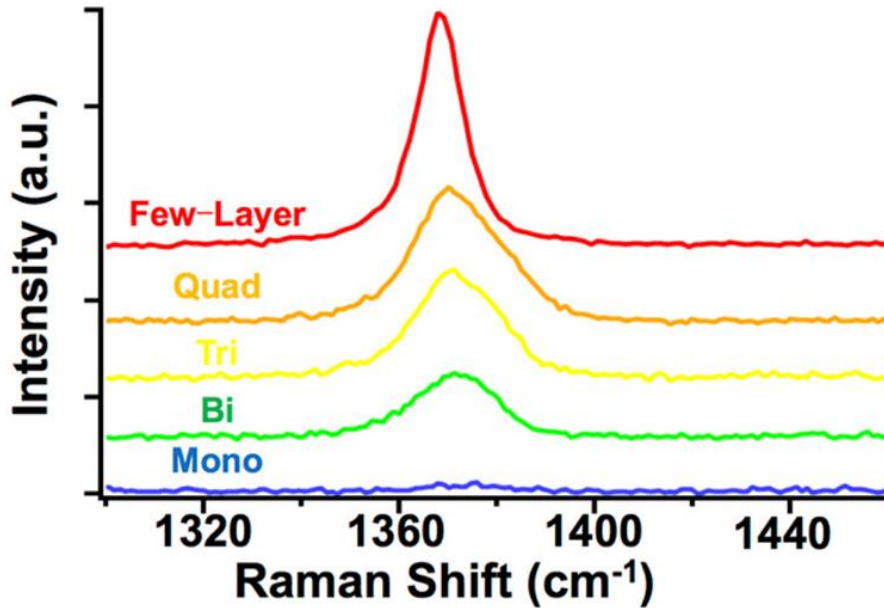
Figure 2.9 Raman spectra of hBN as a function of the atomic layer number. Reprinted with permission from reference[58]. Copyright (2017) American Chemical Society.

The peak position is the most straightforward way to determine if hBN is present. hBN exhibits two primary vibrational modes: an in-plane mode at high frequency and an interlayer mode at low frequency (Figure 2.10). The E_{2g} lattice vibration peak corresponds the B and N atom in-plane stretching vibrations.[59] Two factors influence this peak position: (a) the number of layers and (b) strain (a built-in stretching of bonds). For bulk hBN, the E_{2g} peak position is at 1366 cm^{-1}.[59] For low-quality hBN films constrained by substrate, the peak position shifts due to strain. For monolayer hBN, the peak is at 1369 cm^{-1}.[60] There was a red shift of bilayer peak position to monolayer (Figure 2.9) because monolayer hBN has a slightly shorter bond between boron and nitrogen, inducing a hardening of the E_{2g} vibration.
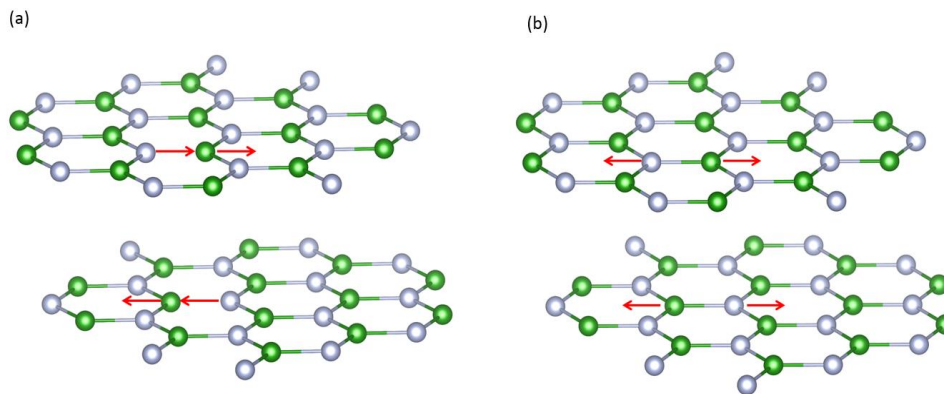
Figure 2.10 Two vibration modes of hBN crystal. (a) Shear mode. For bulk natural hBN, the peak position is at 52.5 cm^{-1}. (b) In-plane mode (E_{2g}). For bulk natural hBN, the peak position is at 1366 cm^{-1}.[61]

The full width at half maximum (FWHM) of the Raman peak can indicate the quality of the hBN crystal: the width increases with the defect density. For hBN synthesized by chemical vapor deposition, the FWHM of the E_{2g} peak is typically more than 20 cm^{-1}.[62]

The best value for CVD-hBN was 14 cm^{-1} (Figure 2.11).[60] For high quality bulk natural

hBN crystals, the smallest Raman FWHM was 7.8 cm^{-1} (Figure 2.12).[59]
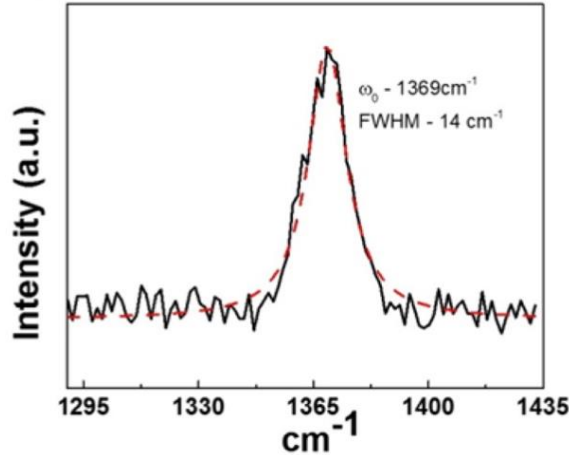
Figure 2.11 Raman spectra of a high-quality monolayer hBN grown by CVD method. Reprinted with permission from reference[60]. Copyright (2015) American Chemical Society.

Isotopically pure hBN has different Raman peak positions. Since the B-N

vibrational frequency in plane is proportional to $\sqrt{\frac{1}{m_B} + \frac{1}{m_N}}$, then the smaller atomic mass

of h^{10}BN has a larger phonon energy than h^{11}BN. As shown in Figure 2.12, the E$_{2g}$ peak

of h^{10}BN and h^{11}BN single crystal are at 1393.3 and 1357.4 cm^{-1}, respectively.[59] The

FWHM in h^{10}BN and h^{11}BN are 3.1 and 3.3 cm^{-1} ; both values are much smaller than

natural abundance hBN (7.8 cm^{-1}) because there is no isotopic mass fluctuation to interrupt

the translational symmetry significantly and elastically scatter the phonons.[63]
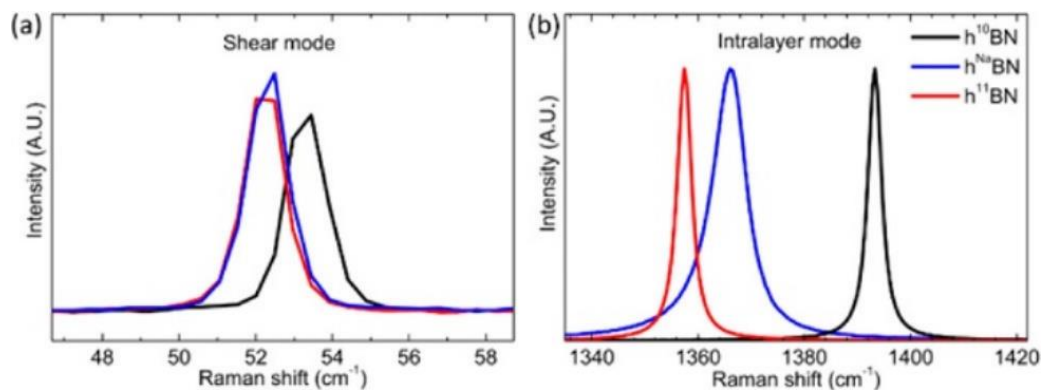
Figure 2.12 Raman spectra of the (a) shear mode and (b) intralayer mode from h^{10}BN, h^{11}BN and hBN crystals grown with a Ni-Cr metal flux. Reprinted with permission from reference[59] . Copyright (2018) American Chemical Society.

Photoluminescence spectroscopy

Photoluminescence (PL) spectroscopy is a non-destructive optical method to characterize the opto-electronic property of a semiconductor, including its energy bandgap and energy states introduced by impurities or defects. In a PL process, a semiconductor is excited by a photon to produce electron-hole pairs. As the electrons and holes undergo relaxation, they recombine by emitting a photon. Because the relaxation favors low energy states, a low concentration of impurities can produce a significant PL characteristic signal. PL spectra is most informative when taken at cryogenic temperature, because high temperatures tend to broaden the peaks thermally, making the details of the energy level unobservable.[64] Defects and impurities can be detected, because they create new energy levels within the forbidden gap.[65-67] Like Raman spectroscopy, as an optical method, no complicated sample preparation is required for collecting PL spectra.
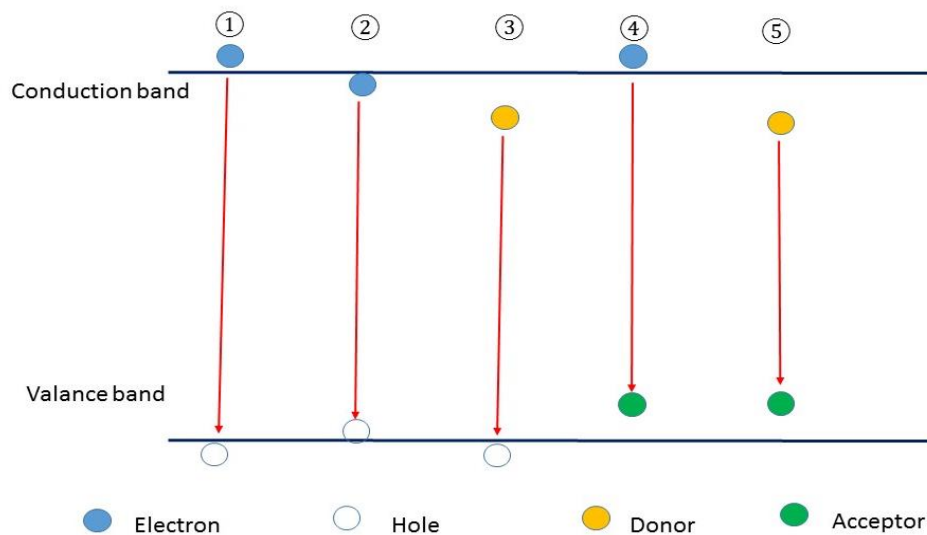
Figure 2.13 Schematic figure of electronic transitions in photoluminescence.

As shown in Figure 2.13, the photon energy emitted depends on the radiative recombination mechanism: (1) conduction band to valence band recombination. (2) Free exciton recombination. Electron-hole pairs are bound to each other due to Coulombic interaction. The energy is smaller than the energy band gap. (3) A hole combines with a neutral donor. (4) An electron combines with a neutral acceptor. (5) A donor interacts with an acceptor.

Direct and indirect semiconductors have different PL features. A direct bandgap semiconductor such as WS_2 has efficient direct radiative recombination. Therefore, photoluminescence spectra of high-quality WS_2 crystal show a strong intrinsic peak, as seen in Figure 2.14.[68] A strong and sharp peak at 2.0 eV indicates the good crystallinity.
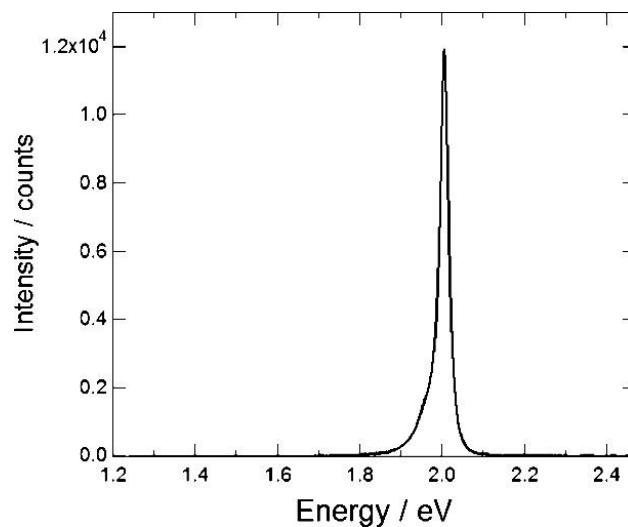
Figure 2.14 A PL spectrum of WS$_2$. Reprinted with permission from reference[68]. Copyright (2014) American Chemical Society.

Bulk hBN is an indirect bandgap semiconductor. [69] Radiative recombination requires assistance by phonon scattering because both energy and momentum must be conserved. Considering the interaction between the intrinsic phonon-assisted recombination and the extrinsic defect-related emission processes, the presence of phonon-assistant peaks indicates highly crystalline hBN.[70] As shown in Figure 2.15, hBN has four radiative recombination peaks assisted by the emission oschsf phonons at 5.76, 5.79, 5.86 and 5.89 eV, indicating the high quality of hBN crystal.[70]
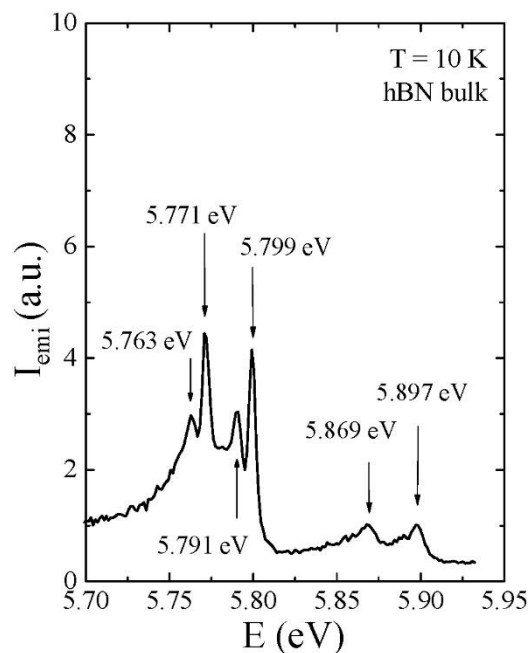
Figure 2.15 PL spectra of bulk hBN. Reproduced from [71], with the permission of AIP Publishing.

The defect-related emission peak centered at 5.5 eV corresponds to the transverse optical phonon-assisted inter-K valley scattering. The presence of stacking faults in bulk hBN provide a density of final electronic states to make this peak observable.[70] The broad peak at 4 eV is attributed to a donor-acceptor transition, due to the presence of vacancies or impurities such as carbon or oxygen.[72]

hBN film synthesis

While the compound hBN can be produced by many techniques, there are only a few methods capable of producing hBN single crystals. Chemical vapor deposition, molecular beam epitaxy and sputter deposition were used to synthesize hBN films, while the metal flux method was used to grow hBN bulk crystals. These methods will be reviewed briefly.

Chemical vapor deposition.

In chemical vapor deposition (CVD) boron and nitrogen precursors reacts at the surface of a heated substrate to form hBN.[73] As a scalable method, CVD has the ability to produce large area films, to control the thickness of film, and to create van der Waals heterostructures. Various transition metals such as Ni,[74, 75] Ru,[76] Cu,[77, 78] and Ag,[79] as well as single crystal sapphire[80, 81] have been used as substrate to produce large-area monolayers hBN. Besides pure metals, alloys have also been investigated as substrates. In general, CVD produces the hBN with relatively small size (100 µm) grain.[82] Recently, two significant results on large-area hBN monolayer were reported Lee et al. synthesized wafer-scale single-crystal hBN film via self-collimated grain formation. [83] Boron and nitrogen atoms in liquid gold at high temperature form the circular hBN grains. These grains evolve single-crystalline film on a wafer scale by self-collimation of B and N edges due to electrostatic interaction between grains. Wang *et al.*[84] achieved CVD epitaxial growth of a 100-square-centimetre single crystal hBN monolayer on copper.

Even though CVD can produce large-area thin films, their quality does not match that of bulk hBN crystals. Raman characterization shows that the quality of CVD produced hBN decrease with the layer thickness: typically, the Raman peak widths are 13 to 24 cm^{-1},[58, 73, 85, 86] which is significantly wider than metal-flux grown bulk hBN (8 cm^{-1}). The hBN structure changes when the hBN layer thickness increases: Henry *et al.* [87] reported that BN films changed from hBN to rhombohedral BN when film thicknesses reach 4 nm. Thus, the challenge remains to improve control of thick- film structural quality.

Molecular beam epitaxy

In MBE, elemental boron is evaporated using evaporation source such as e-beam, and a nitrogen flux is introduced by a plasma source.[88] The boron and nitride elements deposited and combined together to form hBN on the substrate. High purity of hBN can be achieved because of the absence of carrier gases or precursors.

MBE can produce hBN layers of high quality, indicating by the presence of phonon-assisted peaks[89] and narrow Raman peak (FWHM of 13 cm^{-1}).[90] While better than CVD films, MBE has not achieved the quality of comparable to bulk hBN.

Sputter deposition

Compare to hBN CVD, less research has been reported on sputter deposition because it is generally difficult to produce high structural quality material with this technique. In sputter deposition, boron and nitrogen were ejected from a target that is a source onto a substrate. Large single-crystal hBN monolayers with a lateral size up to 100 µm on Ni substrate was produced.[91-93] Future research should focus on multiply-layers hBN films growth by sputter deposition.

Bulk hBN single crystal growth

The hBN crystal growth process studied in this dissertation was the metal flux method. A flux (a molten metal) is used as the solvent to dissolve the hBN components. There are two significant advantages for the metal flux method: (1) it can grow bulk crystals (hundreds of micrometers thick), compared to chemical vapor deposition, which is better for producing thin layers, generally less than 50 µm thick. (2) The crystal is grown

below the compound's melting temperature. For example, hBN has a melting temperature of 3000 °C, making it hard to grow crystal from the melt. hBN crystals can be grown from a Cr-Ni flux at 1500 °C. Due to the lower temperature, the thermal stress is decreased, making it possible to grow crystals with fewer defects. It also decreases the incorporation of impurities coming from the crucible or the ambient into the crystals, so lowering the growth temperatures remarkably improves the quality of the crystals. (3) Typically, the segregation coefficient k (the ratio of an impurity concentration in the solid phase to the liquid phase) is less than one, so impurities enter the metal solution and not the crystal. Thus crystallization is a purification process. (4) The crystal can be grown under low pressure, providing a way to grow the crystal whose decomposition vapor pressure is high. A proposed flow chart to select the semiconductor single crystal growth method is shown in Figure 2.16.

Crystal growth of the desired material from the melt or a metal flux?

Does the material experiences incongruent melting or a high $T_{melting}$?

No

Yes

Example: silicon is grown
from molten silicon
($T_{melting}$ =1,414°C)

Example: hBN is grown
from metal flux
($T_{melting}$ =3,000°C)

Pulling crystal
from the melt

Identify a suitable metal
solution, stable crucible,
etc.
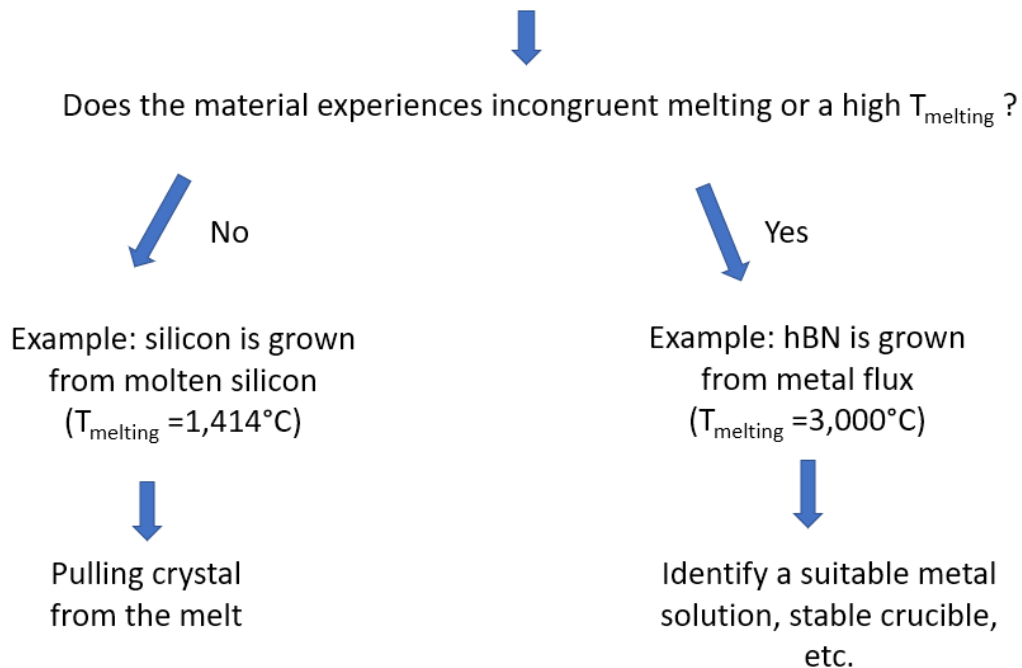
Figure 2.16 Flow chart to determine the bulk-crystal growth method.

22

In the metal flux crystal growth, the source components are dissolved into a molten metal flux at a temperature sufficiently high to form a solution. Then the solution is cooled, causing the component's solubility to decrease and creating a supersaturated metal solution. Crystal growth involves two separate processes: nucleation and growth. The nucleation is mainly a function of temperature, which controls the solubility and supersaturation. There is a critical size for the nucleus to grow, instead of dissolving into the metal melt again. The growth process begins after the nuclei have exceeded a critical size which is a function of supersaturation. For high supersaturation, the growth process begins from smaller nuclei. Conversely, for low supersaturation, the growth needs to reach a larger critical size. To grow larger crystals, the nuclei density must be decreased to obtain a few large crystals, rather than many small crystals. Ideally, the crystal growth rate in specific crystallographic direction should be controlled, to produce crystal with specific morphologies. The ambient pressure should be high enough to suppress significant metal evaporation.

The important properties for metal flux include: a high solubility of boron and nitrogen under the growth temperature and pressure, no metal incorporation into the hBN crystal.[94] For example, B is highly soluble in Ni and N has good solubility in Cr. Therefore, Ni-Cr is a good metal flux to grow hBN. Alumina is a good crucible material, as it is stable against Ni-Cr solutions.

A typical process using a Ni-Cr metal flux is shown in Figure 2.17. In this process, nickel and chromium powders were placed in a hot-pressed BN crucible then loaded into a furnace under N_2 flowing at 850 Torr. The furnace was heated and held at a high temperature such as 1500 °C for several hours, to melt and mix the Ni-Cr flux with BN dissolved from the crucible. N_2 gas works as both a protective and reactive gas. Then the

crucible was slowly cooled at a rate of 1°C/h. During the cooling process, the solubility decreases with the temperature, causing hBN crystal precipitation. Finally, furnace is quenched to room temperature.
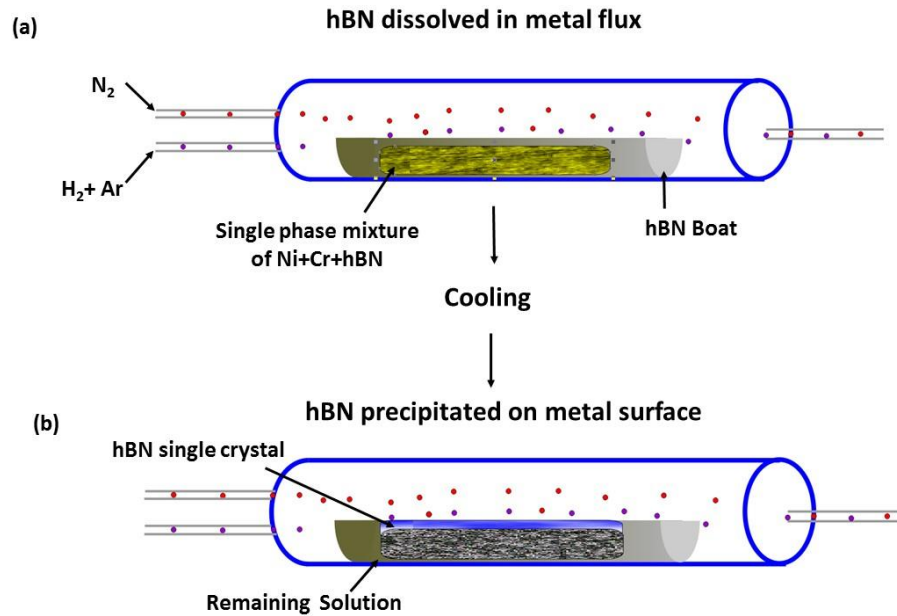
Figure 2.17 A schematic diagram of the hBN crystal growth process. (a) hBN is dissolved in a metal flux at high temperature. (b) hBN single crystals precipitated on the metal flux surface during the cooling process.

Several metal fluxes have been tested for hBN crystal growth and reported in the literature, including Ni-Cr,[95] Fe-Cr,[96] Ni-Mo,[19] Mg,[97] and Ba.

Table 2.2 Summary of hBN bulk single crystal grown from metal flux.

Solvent	Peak position of Raman (cm^{-1})	FWHM of Raman (cm^{-1})	Growth Temperature (°C)	Growth Pressure (atm)	Crystal Size (µm)
Ni-Mo[19]	1365	9.3	1500-1350	1	500
Ni-Cr	1366	8	1550-1450	1	1000
Fe-Cr[96]	1366	7.8	1550-1500	1	1000
Mg	1367	8	1900 - 2100	24317	1000
Ba[98]	Not reported	Not reported	1650-1500	44412	500
Na	Not reported	Not reported	700	25	1

Table 2.2 shows the reported bulk hBN crystals grown from several metal fluxes. From these data, bulk hBN grown from different metal fluxes has similar Raman peak FWHM (8-9.3 cm^{-1}), indicating these hBN single crystals were highly crystalline. To compare the crystal quality, further characterizations such as the electronic property and thermal conductivity are needed. The hBN-based device performance is also helpful to demonstrate a slightly difference of hBN quality. The maximum crystal size is also similar. But the crystal size grown from Na is the smallest. We could presume that the supersaturation of nitrogen in Na is small. Some solvents (Na, Ba and Mg) need a high pressure, this increases the experimental cost. To grow high quality of hBN with a large size in an economic way, a new flux or an improved method is needed.

Chapter 3 - High-quality, three-square-centimeter hexagonal boron nitride crystals growth from Fe flux

Introduction

Two-dimensional (2D) materials have received immense interest for their properties and their proposed applications in optics, electronics, nanophotonics, optoelectronics, and photovoltaics. Of these, hexagonal boron nitride (hBN) has attracted much attention due to its exciting applications as an excellent substrate for graphene devices[99], an excellent protective encapsulant for other 2D materials,[100, 101] a heat management layer in flexible nanoelectronic devices,[32, 102] a single photon emitter, and a platform for nanophotonic hyperbolic devices.[103] In addition, due to its chemical and thermal stability, atomic flatness, large energy band gap (5.9 eV) and absence of dangling bonds and surface charge traps, hBN is an ideal ultrathin insulator and gate dielectric.[104] In these applications, crystal defects can drastically degrade the performance of devices. Therefore, largescale hBN single crystals with low residual impurity concentrations are highly desirable. Considering its high melting temperature (3400K),[105] it is impractical to grow hBN single crystals from a pure melt of hBN. So far, research on hBN synthesis has focused on chemical vapor deposition (CVD)[31, 106-108], molecular beam epitaxy[89, 90] and sputter deposition synthesis.[109] Although CVD is scalable and has the potential to produce large area films with a controlled thickness, those hBN films do not have high structural quality due to the presence of vacancies, grain boundaries,[110] and line defects.[111] Typically, the full-width at half-maximum (FWHM) value of the E_{2g} Raman spectrum for hBN films is between 20 and 30 cm^{-1}. The phonon-assistant peaks greater than 5.5 eV are absent in

their photoluminescence spectrum due to their low crystal quality.[112, 113] The break down electric field for a deposited film, 8-15 nm thick, was reported as 24 MV cm^{-1}.[31]

The solution growth method can produce hBN bulk single crystals with much higher quality than deposition methods. The crystals grown from molten metal fluxes have fewer defects, less thermal strain and fewer impurities, because the impurities in the metal flux do not incorporate into the crystals.[114] The hBN crystal flakes form in a liquid without constraint, unlike deposited films which are strained by mismatches with a solid substrate in symmetries, lattice constants, and coefficients of thermal expansion. So far, hBN crystals have been grown with Na,[115] Ba,[98] Ni,[116] Ni-Cr [95] and Fe-Cr[96] metal fluxes. However, these solvents generally produce small crystals, typically less than 1 mm^2. Furthermore, after mechanical exfoliation, the domain size becomes even smaller, 0.01 mm^2. For the metal-solution crystal growth process, if the supersaturation is too high, highly defective crystals are produced due to dendritic growth and some impurities can be trapped in the crystal as inclusions. In contrast, a low supersaturation takes a very long, impractical amount of time to grow crystals. A very low degree of supersaturation will lead to small size crystals.[94]The challenge remains to identify an optimal metal flux that produces hBN single crystals with fewer impurities and defects for good device performance.

Herein, we report on high-quality, bulk hBN single crystal growth from an iron solution at atmospheric pressure. The quality of the hBN crystals was determined by the Raman and photoluminescence spectra. WSe$_2$ was deposited on the surface of a resulting hBN crystal flake to assess the its defect density. A graphene/hBN/graphene device was fabricated to evaluate the tunneling characteristic of the hBN.

Results and discussion
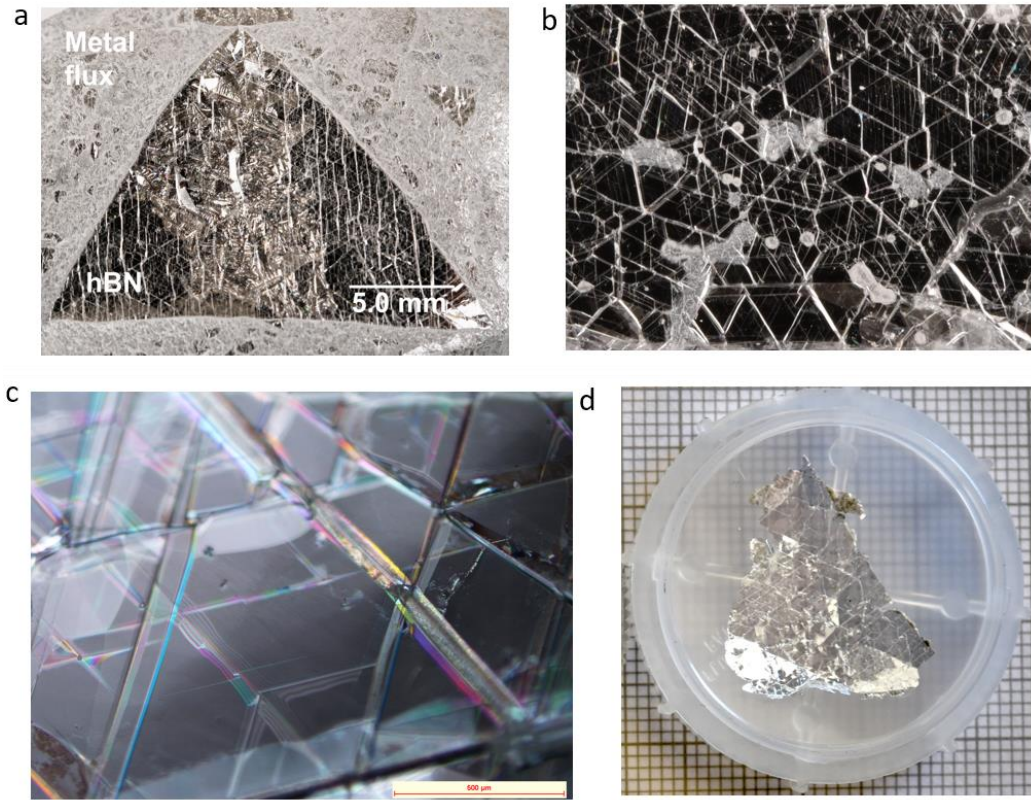
Figure 3.1 Bulk hBN growth from Fe flux. (a) Macro image of hBN on the Fe ingot surface in the alumina boat. (b) Macro image of an enlarged region of the hBN single crystal on the top surface of ingot. (c) An optical micrograph of the hBN single crystal on the top surface of the ingot. The scale bar is 500 micrometers. (d) Macro image of the peeled hBN flake in a wafer carrier. (a) and (d) are from the same crystal.

Crystal growth. The hBN crystals were grown by precipitation from a liquid iron flux. Figure 3.1a shows a macro image of hBN on the Fe ingot surface. A large triangular domain of hBN and several small domains covered the Fe ingot surface. Figure 3.1b displays an enlarged region of the hBN single crystal on the top surface of ingot. The main crystal shapes on the metal surface is triangular. Figure 3.1c shows an optical micrograph of the hBN crystal on the top surface of ingot. The large triangular domain consists of several small triangular domains. Free-standing hBN flakes were peeled from the Fe ingot

28

with thermal release tape. Subsequently, to release the hBN flakes, the tape was heated the tape to 130°C for 5 s. For hBN grown on Ni-Cr or Fe-Cr ingots, this process breaks the hBN crystals, making them smaller. Typically, the flake area of hBN grown on Ni-Cr or Fe-Cr were up to 1 mm^2.   However, the flake area was up to 3-4 cm^2, which is 300 - 400 times larger than our previously reported results.[59, 96] This indicates that hBN grown from Fe has few cracks. Figure 3.1d shows a macrograph of free standing hBN flake peeled from the Fe surface. The resulting hBN flake was highly transparent and colorless.
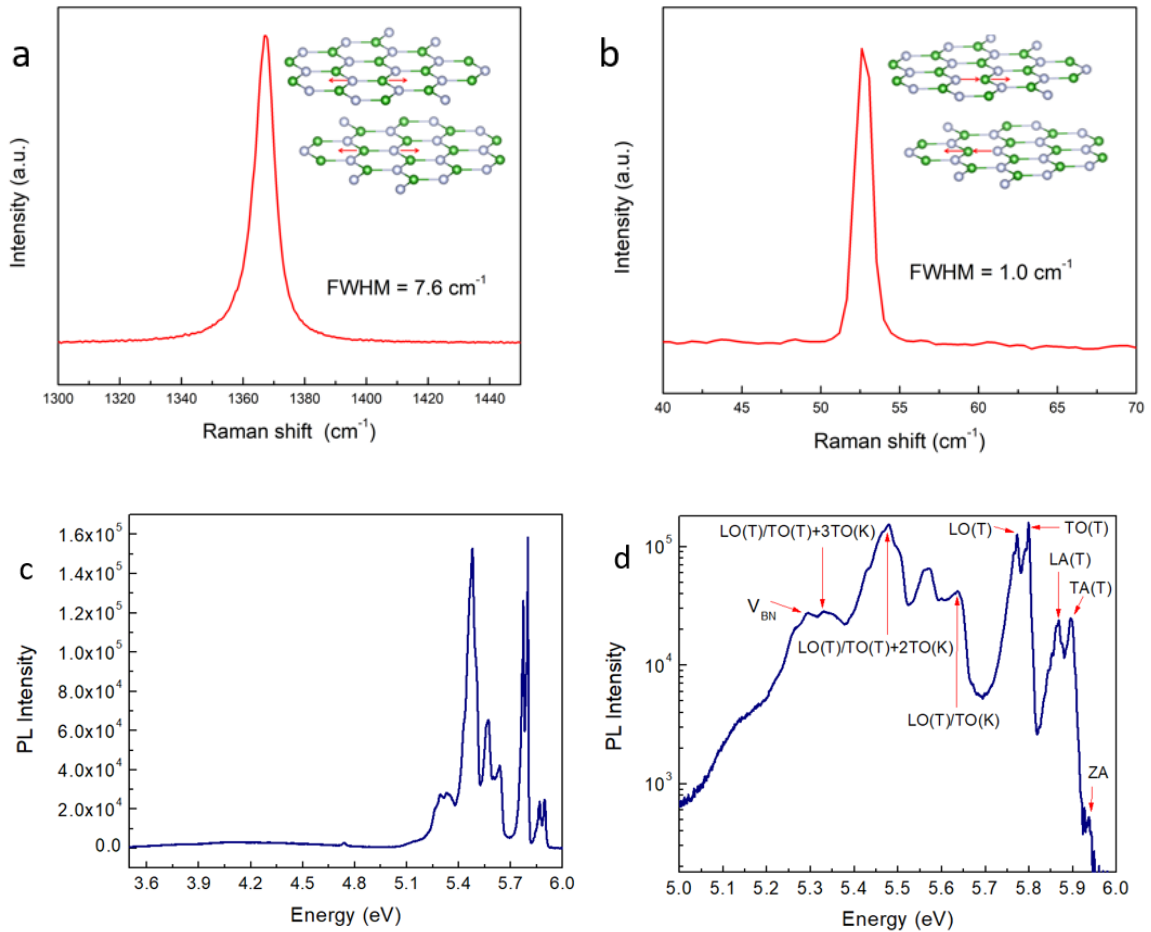
Figure 3.2 Optical characterization of bulk hBN crystal flake. (a) Intralayer mode of Raman spectra of hBN bulk flake. (b) Shear mode of Raman spectra of hBN bulk flake. (c) Photoluminescence (PL) spectra of bulk hBN flake on a linear scale at 8 K. (d) PL spectra of bulk hBN flake on a log scale at 8 K. between 5.0 and 6.0 eV. LO, TO, LA and TA are the longitudinal and transverse optical, and acoustic phonons, respectively[70].

29

Optical characterization of hBN. The Raman spectra of hBN exhibited both the intralayer mode at high frequency and the interlayer shear mode at ultra-low frequency. The intralayer Raman mode corresponds to the E_{2g} vibration between boron and nitrogen atoms in the layer plane at 1367.0 cm^{-1} (Figure 3.2a). The full width at half maximum (FWHM) of E_{2g} peak is 7.6 cm^{-1}, which is comparable to our published result of hBN grown from Ni-Cr or Fe-Cr flux (7.8 cm^{-1}).[61, 95] For typical CVD-grown hBN layers, the peak position appears at 1370.5 cm^{-1} for thin (300 nm) layers [117] to 1369 cm^{-1} for thicker (0.5 µm) films[113], and the peaks widths are between 25 and 30 cm^{-1}.[117] The smaller FWHM indicates that the hBN crystal is higher-quality crystal with few defects. The ultra-low frequency corresponds the rigid shearing vibration mode between adjacent layers (Figure 3.2b),[118] with a peak at 52.7 cm^{-1}, and with a FWHM of 1.0 cm^{-1}. This indicates the crystals have fewer stacking defects.

The photoluminescence (PL) spectra were characteristic of high quality hBN. It did not have the sharp peaks that frequently appear around 4 eV that are associated with point defects.[72] The region above 5.7 eV corresponds to the intrinsic phonon-assisted emission with five phonon replicas: LO, TO, LA, TA and ZO/ZA at 5.76, 5.79, 5.86, 5.89, and 5.93 eV, respectively. Because of the interaction between the intrinsic phonon-assisted recombination and the extrinsic defect mediated emission processes, the presence of phonon-assisted peaks is a signature of high-quality crystal.[89] Bourrellier *et al.*[119] used cathodoluminescence to identify peaks in the energy region between 5.3 and 5.7 eV as related to hBN defects by cathodoluminescence. In PL spectra, the spot size of probe is in the order of 100 µm, so PL detects hBN's grain boundaries as well as stacking defects. Therefore, the emission peak in PL spectra from stacking faults is always at a higher energy

than the one of the intrinsic lines above 5.7 eV. In contrast to these bulk crystals, many CVD-grown hBN layers do not have these intrinsic FX transitions peaks due to defects and impurities.[112, 113] Only for the highest quality bulk crystals, are these peaks present,[69, 70, 89, 120] indicating that the hBN crystals prepared in this study are high-quality crystals with few defects. Their peak intensities of LO and TO is comparable to the peak intensity of LO/TO+3TO (Figure 3.2d). This demonstrates that the sample quality at least matches the best results reported previously.[69]
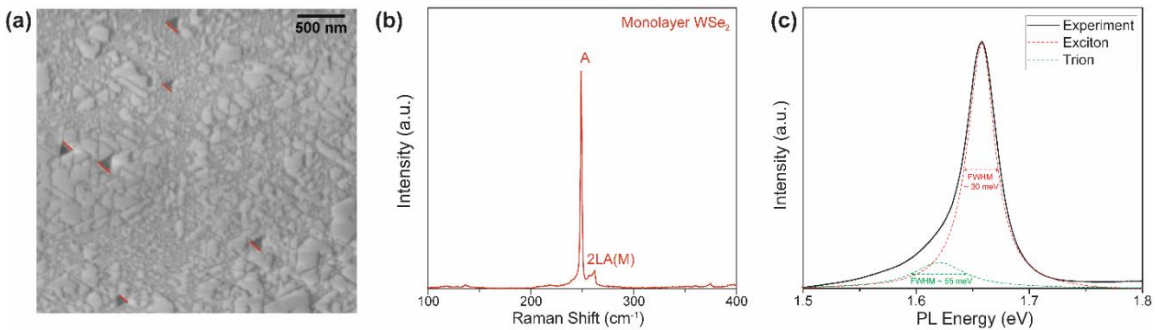
Figure 3.3 (a) Field emission scanning electron microscopy images of WSe$_2$/hBN showing aligned WSe$_2$ domains with one edge marked in red. (b) Raman characteristic peaks of WSe$_2$ confirming the existence of monolayer WSe$_2$ on hBN. (c) The deconvoluted PL spectra of WSe$_2$/hBN at room temperature. The deconvoluted spectra were acquired by performing multipeak Lorentzian fitting using exciton and trion peak positions.

Growth of WSe$_2$ on hBN. Single crystal hBN is a good substrate for the epitaxial growth and encapsulation of 2D transition metal dichalcogenides due to its high dielectric constant and chemically inert surface.[121, 122] When hBN is used as a substrate to deposit WSe$_2$, the nucleation density of WSe$_2$ can be estimated by counting the number of triangular domains in different regions and averaging the density.[123, 124] Previous studies indicate that the nucleation density of monolayer WSe$_2$ on hBN is directly related to the

31

surface defect density of the hBN.[123, 124] To demonstrate the potential to grow 2D semiconducting materials as a substrate and investigate the defects density of our hBN, we carried out the growth of monolayer WSe_2 domains on our hBN flakes by a gas source chemical vapor deposition. The field emission scanning electron microscopy (FESEM) image of hBN surface after the growth in Figure 3.3a shows a group of well-aligned triangular WSe_2 domains (one edge marked in red), indicating their epitaxial growth and the high crystallinity of the hBN flakes. The additional patterns in the FESEM image come from the charging effect due to the insulating nature of hBN. Although the nucleation density of WSe_2 varied across the surface of the hBN, it has a discernibly lower nucleation density, an average of $0.56\pm0.24\ \mu m^{-2}$, than other monolayer WSe_2 growth using exfoliated bulk hBN flakes as subsrates.[68, 123-125] Although additional surface defects can be created during the transfer process, the significant reduction of WSe_2 nucleation density implies the low intrinsic point defect density from the hBN flakes. The Raman spectrum from the WSe_2 (Figure 3.3b) further confirms the triangular domains are monolayer WSe_2 with a characteristic peak at 250 cm^{-1} and no breathing mode at ~310 cm^{-1}. The optical properties of WSe_2 are also strongly affected by their growth conditions, especially the growth substrates.[31] Due to the high crystal quality of our hBN substrate, the PL peak of the monolayer WSe_2 was sharp as shown in Figure 3.3c. The asymmetric peak can be deconvoluted into an exciton peak at 1.66 eV and a trion peak at 1.62 eV. Both the exciton and trion peaks have narrow FWHM, considering the measurement was carried out at room temperature.
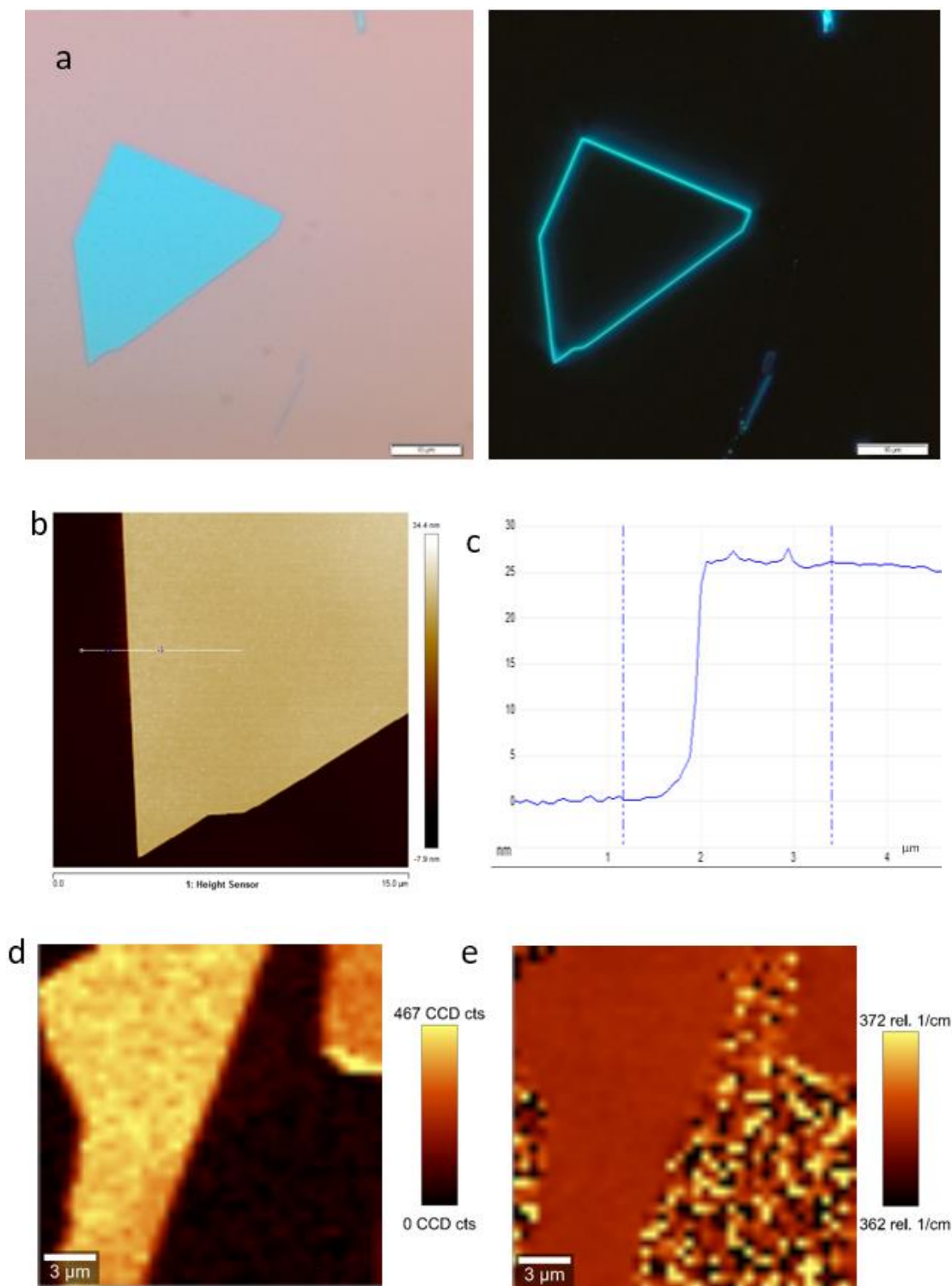
Figure 3.4 Characterization of a hBN sheet. (a) Bright and dark field optical images of an exfoliated hBN film with the thickness of 25 nm. The scale bar is 10 µm. (b)AFM image of the hBN film. (c) The height profile of the hBN film. (d) Raman maps of intensity of the hBN film. (e) Raman map of peak position of the hBN film.

33

hBN nanosheet. For many device applications, the surface flatness and uniformity of the hBN is very important. To test the thickness from our crystals, an exfoliated hBN nanolayer was characterized by atomic force microscopy (AFM). In Figure 3.4a, bright and dark field optical images, no cracks are visible. The AFM image in Figure 3.4b shows the film has a flat and uniform surface. The thickness is 25 nm (Figure 3.4c). Raman mapping reveals a highly uniform intensity (Figure 3.4d) and peak position (Figure 3.4e), indicating a highly uniform flatness and thickness and a highly crystalline surface, respectively. These results imply that our hBN is a great candidate as a substrate in various nanodevices.
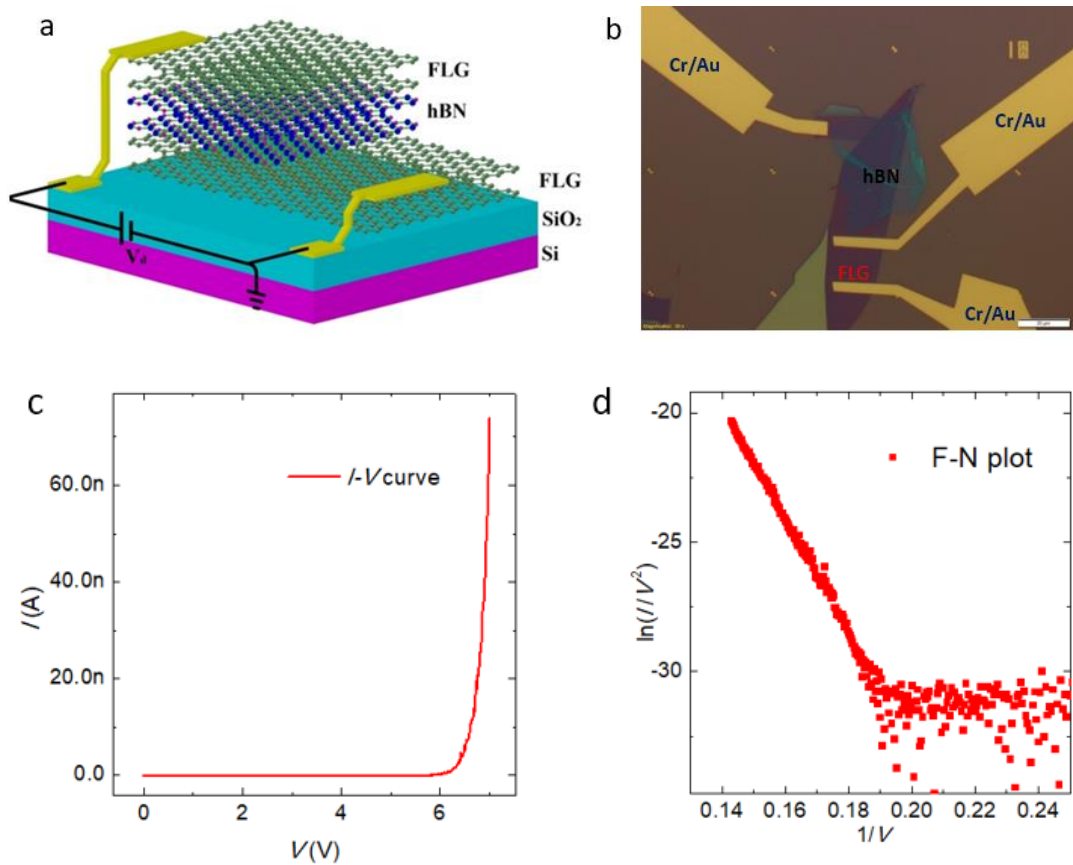
Figure 3.5 Vertical hBN tunneling devices based on van der Waals heterostacks consisting of few-layer graphene (FLG)–hBN– FLG. (a) Schematic view of a typical tunneling device. (b) Bright-field optical image of the device. (c) I_d−V_d characteristic at V_g = 0 V. (d) Fowler-Norheim (F-N) plot of the I_d−V_d at a high bias voltage.

Dielectric properties. To evaluate the dielectric properties of our hBN, a metal-insulator-metal vertical device was built based on a van der Waals heterostack. The device consists of a hBN on top of a few-layer graphene (FLG) layer, capped with another FLG (see the experimental methods section for details). Figure 3.5a is a schematic of our device. To measure the breakdown electric field of the hBN, a voltage bias was applied to the two (top and bottom) FLG. The thickness of hBN is 4 nm, as measured by AFM. Figure 3.5c shows a representative current versus applied electric voltage plot. In the tunneling regime of a thick insulator (here 4 nm) and high bias condition (here > 6V), suppose α, $\hbar$, ϕ_B, e, m, m*and d are the effective contact area, Planck's constant, barrier height, electron charge, free electron mass effective electron mass and barrier width, respectively the *I-V* characteristic follows the Fowler-Norheim tunneling equation,

$$I_d(V_d) = \frac{\alpha e^3}{8\pi\hbar\phi_B} \frac{m}{m^*} \left(\frac{V_d}{d}\right)^2 \exp\left(-\frac{8\pi\sqrt{2}\phi_B^{3/2}}{3\hbar e} \frac{d}{V_d}\right)$$

Fowler-Norheim tunneling mechanism indicates an ideal insulator behavior.[126, 127] Figure 3.5d shows that the plot of ln (I_d/V_d^2) versus $1/V_d$. A strong linear dependence in the F-N plot indicates that the tunneling is dominated by the F-N mechanism.

The device shows tunneling characteristic with a turn-on voltage of 5.5 V by the voltage at which the current reaches 10^{-11}A (Figure 3.5c). This value is comparable to the b hBN crystalline film with thickness of 8-15 nm previously reported by Kim *et al.*[31], exfoliated hBN reported by Lee *et al.* [100] and that of SiO_2 [128], suggesting our hBN has good insulating characteristics. This high turn-on voltage and ideal field emission tunneling suggests that the hBN is an excellent material as a 2D dielectric and tunneling layer.

Conclusion

In summary, large-area and high-quality hBN single crystal flakes were grown via a new metal flux, pure iron. Iron was selected to grow hBN as metal flux due to the optimal nitrogen solubility. The hBN crystals were up to 3 cm^2 in area, which is 300 times larger than what has been previously reported. The narrow E_{2g} vibration peak (7.6 cm^{-1}) in Raman spectra and the presence of phonon-assist peaks in photoluminescence spectra indicate the hBN produced with this flux are high crystal quality. WSe$_2$ deposited on its surface with a low nucleation density, further demonstrating that the hBN has a low defect density. A graphene/hBN/graphene tunneling device shows tunneling characteristic with a turn-on voltage Vth > 5.5 V. In the tunneling regime, the I-V characteristic follows the Fowler-Norheim tunneling behavior, as shown in the linear character of the F-N plot. This high turn on voltage and ideal field emission tunneling suggests that the hBN works perfect as a 2D dielectric and tunneling layer. The crystals are ideal materials for high performance devices and investigation of thermal, optical and electrical properties of hBN. This study not only paves a way for the production of high-quality, large-area hBN but also provides a new strategy to advance growth research.

Experimental methods

hBN single crystal growth. Fe powder and a hot-pressed boron nitride crucible were loaded into an alumina crucible in an alumina tube furnace. The crucible was heated at 1550 ℃, then hBN crystals were precipitated on the surface of the Fe flux during the cooling process. Before the experiment, the alumina tube was purged three times by nitrogen and forming gas (5% hydrogen in balance argon). The hydrogen in the forming

gas reacts with any remaining oxygen in the tube to minimize oxygen contaminants in hBN crystals. During the experiment, nitrogen and forming gas flowed through the tube continuously at a pressure of 820 Torr. The flow rates were 140 and 20 sccm, respectively. Fig. 1(b) shows the temperature profile during the crystal growth. The Fe powder was heated to, and held at 1550℃ for 24h, enabling the boron and nitrogen to dissolve in the Fe metal flux to form a liquid solution. After dwelling at this temperature for 24 hours, the crucible was cooled down from 1550℃ to 1450℃ at a rate of 4℃/h. Finally, the system was quickly quenched to room temperature.

Raman spectra. Raman spectra were taken at room temperature using a Horiba Labram HR Raman microscope system. A 532 nm laser was used. The laser spot was focused by a 100x lens to a spot diameter of ~1 μm. By using an 1800 groove/mm grating, we achieved an instrument resolution of ~0.5 cm^{-1}. Lorentz equation was used to normalize the result.

Photoluminescence spectra. The optical properties of our samples were characterized by PL spectroscopy. The hBN crystals were held on the cold finger of a closed-cycle cryostat at a temperature of 10K. The excitation beam is the fourth harmonic of a cw mode-locked Ti-Sa oscillator (194 nm) with a repetition frequency of 82 MHz. The beam was focused on the sample with a spot diameter of ~50μm and a power of ~35 μW. An achromatic optical system couples the emitted signal to our detection system using parabolic mirrors with a special coating for deep UV. The detection system was composed of a f = 300 mm Czerny-Turner monochromator, equipped with a 1800 grooves/mm grating blazed at 250 nm, and a back-illuminated CCD camera (Andor Newton 920), with a quantum efficiency of 50% at 210 nm, operated over integration times of 1 min.

37

Monolayer WSe$_2$ growth and characterization. Monolayer WSe$_2$ domain were synthesized through a multi-step gas source CVD process using tungsten hexacarbonyl (W(CO)$_6$, Sigma-Aldrich, 99.99% purity and hydrogen selenide (H$_2$Se, Matheson, 99.998% purity) in a cold-wall vertical reactor with an inductively heated SiC-coated graphite susceptor.[56] Ultra-high purity hydrogen was used as the carrier gas through the bubblers and reactor to maintain a total flow rate at 450 sccm and a reactor pressure at 700 Torr. Single crystals of hBN flakes were exfoliated onto a c-plane (001) double-side polished sapphire as a handle substrates. The W(CO)$_6$ powder was contained inside a stainless steel bubbler held at 30℃ and 730 Torr. A short duration of nucleation and lateral growth time was adapted in the growth of WSe$_2$ in order to separate and clearly distinguish each WSe$_2$ domains. When the substrate reached 800℃, hydrogen carrier gas started passing through the bubbler at a flow rate of 20 sccm which resulted in a W(CO)$_6$ flow rate of 1.8×10^{-3} sccm out of the bubbler for 1 minutes. Subsequently, hydrogen carrier gas was switched to a lower flow rate of 2 sccm through the bubbler which resulted in a W(CO)$_6$ flow rate of 1.9×10^{-4} sccm out of the bubbler for 20 min. The H$_2$Se flow rate and substrate temperature were held constantly at 7 sccm and 800℃ respectively during the entire growth.

The surface morphology of the WSe$_2$ on hBN was measured by field emission scanning electron microscopy (FESEM) using a Zeiss Merlin instrument. The Raman and PL spectra of WSe$_2$ were acquired in a HORIBA LabRAM HR Evolution high spectral resolution analytical Raman microscope at room temperature with a laser wavelength of 532 nm and a 1800 lines/mm grating.

Tunneling devices. The devices were prepared on a SiO_2/Si substrate using PDMS dry transfer technique[129]. FLG (<2 nm) and hBN (~ 4 nm) were exfoliated from a bulk crystal onto PDMS surface and then transferred on SiO2/Si substrate. The sample thicknesses were measured by AFM. The heterostacks were annealed in vacuum for 2h in 200 ˚C. Standard electron beam lithography was used to pattern electrodes onto the top and bottom FLG layers. Cr/Au (2 nm/50 nm) electrodes were deposited by thermal evaporation. Diode bias was applied on FLG induces tunneling of carriers across the hBN layer. Electrical measurements of the device were conducted using a parameter analyzer (B1500A) in a nitrogen glove box atmosphere.

Acknowledgement

Chapter 4 - Hexagonal boron nitride single crystal growth from solution with a temperature gradient

Introduction

Hexagonal boron nitride (hBN) has emerged as a useful material in a broad range of applications, including heat management of flexible nanoelectronics,[102, 130] substrates for other 2D materials,[131] hole-transport and electron-blocking layer on van der Waals heterostack LED,[132] infrared nanophotonics,[133, 134] single photon emitter,[135] flexible neutron detectors,[86, 136] deep UV emitters,[89] and membranes for hydrogen isotope separations.[137] To achieve the highest device performance possible, high-quality, large-area single crystal hBN is required for these applications. Structural defects such as grain boundaries, points defects and dislocations can alter hBN's electronic and optical properties, thus degrading the performance of hBN-containing devices.[110]

We have previously demonstrated high quality hBN crystal growth by the metal flux solution method with slow cooling. In this method, boron and nitrogen are dissolved at high temperature in a molten metal flux, then hBN crystals precipitated as the solution is cooled. This crystal growth is performed at atmospheric pressure. High-quality bulk hBN crystals were produced by both nickel/chromium[95] and iron/chromium fluxes.[61] The hBN grown from both solvents were high quality, as indicated by the narrow E_{2g} peak (a full width at half maximum (FWHM) of 8 cm^{-1})[95] in the Raman spectra and the presence of high energy peaks around 5.75 eV in the photoluminescence (PL) spectra.[138] In contrast, typically, the FWHM of the E_{2g} peak in the Raman spectra taken from chemical vapor

deposition grown hBN is about 20-30 cm^{-1} ,[62] and the high energy emission peaks in PL or cathodoluminescence spectra are absent.[112, 113]

However, the slow cooling solution growth method has its limitations. Most significantly, the crystals precipitate over a wide range of temperatures, from the maximum temperature (1550 °C in our prior studies) until the flux completely solidifies (1350 °C or less). This is a problem because the crystal quality and size tends to decrease as the temperature decreases.[94] To overcome these problems, in this work, we induced the large area bulk hBN single crystal growth by applying a temperature gradient across the molten metal flux. The source material dissolves in the high temperature region, and hBN crystals precipitate at the lower temperature, so both heat and mass transfer work together, to provide a suitable supersaturation for crystal growth. The crystal quality was characterized by Raman spectroscopy, photoluminescence spectroscopy and X-ray diffraction. The in-plane and out-of-plane thermal conductivities were measured by the nanosecond transient thermoreflectance technology. Nanometer thick hBN layers were exfoliated from the bulk hBN flake and characterized by atomic force microscope and Raman mapping method.

Results and discussion
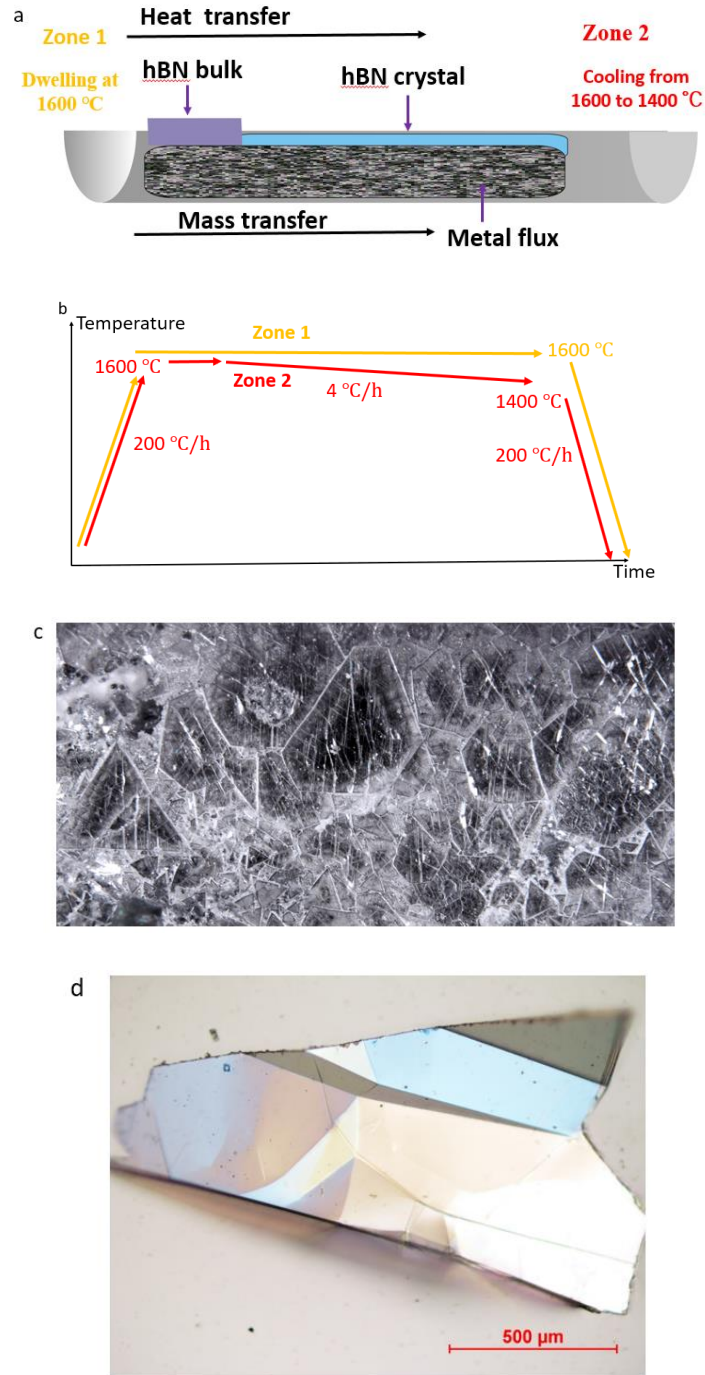
Figure 4.1 hBN bulk single crystal growth from metal flux using temperature gradient. (a) Schematic diagram of the temperature gradient approach used for hBN crystal growth. (b) Temperature profile for crystal growth. Heat zone 1 was kept at 1600 ℃ during crystal growth process (yellow line), heat zone 2 was cooled from 1600 ℃ to 1400 ℃ at a cooling rate of 4 ℃/h (red line). (c) Macro image of the entire Fe-Cr ingot covered with hBN single crystals. (d) Micro images of hBN flake peeled from the ingot. Scale bar is 500 µm.

Crystal growth using temperature gradient technology. hBN single crystals were grown from a Cr-Fe flux using temperature gradient technology (see the experimental section for details). A two heating zones furnace system produced the temperature gradient, as shown in Figure 4.1a. Figure 4.1b illustrates the temperature profile for the two heating zones. During the hBN crystal precipitation process, the HPBN source dissolved continually in the high temperature region (left side) and hBN crystals precipitated in the cooler region (right side). There exists a concentration gradient in the boat, both heat and mass transfer can work as driving force to provide supersaturation for the crystal growth. After Fe-Cr solidification, hBN crystals covered the surface of Fe-Cr ingot. Figure 4.1c displays the macro images of hBN on the Cr-Fe ingot. In the area which was far away from boron nitride source, there were many hexagonal domains with sizes up to 4-5 mm. In the area closed to boron nitride source, because both BN concentration and temperature is higher than the far boron nitride source area, the higher supersaturation and nucleation rate produced small crystals.[94] Large-area hBN flakes were peeled from the ingot (Figure 4.1d).
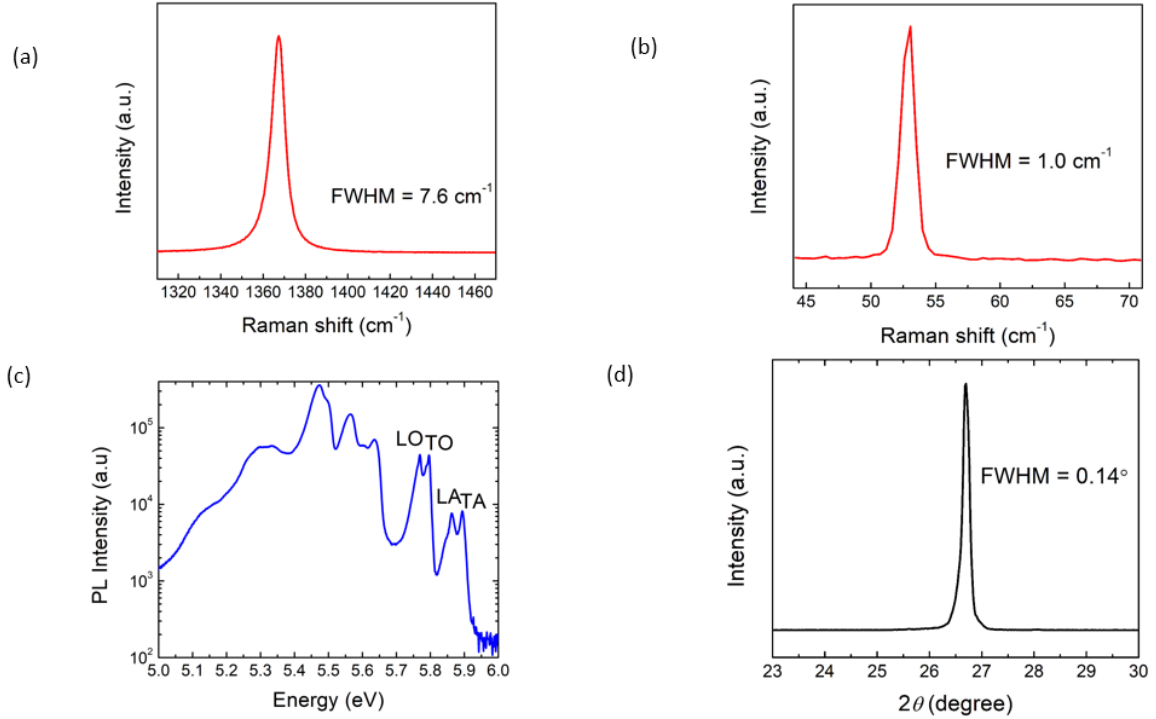
Figure 4.2 Characterization of hBN. (a) Raman spectra of the in-plane modes. (b) Raman spectra of shear mode. (c) Photoluminescence spectra of bulk hBN on a log scale at 8K ranging from 5 to 6 eV. (d) X-ray diffraction pattern.

Characterization of hBN. Raman spectra, photoluminescence, XRD and XPS were used to characterize the hBN flake. Figure 4.2a shows the in-plane mode of the Raman spectra of hBN. The E_{2g} peak appears at 1367.1 cm^{-1}, which originates from the in-plane vibration between boron and nitrogen. The full width at half maximum (FWHM) was 7.6 cm^{-1}, which is similar to previous high-quality bulk hBN grown by slowing cooling Fe-Cr flux (7.8 cm^{-1}), indicating that our hBN is highly crystalline in-plane. The low-frequency peak was at 52.8 cm^{-1} with a FWHM of 1.0 cm^{-1} corresponding to the rigid shearing motion between adjacent layers, as shown in Figure 4.2b, which is also comparable to reported previously bulk hBN grown,[59] indicating our hBN is highly crystalline in the *c*-direction.

Figure 4.2c displays the PL spectrum of the hBN flake on a log scale at 8 K. As an indirect bandgap semiconductor, during photon emission or absorption process, phonon

44

scattering is necessary   to conserve both energy and momentum.[69] Therefore, the presence of phonon-assisted emission peaks between 5.7 and 6.0 eV in the spectra are indicative of high quality hBN single crystals.[70, 139] As show in Figure 4.2c, four phonon replicas (LO, TO, LA and TA) between 5.7 and 6.0 eV can be seen clearly. Their presence indicates that the crystal are highly crystalline, with a low defect density, which is comparable to bulk hBN grown by slowing cooling solution method. Moreover, the broad emission band below 5.7 eV (at 5.62, 5.56, 5.47 and 5.3 eV) have been identified as stacking defects-related emission in bulk hBN.[120] The peaks come from phonon-assist inter-K valley scattering, which becomes observable because stacking defects in bulk hBN provide a density of final electronic states.[69]

Figure 4.2 d shows the XRD pattern of the hBN. The peak centered at two theta equal to 26.7° corresponds (002) crystal plane.[117] The FWHM is 0.14°, which is significantly better than CVD films (0.6°)[62] or bulk hBN produced by slow cooling (0.6-0.3°)[95]. Both the small XRD peak and the presence of the shear mode in the Raman spectra indicate that highly crystalline hBN in the c-direction. X-ray photoelectron spectroscopy shows that the binding energies for B 1s and N 1s are at 190.3 eV and 397.8 eV, respectively, which are comparable with previously reported values.[140]
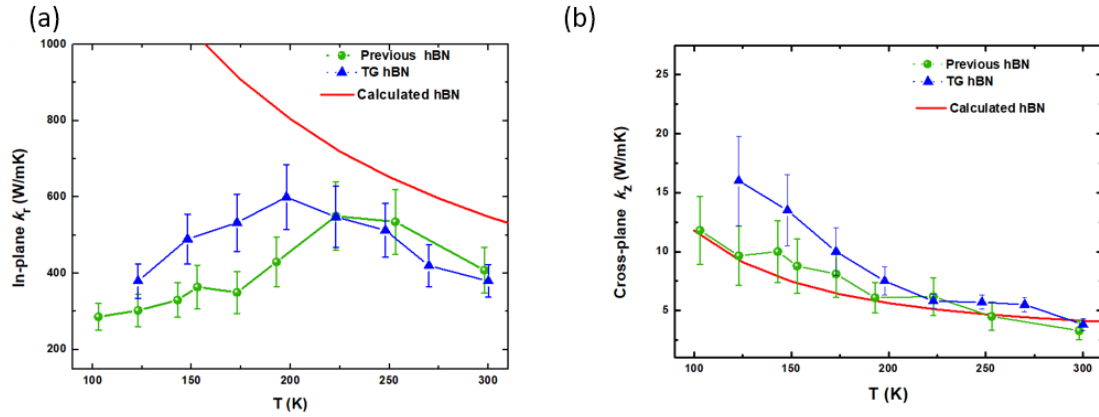
Figure 4.3 Temperature-dependent thermal conductivity of a hBN flake grown by the temperature gradient method. (a) in-plane (k_r) and (b) out-of-plane (k_z) of hBN flake (blue triangular), along with measurements on a hBN flake grown by slow cooling (green circle) and theoretical results (red line) from the Boltzmann transport equation /density functional theory calculations.[32]

Temperature-dependent thermal conductivity of hBN flake. In hBN, heat is mainly conducted by phonons, so thermal resistance is produced by intrinsic isotopic disorder, phonon-phonon, and extrinsic crystal defects scattering.[141] The in-pane (k_r) and out-of-plane (k_z) thermal conductivities of the hBN were measured by nanosecond transient thermoreflectance technology.[32] Figure 4.3 compares the temperature dependent thermal conductivity of k_r and k_z for a hBN flake produced by the temperature gradient method from the current study, with a hBN flake produced by slow cooling and theoretical calculation results[32]. These hBN crystals have the exact same intrinsic isotopic and phonon-phonon scattering, so the higher k_r of the hBN flake produced by the temperature gradient in the temperature ranging from 125 K to 200 K (as shown in Figure 4.3a) originates from a lower extrinsic defect density than the hBN grown by slow cooling. At room temperature, k_r was 420 ± 65 W m^{-1} K^{-1}, among the highest previously reported values for natural hBN.[32, 142, 143]

We also performed a defect-controlled epitaxial growth of WSe_2 on our hBN, the nucleation density is determined by hBN point defects. A low nucleation density of WSe_2 on hBN also confirms that the hBN has low defect density.[123]

As shown in Figure 4.3b, the k_z of our hBN was significantly higher than the slow cooled grown hBN at low temperature ranging between 100K and 200K. The high k_z results at low temperature, along with Raman and XRD results (the small FWHM of shear mode Raman vibration and 2θ peak at XRD) confirms that our hBN has higher crystallinity than the hBN grown by slow cooling. At room temperature, the k_z was 4.3 ± 0.6 W m^{-1} K^{-1}, which is also in good agreement with the literature values.[32]
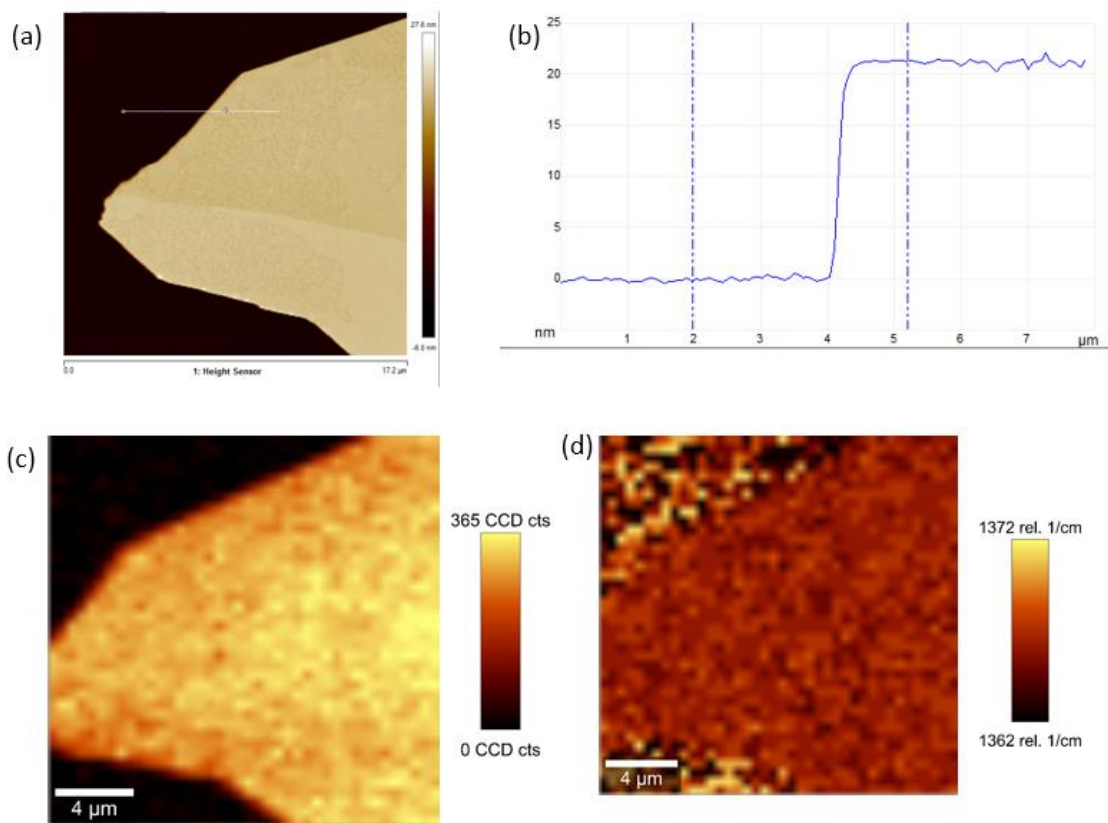
Figure 4.4 Characterization of an exfoliated hBN sheet. (a) AFM image of an exfoliated hBN sheet on a substrate. (b) The height profile of the exfoliated hBN sheet along the line in (a). (c) Raman intensity map of the E_{2g} peak. (d) Raman position map of the E_{2g} peak.

47

For device fabrication, thin, nanometer thick hBN layers are needed, and these must be exfoliated from the bulk hBN flake. To demonstrate the potential of our hBN for nano device applications, hBN layers were produced by exfoliating hBN flake mechanically. Figure 4.4a shows AFM image of an exfoliated hBN film. Figure 4.4b displays that the thickness is 20 nm. Figure 4.4c and d show Raman mapping image of the E_{2g} peak. As shown in c, the Raman intensity was uniform over the entire film at different locations, suggesting that the hBN film is continuous with a uniform thickness. The Raman peak position was consistent everywhere, indicating that the hBN film is highly crystalline on all surface. High-quality of hBN film implies that our hBN is good candidate for device applications such as a substrate, tunnel barrier or encapsulating layer.

Conclusion

Large-area and few-defect hBN single crystals were grown using metal flux method with a temperature gradient, which allows both heat and mass transfer to produce driving force for crystal growth. Using this method, the maximum crystal domain size was up to 4 mm. The narrow E_{2g} peak of Raman (a FWHM of 7.6 cm^{-1}) and the presence of the intrinsic phonon-assisted emission peaks in the photoluminescence spectra indicate that our hBN is highly crystalline. The shear mode of the Raman spectra and the XRD results demonstrate that our hBN has few stacking defects. In addition, high in-plane and out-of-plane thermal conductivity confirms that our hBN flake has few defects in plane. High out-plane thermal conductivity is another evidence to prove our hBN is highly ordered in *c*-direction. Moreover, highly crystalline hBN film was prepared by mechanical exfoliation. AFM and

Raman map characterization show our hBN has uniform and an atomically smooth surface, which suggest that the hBN flake has potential for nanodevice application. The work not only inspires a new strategy for large single crystal growth but also provides a high-quality hBN flake and film for nano device applications.

Experimental methods

Crystal growth and hBN flake preparation. A horizontal alumina tube furnace system was used to grow hBN crystals. Fe-Cr metal flux was used to dissolve boron and nitrogen.[96] As shown in Figure 4.1c, an alumina boat was filled with 50wt%Fe-50wt%Cr powder mixture. A hot-pressed boron nitride source was put in the left side of the boat. The boron nitride source located in the left side of in the alumina boat filled. Before heating the furnace, the tube was purged three time with nitrogen and forming gas (H_2 5% and Ar 95%). During heating process, nitrogen and forming gas flowed through the furnace system at a flow rate of 5 sclm and 20 sccm, respectively. Two heating zones were applied to produce the temperature gradient. The boat was located at in the center line of two heating zones. Figure 4.1b showed the temperature profile of two heating zones. At beginning of experiment, both zone 1 and 2 were heated at 1,600 °C for 24h to dissolve boron and nitrogen. During crystal growth process, zone 1 was dwelled at 1,600 °C. Then zone 2 was cooled down to 1,400°C at a cooling rate of 4 °C /h, thus temperature gradient was formed between heating zone 1 and 2. Crystal formed during zone 2 cooling process. Finally, the two zones were quenched to room temperature to form Fe-Cr ingot. hBN crystals covered Fe-Cr ingot surface. hBN flakes were peeled from Fe-Cr ingot using thermal release tape. The tape was heated at 130 °C, then washed by acetone, adhered hBN flake was released.

Photoluminescence spectroscopy. The hBN sample were mounted on a cold finger of a closed-cycle cryostat at a temperature of 10K. The excitation beam is the fourth harmonic of a cw mode-locked Ti-Sa oscillator (194 nm) with a repetition frequency of 82 MHz. The beam is focused on the sample with a spot diameter of ~50µm and a power of ~35µW. An achromatic optical system couples the emitted signal to our detection system using parabolic mirrors with a special coating for deep UV. The detection system is composed of a f = 300mm Czerny-Turner monochromator, equipped with a 1800 grooves/mm grating blazed at 250 nm, and a back-illuminated CCD camera (Andor Newton 920), with a quantum efficiency of 50% at 210 nm, operated over integration times of 1 min.

Raman spectra. Raman spectroscopy was performed at room temperature using a Horiba Labram HR Raman microscope system. A 532 nm laser power was used. The laser spot was focused by a 100x lens with a spot diameter of ~1 µm. Using an 1800 groove/mm grating, a resolution of ~0.5 cm^{-1} was achieved.

X-ray diffraction. hBN flakes were stacked and covered the entire Si/SiO$_2$ substrate. A Cu K-alpha source was used.

Thermal conductivity measurement. A transient thermoreflectance technique was applied to measure both the out-of-plane and in-plane thermal conductivity of hBN[32]. Briefly, a 50 nm Au film was deposited on hBN flake surface as transducer, with a 10 nm Ti interlayer for good adhesion. A 10 ns, 355 nm pulsed pump laser heated the Au film to produce a temperature response. A continuous 32 nm laser was used to monitor the temperature response via the change of Au reflectivity. A cryostat was used to control the

measuring temperature from 100 K to 300 K. An analytical photothermal pulses-induced thermal transport model was used to analyze the measured transients.[32]

Acknowledgement

Chapter 5 - Monoisotopic boron- hexagonal boron nitride crystals：growth and optical characterization

Introduction

Hexagonal boron nitride (hBN) has received a lot of attention recently because of its excellent properties such as its chemical inertness, wide energy bandgap (5.9 eV), atomically smooth surface that is free of dangling bonds,[144] and high in-plane thermal conductivity.[32] These properties make hBN appealing for such applications as deep UV emitter and detectors,[49] substrates for other two-dimensional materials,[54] quantum emitters,[145] heat management layers in nano devices,[57] dielectrics,[146] neutron detectors,[147] and so on. For these applications, hBN single crystals are needed.

Beyond natural hBN, monoisotopic boron hBN single crystals possesses more novel properties. Most current research use hBN with the natural distribution of boron isotopes: ^{11}B (80.1%) and ^{10}B (19.9%). Due to the different neutron spin number and atomic mass between ^{10}B and ^{11}B isotopes, pure boron and boron compounds with a single isotope (monoisotopic) possess different phonon effects including electron-photon interaction, isotopic disorders and average isotopic masses.[138] The different properties of ^{10}B and ^{11}B isotopes cause monoisotopic boron to have different applications. For example, ^{10}B-enriched boron nanoparticles can enhance the contrast of magnetic resonance imaging of brain tumor.[148]In addition,^{10}B has a large capture cross-section of thermal neutrons (3840 barn at 0.025meV). In contrast, ^{11}B is nearly transparent to neutrons. Thus, boron

compounds enriched in ^{10}B are better suited for neutron detectors than those with the natural distribution of boron.

In the case of hBN, changing the relative concentrations of the ^{10}B and ^{11}B isotopes affect its properties, including the optical excitation spectra and energy gaps.[63] Monoisotopic boron hBN single crystals are of interest for the investigating the boron isotopic effects. Monoisotopic hBN provides the novel properties and applications including heat management, nanophotonics and thermal neutron detecting. For example, because of its anisotropic thermal conductivity (high in-plane and low out-of-plane), chemical stability and mechanical flexibility at high operating temperature, monoisotopic hBN opened up an opportunity for next generation thermal management materials, such as cooling bendable nanoscale microelectronics or thermoelectrics. Compared to natural hBN, monoisotopic hBN possesses a high thermal conductivity because of reduced isotopic phonons scattering. Moreover, hBN is a low-loss phonon polariton material. First-principles calculations predict the polariton lifetimes of monoisotopic hBN can be a factor of ten times longer than hBN with the natural distribution of boron isotopes because of less phonon scattering, so it is a promising materials for high-efficiency, polaritonic devices.[149] A threefold increase in the bulk phonon lifetimes and approximately equal increase in propagation length of phonon polariton over the already low-loss natural hBN crystals were experimentally demonstrated.[149] Furthermore, neuron detectors fabricated with h^{10}BN epilayers have achieved an efficiency of 51.4%, which is the highest among all semiconductor neutron detectors.[86]

Although monoisotopic boron hBN single crystals are promising in more potential applications, its growth has not been well studied. Our group has previously reported the

single crystal growth of millimeter-sized monoisotopic hexagonal boron nitride by using Ni-Cr flux crystal growth technique. Monoisotopic boron powders, i.e.,^{10}B and ^{11}B, and nitrogen were used as the precursors. Both h^{10}BN and h^{11}BN single crystals were produced from Ni-Cr flux solvent at 850 torr. Their Raman peak width were narrow (~ 3 cm^{-1}) indicating their excellent structural quality. There was a clear spectral shift in both the shear and intralayer Raman modes in monoisotopic hBN, with the specific boron isotope.

In this study, photoluminescence (PL) and Raman spectra were used to evaluate the quality and purity of the monoisotopic hBN. PL can characterize the optical properties and electronic property of a semiconductor, including the energy bandgap in intrinsic materials and additional states that arise in doped or defected materials. In a PL process, a system is excited by a photon to create an electron-hole pair. The free electron and hole undergo relaxation then via radiative recombination, the system returns from an excited state to the

Here we investigated the solvent effect of Fe-Cr and pure Fe on monoisotopic hBN crystal quality. For metal flux techniques, impurities can degrade the hBN quality. Potential sources of impurities in the hBN are the metals comprising the flux (i.e., Fe, Ni, and Cr), as well as impurities in the metal fluxes (carbon and oxygen for example). These can incorporate as precipitates (inclusions), substitutionally on lattices sites, or intercalated between the layers of hBN.[94, 150] Iron is a potential alternative to nickel. It is much less expensive and commercially available in high purity. Our prior study demonstrated that Fe-Cr metal flux can grow hBN with the natural boron distribution from a hot pressed boron nitride source.[96] Some prior studies also suggest pure iron is a potential metal flux to grow hBN: the presence of boron in solid iron can increase nitrogen solubility between 950 and 1150°C.[151]

ground state by emitting a photon. The presence of defects and impurities introduces new energy levels within the forbidden gap. The relaxation favors low energy states, so low concentration of impurity can cause a significant PL signal.[69]

In the present study, we examined whether iron−chromium and pure iron solvent can also produce $h^{10}BN$ and $h^{11}BN$ crystals with comparable quality as the Ni−Cr solvent. The crystal quality was characterized by Raman and photoluminescence spectra. The small FWHM values of shear mode and intralayer mode in Raman spectra demonstrate the crystals are comparable to the $h^{10}BN$ and $h^{11}BN$ grown from Ni-Cr flux. Phonon-assisted transitions in photoluminescence (PL) spectra caused by longitudinal optical (LO) and transverse optical (TO), longitudinal acoustic (LA), and transverse acoustic (TA) phonons confirm that the crystals are the high quality, with low defect densities and impurity concentrations. These $h^{10}BN$ and $h^{11}BN$ crystal can be used for researching the isotopic effects on the electronic and optical properties.

Results and discussion
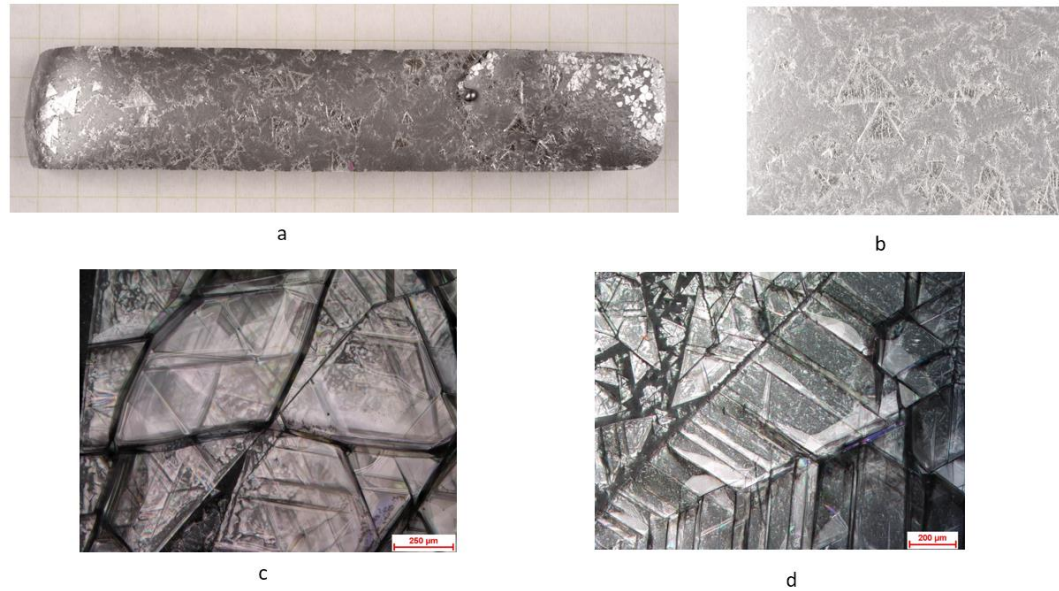
Figure 5.1 Macro and micro images of $h^{10}BN$ single crystal. (a) $h^{10}BN$ single crystal on the top surface of the Fe-Cr ingot. The grid size 5 mm × 5 mm. (b) an enlarged region of the $h^{10}BN$ single crystal grown from Fe-Cr on the top surface of ingot. (c) micro images of $h^{10}BN$ single crystal grown from Fe-Cr. (d) micro images of $h^{10}BN$ single crystal grown from Fe.

After the solution was quenched from 1450 ℃ to room temperature, the metal ingot surface was covered by hBN crystals. Figure 5.1a is a macro image, showing an example of $h^{10}BN$ crystals on the Fe-Cr ingot. Some individual triangular and imperfect polygonal domains formed on the top surface of the Fe-Cr ingot, which is the typical morphology of hBN grown from a metal flux.[59, 95, 96] There were some opaque areas on the surface of ingot (Figure 5.1b), which comes from small size $h^{10}BN$ crystal due to the high supersaturation during nucleation process. Actually, the entire surface was not fully covered by h10BN crystal: bare metal was exposed in some regions. The domain size was as large as 1mm across, indicating low nucleation density in this area during the crystal growth process. To better understand the surface morphology, the ingot was examined using optical

microscopy. The crystals were highly transparent and colorless. The Fe-Cr alloy under the crystal can be seen through the transparent $h^{10}BN$ crystal layer. Micro images show that some domains overlap each other, like fish scale (Figure 5.1c). Considering that nitrogen is the only volatile element in the system, this is presumably due to the deficiency of nitrogen during $h^{10}BN$ crystal precipitation process.[60] The deficiency of nitrogen in some areas can change the domain shape on the ingot. The subgrains were relatively flat, with equilateral, non-equilateral, truncate triangle or trapezoidal shape. For $h^{10}BN$ grown from Fe flux, the main morphology of subgrains were trapezoid (Figure 5.1d).
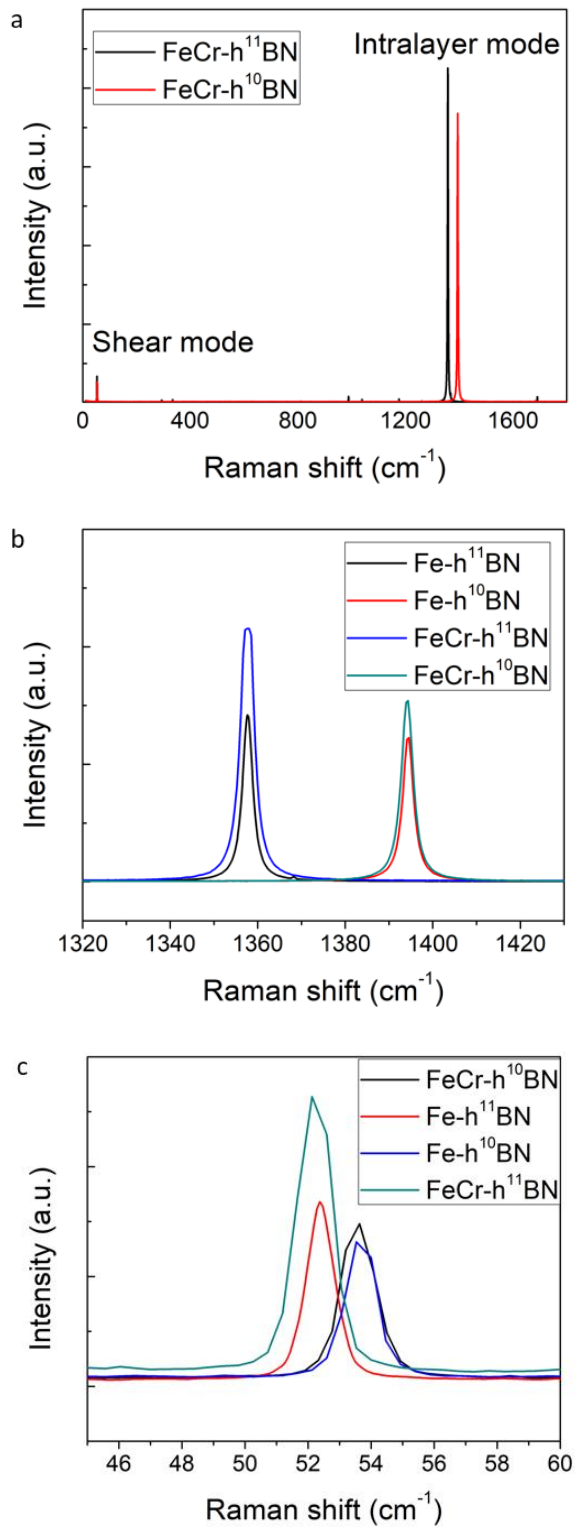
Figure 5.2 (a) Raman spectra of bulk hBN flake grown from Fe-Cr. (b) shear mode and (c) intralayer mode.

Figure 5.2 shows Raman spectra of $h^{10}BN$ and $h^{11}BN$ crystals grown from Fe and Fe-Cr flux. Both $h^{10}BN$ and $h^{11}BN$ exhibit a high frequency peak and a low frequency peak. The mode at high frequency originates from the intralayer E_{2g} phonon vibration.[152] In contrast, the mode at low frequency is attributed to a vibrational interlayer shear mode, specific to the relative motion of adjacent atomic layers. The intensity of intralayer mode is much higher than shear mode, which corresponds the interaction difference. The in-plane interactions are strong chemical bond. However, the interlayer interaction is weak van der Waals force. No other peak was detected ranging from 10 to 1800 cm^{-1}.

The peaks of intralayer mode in Fe grown and Fe-Cr grown $h^{10}BN$ are at 1394.4 cm^{-1} and 1394.1 cm^{-1}, respectively. The full width at half-maximum (FWHM) value for Fe grown and Fe-Cr grown $h^{10}BN$ are 2.9 and 3.2 cm^{-1}. Both are comparable with our Ni-Cr grown $h^{10}BN$ (3.1cm^{-1}),[59] which suggests the quality of Fe and Fe-Cr grown monoisotopic hBN is similar to our Ni-Cr grown $h^{10}B$: these monoisotopic hBN are highly crystalline. The peaks of both Fe grown and Fe-Cr grown $h^{11}BN$ are at 1357.7 cm^{-1} with a FWHM of 2.8 cm^{-1} and 3.5 cm^{-1}, respectively. These are also comparable with Ni-Cr grown $h^{11}BN$[59]. The E2g phonon energy of $h^{10}BN$ is higher than $h^{11}BN$ due to the boron atomic mass difference of ^{10}B and ^{11}B. In a harmonic oscillator, the vibration frequency of a binary atoms lattice is proportional to $\sqrt{\frac{1}{m_B} + \frac{1}{m_N}}$, where m_B and m_N are atom mass of boron and nitrogen.[63] Due to the smaller mass of ^{10}B, $h^{10}BN$ has a larger phonon energy than $h^{11}BN$. The FWHM value of both $h^{10}BN$ and $h^{11}BN$ is much smaller than natural abundant hBN (7.8 cm^{-1}), which attributed to the isotope disorder effect. Isotopic mass fluctuation interrupts the translational symmetry of isotopically pure atoms and causes elastic scattering of phonons. Therefore, monoisotopic hBN without isotopic

59

mass fluctuation has less elastic scattering of phonons. Figure 5.2c displays the low-frequency spectra in shear mode. The low frequency peak of $h^{10}BN$ grown in Fe and Fe-Cr with appears at 53.7 (FWHM of 0.9 cm^{-1}) and 53.6 (FWHM of 1.1 cm^{-1}) cm^{-1}, respectively. The peak positions of $h^{11}BN$ grown from Fe and Fe-Cr are at 52.2 and 52.4 cm^{-1}, with a FWHM 0.9 cm^{-1}, respectively. This indicates the crystals have few stacking defects. The FWHM values of both $h^{11}BN$ and $h^{10}BN$ grown from Fe and Fe-Cr flux are slightly smaller than monoisotopic hBN grown from Ni-Cr flux (1.3 cm^{-1}),[59] suggesting both $h^{11}BN$ and $h^{10}BN$ grown from Fe and Fe-Cr flux may have less stacking defects than $h^{11}BN$ and $h^{10}BN$ grown from Ni-Cr. Similar to intralayer mode, for $h^{10}BN$, a blue shift was observed to $h^{11}BN$. The phonon energy difference is also attributed to mass difference of ^{10}B and ^{11}B.
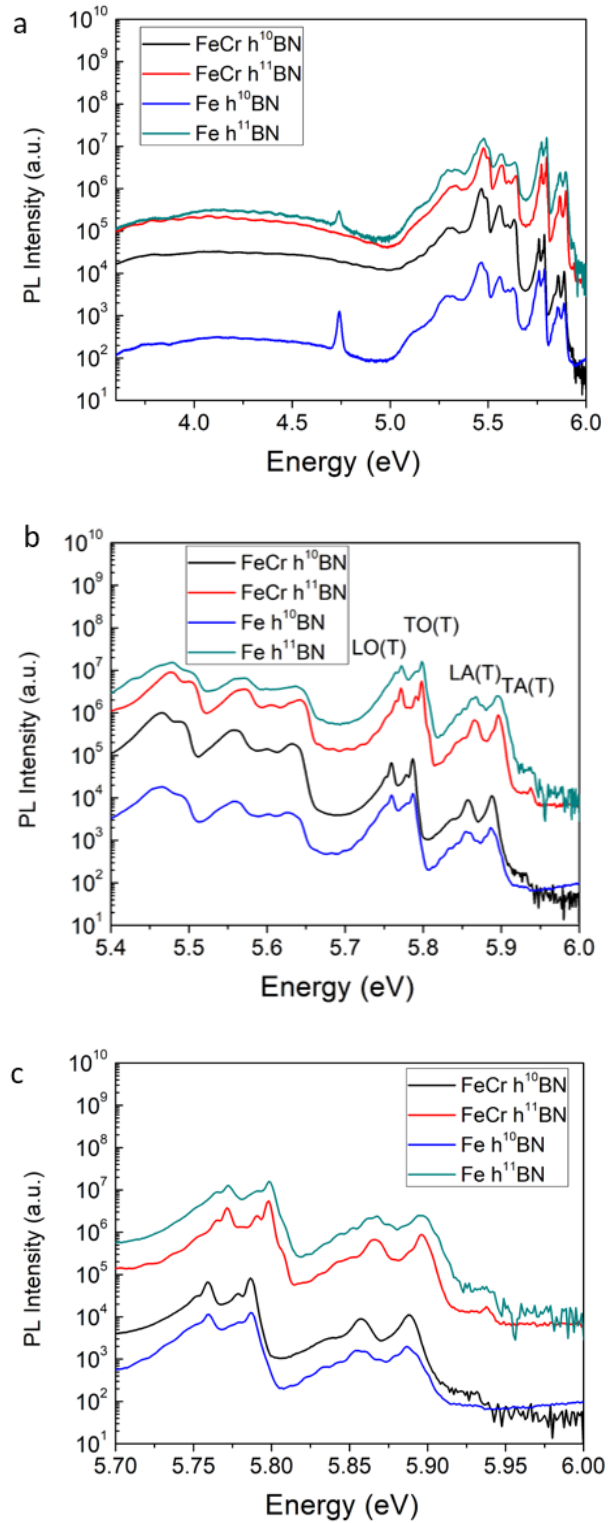
Figure 5.3 (a) Photoluminescence spectra of bulk h^{10}BN on a log scale at 8K. Left inset: zoom of the PL on a log scale. (b) PL spectra ranging from 5.0 eV to 6.0 eV. (c) PL spectra in the deep ultraviolet (ranging from 5.7 eV to 5.95 eV).

As Figure 5.3a illustrates, there were no emission peaks around 4 eV, indicating low concentration of carbon, and oxygen impurities and other points defects.[153, 154] The donor-acceptor pair line originates from boron and nitrogen divacancy centered on 5.56 and 5.3 eV.[70]

As an indirect semiconductor, the lowest energy of conduction band is located at the M point of the Brillouin zone, whereas the maximum energy of valance band sits at the K point. Due to the energy and momentum conservation, radiative recombination must be assisted by the emission of phonons.[69, 70, 120] Consequently, the PL spectra of hBN is composed of many phonon replica lines, which is attributed to the different paths of phonon emission. Figure 5.3b shows the PL spectra of monoisotopic hBN ranging from 5.0 eV to 6.0 eV. The lines around 5.62, 5.56, 5.47, 5.32 and 5.27 eV are named as D lines, which come from inter-K valley scattering assisted by phonons at the K point of the Brillouin zone. The stacking defects of bulk crystals provide density of states and make the inter-K valley scattering observable.[70] Especially, the peak at about 5.46 eV corresponds to the longitudinal optical (LO)/ transverse optical (TO) virtual excitonic state plus 2 TO phonons. The peaks at about 5.76 and 5.79 eV are caused by longitudinal optical (LO) and transverse optical (TO), respectively. The peak intensities of TO and LO at 5.75 eV becomes comparable to the peak LO/TO plus 2TO at 5.5 eV, which is a dramatic improvement over some reported hBN: the peaks of TO and LO are not visible due to the lower crystallinity than our hBN[112, 155]. The PL spectrum is globally blue shifted slightly in h^{11}BN, compared to h^{10}BN. Figure 5.3c demonstrates PL spectra of bulk h^{10}BN in the deep ultraviolet region. Phonon-assisted transition peaks are caused by longitudinal optical (LO, at 5.76 eV) and transverse optical (TO, at 5.79 eV), longitudinal acoustic (LA, at 5.86 eV) and transverse

acoustic (TA, at 5.89 eV) phonons. The presence of those sharp and intense peaks indicate the crystal have better crystallinity and less impurities and defects than many previous studies in which these peaks were not observed.[112, 139, 155]

Conclusion

In summary, we successfully synthesized monoisotopic boron hBN bulk single crystals from both Fe and Fe-Cr flux via metal flux method. Raman shear mode shows the crystals are highly ordered in the c direction, whereas the small FWHM of intralayer mode indicates highly crystalline in plane. The peak intensities of TO and LO at 5.75 eV in PL spectra are comparable to the peak LO/TO plus 2TO at 5.5 eV, demonstrating the high quality of these bulk hBN crystal. The presence of intense transition peaks assisted by LO, TO, LA and TA phonons is another strong evidence of the high quality of the crystals. Based on our results, both Fe and Fe-Cr fluxes can be used to grow high quality of bulk hBN, which reduces the cost significantly. This study opens a new way to produce high quality of monoisotopic boron hBN, which is good candidate material for fundamental isotope effect of hBN, the novel 2D material. Our hBN also bring great potential applications such as neutron detector, heat management materials in nano flexible devices, phonon polariton-based nanophotonic devices.

Experimental methods
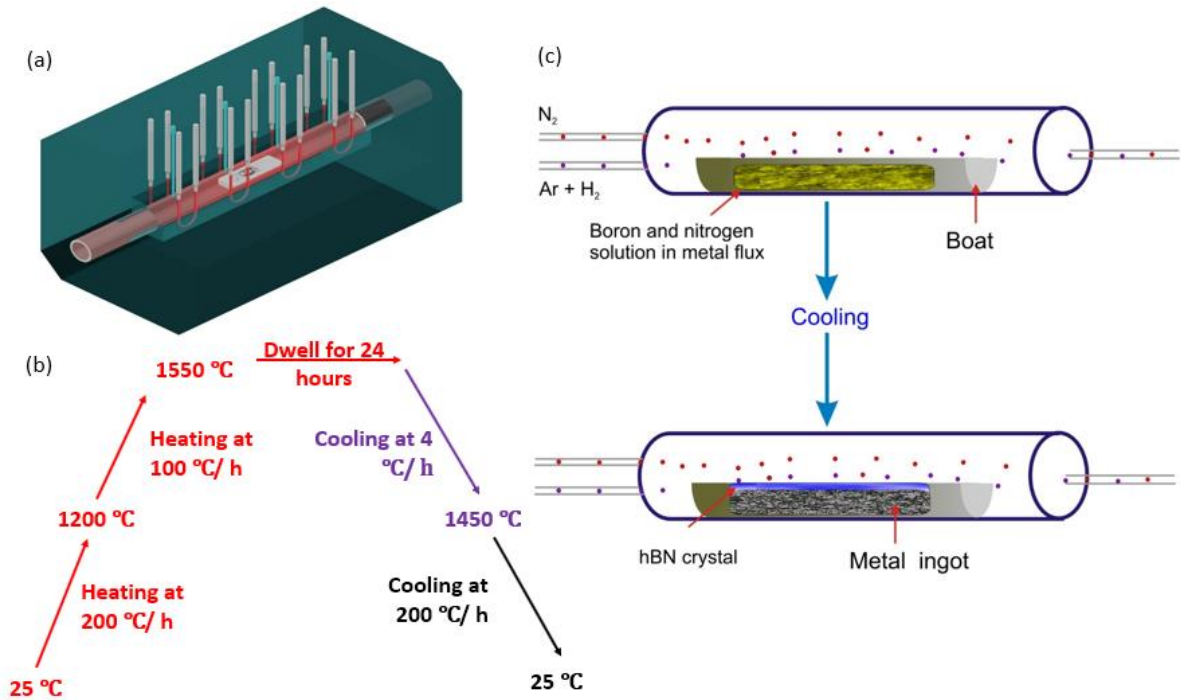
Figure 5.4 Schematic diagram illustrating the monoisotopic boron hBN crystal growth process: (a) alumina tube furnace with a single heating zone, (b) temperature versus time profile, (c) boron and nitrogen were dissolved in metal flux at high temperature(top), then hBN single crystal precipitated on the metal flux surface during cooling process (bottom).

Bulk single crystal growth. Monoisotopic boron hBN (h^{10}BN and h^{11}BN) were synthesized in the tube furnace and the crystals were grown by the metal flux method. Figure 5.4 illustrates a schematic of the process. For pure Fe grown hBN crystal, 2g ^{10}B (or ^{11}B) powders and 60g Fe were used as starting materials. For Fe-Cr metal flux, high-purity 30g iron shot, 30g chromium granules, and 2g ^{10}B or ^{11}B powders were used. The starting materials were loaded into an alumina crucible, then placed into an alumina tube furnace with single horizontal heating zone. Before heating the furnace, the alumina tube was purged three times by forming gases (95% Ar and H$_2$ 5%) and N$_2$, then was filled to a pressure of 820 torr. The flow rate of N$_2$ and forming gas were 700 and 30 sccm during the

experimental process, respectively. The alumina crucible was heated to 1550 ℃ and held for 24h. This allowed the metals to melt and the solution to saturate with boron and nitrogen. Then the crucible was cooled to 1450 ℃ at a rate of 4 ℃/h. hBN crystals precipitated during the cooling process. Finally, the furnace was quenched to room temperature at 200 ℃ /h, so the metal flux was solidified to form a metal ingot. The $h^{10}BN$ (or $h^{11}BN$) crystal covered the ingot surface.

Raman spectra. To do Raman and photoluminescence characterizations, the hBN crystals were peeled from metal flux surface using thermal release tape. Raman spectra were taken at room temperature using a Horiba Labram HR Raman microscope system. A 532 nm laser was used. The laser spot was focused by a 100x lens to a spot diameter of ~1 µm. By using an 1800 groove/mm grating, we achieved an instrument resolution of ~0.5 cm^{-1}. The Lorentz equation was used to normalize the result.

Photoluminescence spectra The opto-electronic properties of the h10BN and h11BN single crystals were characterized by PL spectroscopy. The latter were mounted on the cold finger of a closed-cycle cryostat at a temperature of 10K. The excitation beam is the fourth harmonic of a cw mode-locked Ti-Sa oscillator (194 nm) with a repetition frequency of 82 MHz. The beam was focused on the sample with a spot diameter of ~50µm and a power of ~35 µW. An achromatic optical system couples the emitted signal to the detection system using parabolic mirrors with a special coating for deep UV. The detection system was composed of a f = 300 mm Czerny-Turner monochromator, equipped with a 1800 grooves/mm grating blazed at 250 nm, and a back-illuminated CCD camera (Andor

Newton 920), with a quantum efficiency of 50% at 210 nm, operated over integration times of 1 min.

Acknowledgement

Chapter 6 - Defects engineering of monoisotopic hexagonal boron nitride single crystals via neutron irradiation

Introduction

Two-dimensional (2D) materials are of interest for their fundamental physics and potential for novel devices. [156, 157] Next to graphene, hBN is the most employed 2D material, as it enables a broad range of nanoelectronic, nanophotonic and optoelectronic devices, due to its excellent properties, including atomic flatness, and absence of charge traps and dangling bonds. The properties of hBN can be further enhanced when it contains only one boron isotope, either exclusively ^{10}B or ^{11}B, instead of the natural mixture of 20% ^{10}B and 80% ^{11}B. Monoisotopic hBN single crystals have reduced phonon scattering from isotopic disorder, which leads to a two times higher thermal conductivity[32] and three times longer phonon-polariton lifetimes.[149] However, hBN is invariably an insulator with fixed optical and electrical properties, which limits its application in electronic and optoelectronic devices.

Defect engineering of hBN single crystals offers the possibility to control the hBN's properties. By introducing point defects and impurities into highly crystalline hBN single crystals, new energy levels and charge scattering centers may be created, to manipulate the electronic and optical properties of hBN. For example, hBN is a promising matrix for bright and photostable single photon emitters. Potentially, these can be produced with a homogeneous spectral distribution by controlling the types and spatial distribution of defects.[158]

This neutron irradiation study of hBN was undertaken in an attempt to alter its properties via a far from thermodynamic equilibrium process. Neutron transmutation

doping (NTD) has the potential to produce boron vacancies and lithium doping in a way that could not be produced during crystal growth or by diffusion techniques. NTD has previously been used to produce dopants homogeneously in a controlled way in some 3D materials such as GaAs, Ge[159], Si[160], and Ge-Ga alloy.[161]

Boron isotope thermal neutron capture cross-sections are

$\sigma(^{10}B) = 3{,}890$ barns   and $\sigma(^{11}B) = 0.005$ barns.

The nuclear reactions the boron isotopes undergo are:

$^{10}B + n \rightarrow [^{11}B]^* \rightarrow {}^{4}He(1.47\ \text{MeV}) + {}^{7}Li\ (0.84\ \text{MeV}) + \gamma(0.48\ \text{MeV})$ 94%

$^{10}B + n \rightarrow [^{11}B]^* \rightarrow {}^{4}He(1.78\ \text{MeV}) + {}^{7}Li\ (1.02\ \text{MeV})$ 6%
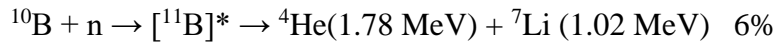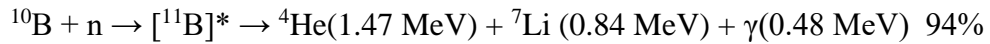
Natural nitrogen is mostly isotopes ^{14}N (99.6%) with only a trace of ^{15}N (0.4%). The ^{14}N isotope has a thermal neutron capture cross section of $\sigma(^{14}N) = 1.84$ barns, and the nuclear reaction it undergoes is

$^{14}N + n \rightarrow {}^{14}C\ (40\ \text{keV}) + {}^{1}H\ (580\ \text{keV})$

Given the high energy imparted to these elementary particles due to the nuclear reaction, there is a high probability that the lithium ion does not reside on a substitutional position. Thus, boron vacancies and lithium interstitials are expected to be present in the irradiated hBN. Other crystal lattice damage is expected as well, as the energetic particles displace additional boron and nitrogen atoms. Thus, neutron irradiation is dominated by ^{7}Li doping and boron vacancies in h^{10}BN, and is a mixture of ^{7}Li doping, boron vacancies, and ^{14}C doping in h^{11}BN because of relatively small neutron capture cross-sections. We expect that the NTD would introduce new energy states within hBN's energy band gap controllably.

Prior hBN neutron irradiation studies have employed powder and pyrolytic boron nitride (pBN, hBN with a fine grain, partially ordered structure). Kabyshev et al.[162] identified boron vacancies on neutron-irradiated pyrolytic boron nitride using electron paramagnetic resonance spectroscopy (EPR). However, Cataldo et al.[163] suggested that neutron irradiation converted hBN powder into cubic boron nitride based on results of Raman and Fourier-transform infrared spectroscopy. They also identified two paramagnetic nitrogen vacancies, based on one-boron centers and three-boron center using EPR. Toledo et al.[164] also found two paramagnetic defects in electron paramagnetic spectra and attributed them to nitrogen vacancies.

In the present study, neutron transmutation doping on monoisotopic boron hBN single crystals was undertaken in an attempt to separate the effects of radiation due to ^{10}B and ^{11}B isotopes. We report on the neutron transmutation doping of monoisotopic boron hBN single crystals (h^{10}BN (99.22 at. % ^{10}B) and h^{11}BN (99.41 at. % ^{11}B), and pyrolytic BN with the natural distribution of boron isotopes. Subsequently, the irradiated hBN were characterized by Raman, photoluminescence and electron paramagnetic resonance spectroscopy were used to characterize the defects. This not only allowed us to investigate the defects induced by neutron irradiation on single crystals separately but also to study the isotopic effects on defect engineering.

Result and discussion
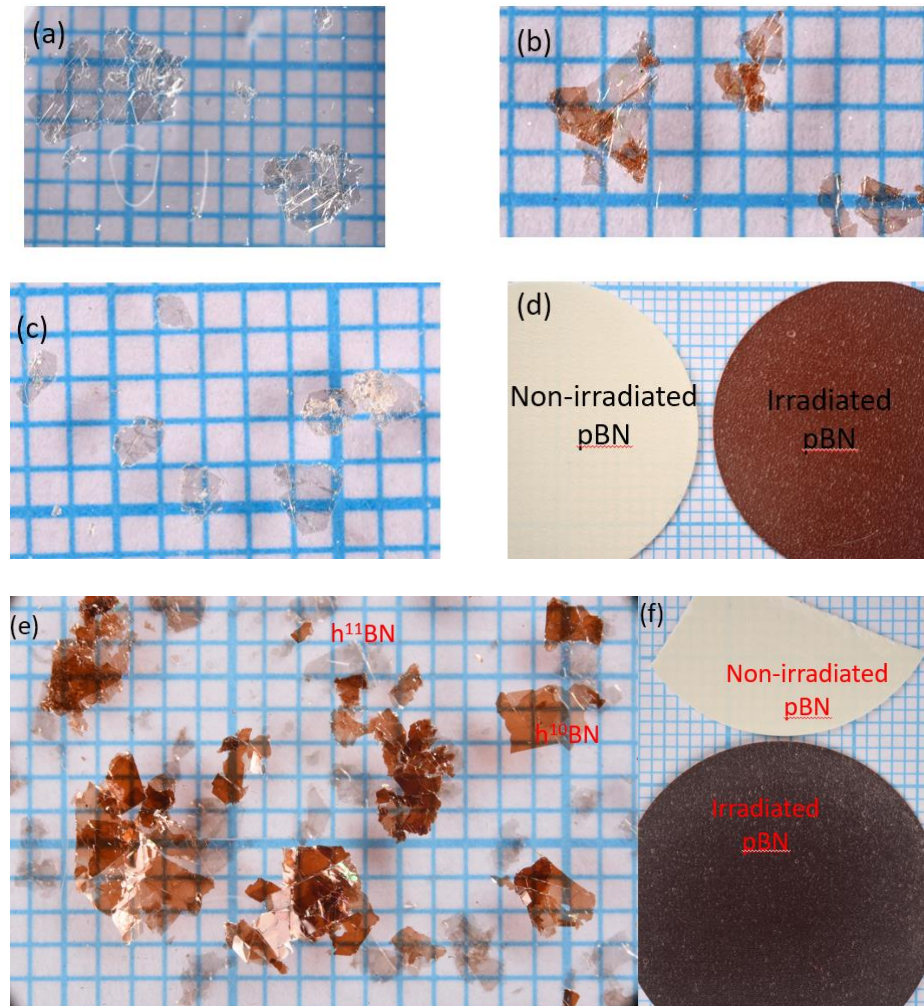
Figure 6.1. Macro images of hBN single crystal flakes and pyrolytic boron nitride (pBN). (a) As-grown $h^{10}BN$ flakes. The grid size is 1 mm. (b) $h^{10}BN$ flakes after low-dose irradiation. The neutron flux of low-dose irradiation was $2.6*10^{16}$ /cm^2. (c) $h^{11}BN$ flakes after low-dose irradiation. (d) Non-irradiated and low-dose irradiated pBN. (e) $h^{10}BN$ and $h^{11}BN$ flakes after high-dose irradiation. The dark red crystals are $h^{10}BN$ and the slightly pink crystals are $h^{11}BN$. The neutron flux of high-dose irradiation was $2.6*10^{17}$ /cm^2. (f) Non-irradiated and high irradiated pBN.

Figure 6.1 shows macro images of hBN single crystal flakes and pBN before and after irradiation. The hBN single crystal flakes were colorless and transparent before irradiation (Figure 6.1a). The color of $h^{10}BN$ changed to reddish-brown after the low-dose irradiation of $2.6*10^{16}$ neutron/cm^2 (Figure 6.1b). After high-dose irradiation $(2.6*10^{17}$

neutron/cm^2), the reddish-brown color became more intense. This indicates that neutron irradiation form color center in h^{10}BN. After irradiation, the h^{11}BN was only slightly brown. The color of pBN change from white to brown to black after low and high irradiation, respectively.
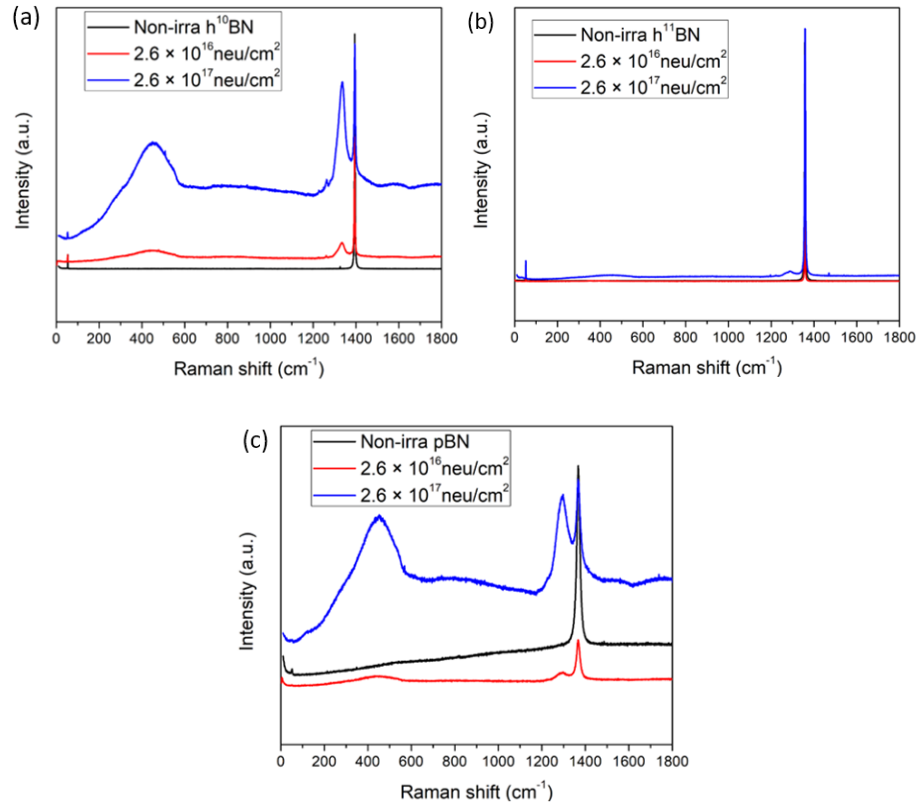
Figure 6.2. (a) Raman spectra of h^{10}BN single crystal before and after irradiation. (b) Raman spectra of h^{11}BN single crystal before and after irradiation. (c) Raman spectra of pBN before and after irradiation.

Table 6.1 Intralayer Raman mode of hBN single crystal and pBN.

FWHM of intralayer mode (cm^{-1})			
	Non-irradiated	$2.6*10^{16}$ (neutron/cm^2)	$2.6*10^{17}$ (neutron/cm^2)
$h^{10}BN$	2.96	3.34	4.82
$h^{11}BN$	3.06	3.02	4.2
pBN	17.5	19.1	22.4
Peak position (cm^{-1})			
$h^{10}BN$	1394.5	1394.0	1395.0
$h^{11}BN$	1358.2	1358.0	1358.2
pBN	1367.7	1367.2	1367.5

Figure 6.2 shows the Raman spectra of the hBN single crystals and pBN. For $h^{10}BN$, the Raman spectra changed dramatically, with new peaks appearing at 400 cm^{-1} and 1350 cm^{-1}. In contrast, these new peaks were barely evident in the $h^{11}BN$. The Raman spectra of pBN more closely resembled that of $h^{10}BN$. High-quality hBN single crystals exhibits two signature peaks: interlayer and intralayer mode. The interlayer mode is at low frequency (~53 cm^{-1}), which comes from rigid shear vibration between adjacent layers.[118] The original peaks of the intralayer vibrational mode in $h^{10}BN$, pBN and $h^{11}BN$ were at 1394.5, 1358.2 and 1367.7 cm^{-1} (Table 6.1), respectively, due to the atomic mass difference between ^{10}B and ^{11}B. Compared to pBN, the Raman peak widths for $h^{10}BN$ and $h^{11}BN$ are narrower, because they have less isotopic disorder-induced Raman scattering.[63] All of FWHM increased after neutron irradiation (Table 6.2), which indicates neutron introduced more crystal defects.

Table 6.2 Interlayer Raman mode of hBN single crystal.

	FWHM of interlayer mode (cm^{-1})		
	Non-irradiated	$2.6*10^{16}$ (neutron/cm^2)	$2.6*10^{17}$ (neutron/cm^2)
h^{10}BN	1.0	1.1	1.9
h^{11}BN	1.1	1.0	1.05
Peak position (cm^{-1})			
h^{10}BN	53.8	53	52.5
h^{11}BN	52.6	52.0	52.3

The interlayer mode peak width of the h^{10}BN increased from 1.0 to 1.9 cm^{-1} after neutron irradiation, indicating neutron bombardment produced more defects. However, the peak position and the FWHM in the h^{11}BN did not change significantly, probably because the ^{11}B capture cross section is small. pBN has no shear mode peak due to its low crystallinity.

Table 6.3 Two new peaks at Raman spectra of h^{10}BN single crystal and pBN.

	FWHM (cm^{-1})			
	Peak 1 of 1st irradiated	Peak 1 of 2nd irradiated	Peak 2 of 1st irradiated	Peak 2 of 2nd irradiated
h^{10}BN	247	255	34.5	35
pBN	190	246	78	77
Peak position (cm^{-1})				
h^{10}BN	447	451	1334	1335
pBN	450	451	1296	1295

Two broad new peaks appeared in the h^{10}BN and pBN after neutron irradiation (Table 6.3). Cataldo *et al.* also reported that the existence of a peak at 1335 cm^{-1} in neutron irradiation hBN powder which he cited as evidence for the formation of cubic boron nitride (cBN). However, cBN has two characteristic peaks: TO peak at 1048 cm^{-1} and LO peak at 1302 cm^{-1}.[165] Our results had no TO peak of cBN, thus we conclude that the formation of

cBN is unlikely. Considering Li^+ forms by neutron capture reaction, these two new peaks may come from interstitial Li^+.

The new peak may arise from the point defects produced by neutron irradiation. A point defect can induce a localized phonon mode at or in the vicinity of the point defect. The maximum phonon vibrational intensity is located at, and decays exponentially with distance from the point defect. The localized phonon mode can produce Raman satellite.[166,][167] The peak of $h^{10}BN$ was blue shifted compared to pBN. Therefore, the point defect must be related to boron atom. ^{10}B atom mass is smaller than the average for natural boron, which induces a blue shift.

The second Raman peak immerging from the irradiation of both $h^{10}BN$ and pBN was at 451 cm^{-1} with comparable FWHM. It must not be related to boron atoms, because both ^{10}B and natural boron atoms have the same peak position, i.e., it is independent of the boron atomic mass. Both $h^{10}BN$ and pBN have the same peak, suggesting neutron irradiation introduce homogenous points defects.
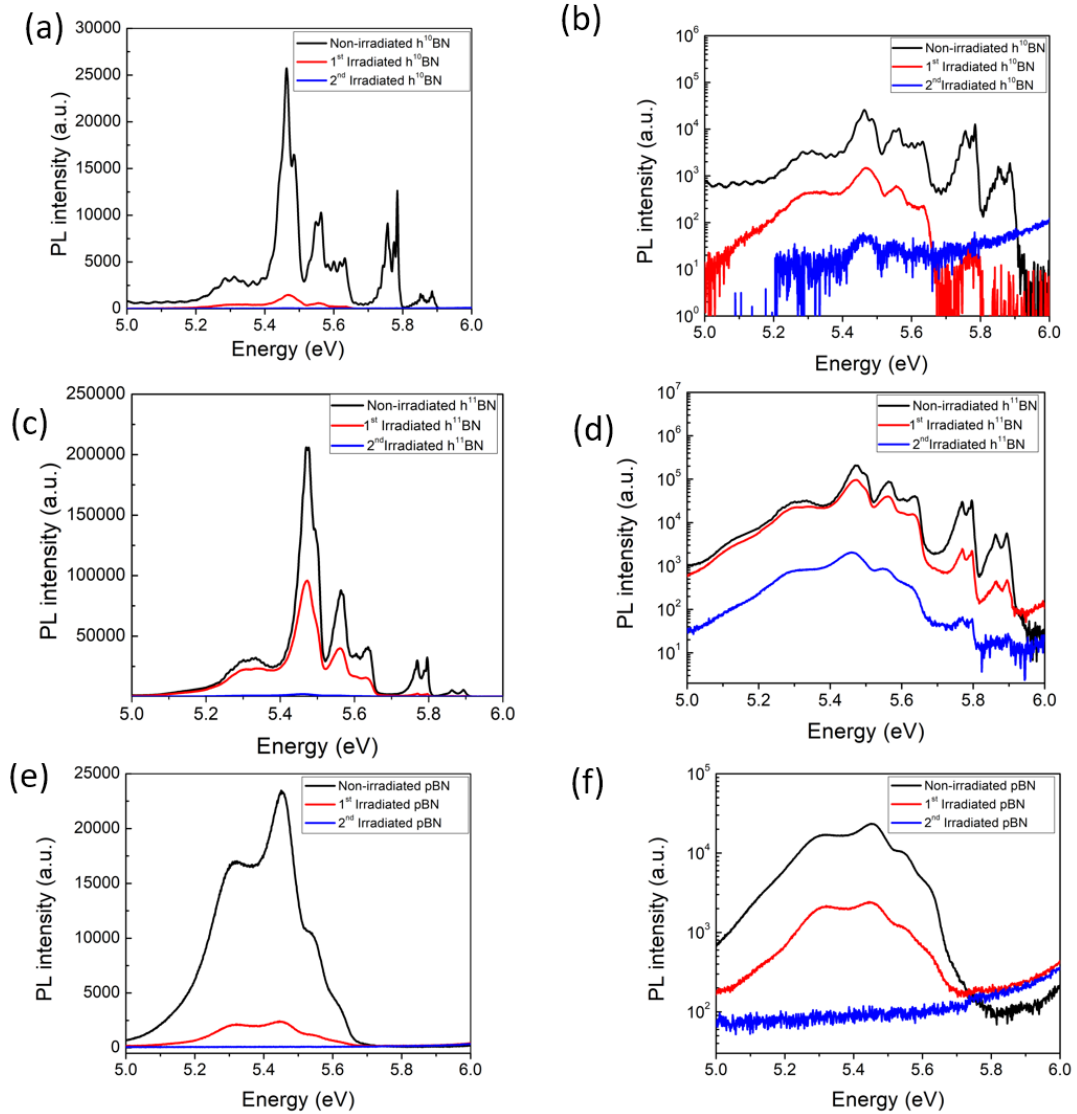
Figure 6.3 Photoluminescence spectra (PL) of hBN single crystal and pBN recorded at 8 K for energies ranging between 5 and 6 eV. (a) PL spectra of $h^{10}BN$ crystals on a linear scale. (b) PL spectra of $h^{10}BN$ crystals on a semi-logarithmic scale. (c) PL spectra of $h^{11}BN$ crystals on a linear scale. (d) PL spectra of $h^{11}BN$ crystals on a semi-logarithmic scale. (e) PL spectra of pBN crystals on a linear scale. (f) PL spectra of pBN crystals on a semi-logarithmic scale.

Figure 6.3 displays the photoluminescence spectra (PL) of the monoisotopic hBN single crystals and the pBN. As an indirect semiconductor, radiative recombination induces phonon scattering to fulfill both energy and momentum conservation.[69] Therefore, instead of strong luminescence features, the presence of phonon-assistant peaks ranging between

5.7 and 6 eV indicates highly crystalline hBN.[89] As demonstrated by the black lines in a-d, both non-irradiated $h^{10}BN$ and $h^{11}BN$ have these phonon-assistant peaks, demonstrating the high-quality of the $h^{10}BN$ and $h^{11}BN$ single crystals. In contrast, pBN does not have these peaks (Figure 6.3e and f) because it is not single crystal. The peaks ranging between 5.5-5.7 eV are due to transverse optical phonons assist intervalley scattering, which becomes observable because stacking fault defects provide a density of final electronic states.[70]

After neutron irradiation, the PL intensity for all the samples was reduced, indicating neutron irradiation can produce defect in $h^{10}BN$, $h^{11}BN$ and pBN. After the low-dose irradiation ($2.6*10^{16}$ neutron/cm^2), the phonon-assistant peaks in $h^{10}BN$ above 5.7 eV were eliminated. However, $h^{11}BN$ maintains these peaks even after the high-dose irradiation ($2.6*10^{17}$ neutron/cm^2), because $h^{11}BN$ has smaller capture cross section than $h^{10}BN$. For pBN, the broad defect-related PL peak between 5.1 and 5.5 eV was diminished but was still visible after low-dose irradiation, but disappeared completely after the high-dose irradiation.
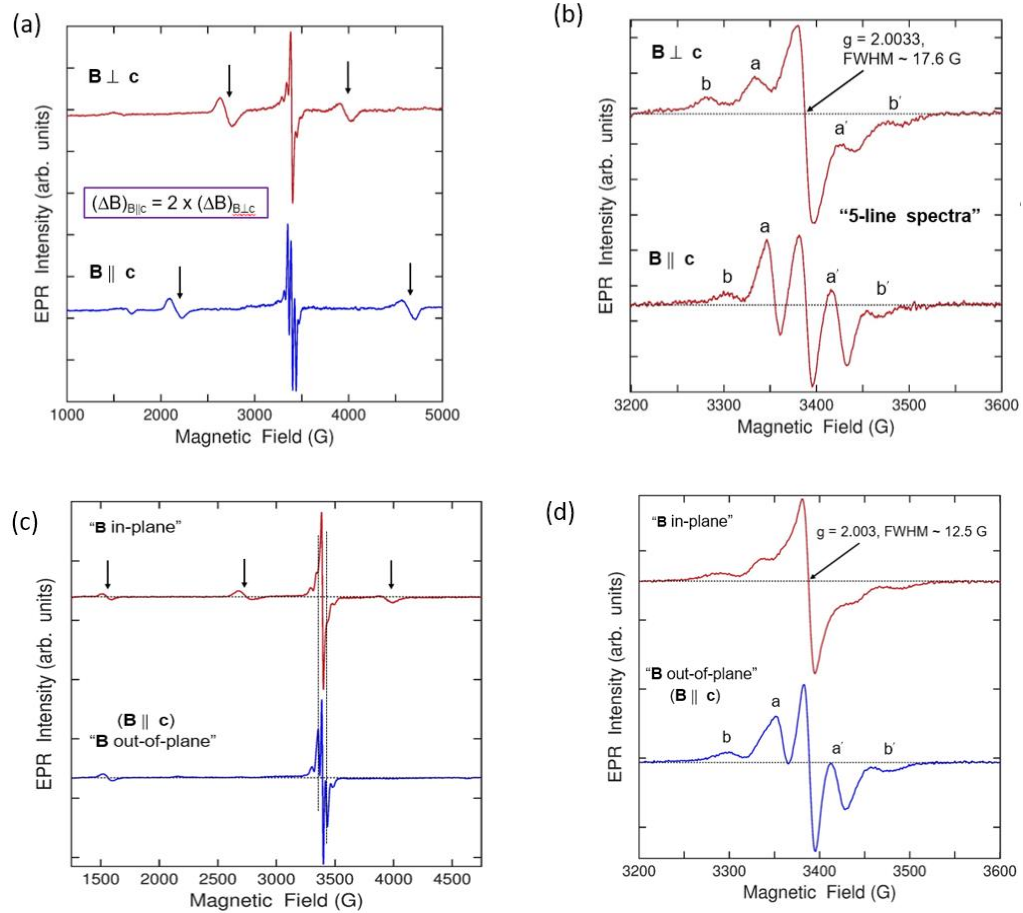
Figure 6.4 Electron paramagnetic resonance (EPR) spectra of neutron-irradiated h^{10}BN and pBN. (a) EPR of neutron-irradiated h^{10}BN flake. Vertical arrows indicate the widely split pair of lines originated from the S=1 defect. (b) The five lines spectrum of neutron-irradiated h^{10}BN flake centered about 3400 G. (c) EPR of the neutron-irradiated pBN. Vertical arrows indicate the S=1 defect. (d) the five lines spectrum of neutron-irradiated pBN centered about 3400 G. Both h^{10}BN and pBN were irradiated under 2.6 x 10^{17} neutrons/cm^2.

Figure 6.4 shows the EPR spectra of neutron-irradiated h^{10}BN and pBN. The spectra consist of two groups: the five lines spectrum centered about 3400 G (Figure 6.4b for h^{10}BN and 4d for pBN) and the widely split pair of lines that show a strong angular anisotropy (vertical arrows in Figure 6.4a and 4c). They likely originated from two defect centers.

The five lines spectrum centered about 3400 G has been attributed by many researchers to either an one boron center (OBC) or three boron center (TBC) defects in natural boron powders.[163, 164, 168, 169] They claimed that an unpaired electron localized on one or three ^{11}B atom causes the five lines. However, Kabyshev *et al.*[162] attributes this to a two-nitrogen center (TNC) defect. The h^{10}BN single crystal had the same spectrum, which indicates that the defect is not related to ^{11}B atom. Considering the large capture cross section of ^{10}B, isolated boron vacancies are the most likely dominant defect in the neutron-irradiated h^{10}BN samples. A boron-vacancy created by the neutron irradiation can trap an unpaired electron with wavefunction delocalized on two neighboring ^{14}N atoms.

The second group of EPR lines (labelled by vertical arrows in Figure 6.4a and 4c) consists of the widely split pair of lines. Kabyshev *et al.*[162] assigned these same defect (two-nitrogen center) with the five lines spectrum centered about 3400 G. However, our Raman results show that there are two types of defects in both the neutron-irradiated h^{10}BN and pBN. Also, the lines show a strong angular anisotropy (Figure 6.4a and 4c) while the peaks that make up the 5-line spectrum centered about 3400G (TNC defect) exhibit a weak angular anisotropy (Figure 6.4b and 4d). From this we believe that they originate from different defects.
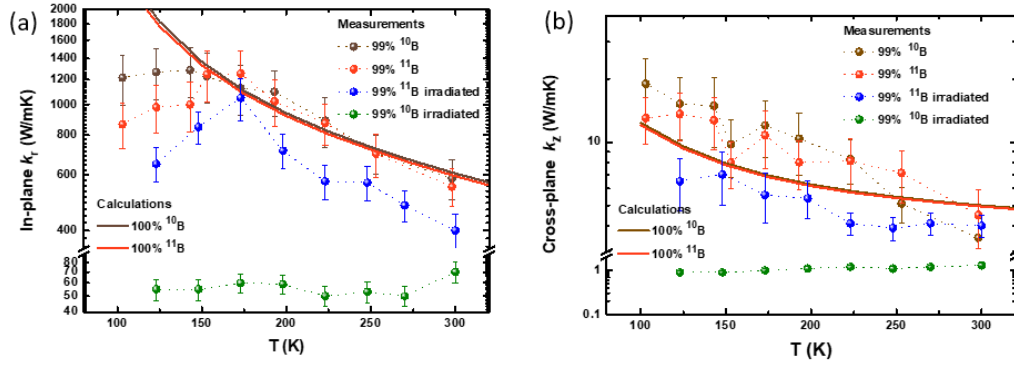
Figure 6.5 Temperature-dependent thermal conductivity of neutron-irradiated hBN flake. (a) in-plane (k_r) and (b) out-of-plane (k_z) of hBN, along with measurements on non-irradiated hBN flakes (labeled by [10]B and [11]B) [32].

Figure 6.5 shows temperature-dependent thermal conductivity of neutron-irradiated hBN flake. For neutron-irradiated h[10]BN (green dots in Figure 6.5), both the in-plane and out-of-plane thermal conductivity were significantly lower than the non-irradiated hBN at low temperature ranging between 100K and 300K. This indicates that the neutron irradiation produced many defects, which decreased the thermal conductivity by increasing phonon-phonon scattering. In contrast, for neutron-irradiated h[11]BN (blue dots in Figure 6.5), both the in-plane and out-of-plane thermal conductivity were only slightly lower than the non-irradiated hBN at low temperature ranging between 100K and 300K, which shows the neutron irradiation only damaged the crystal lattice slightly.
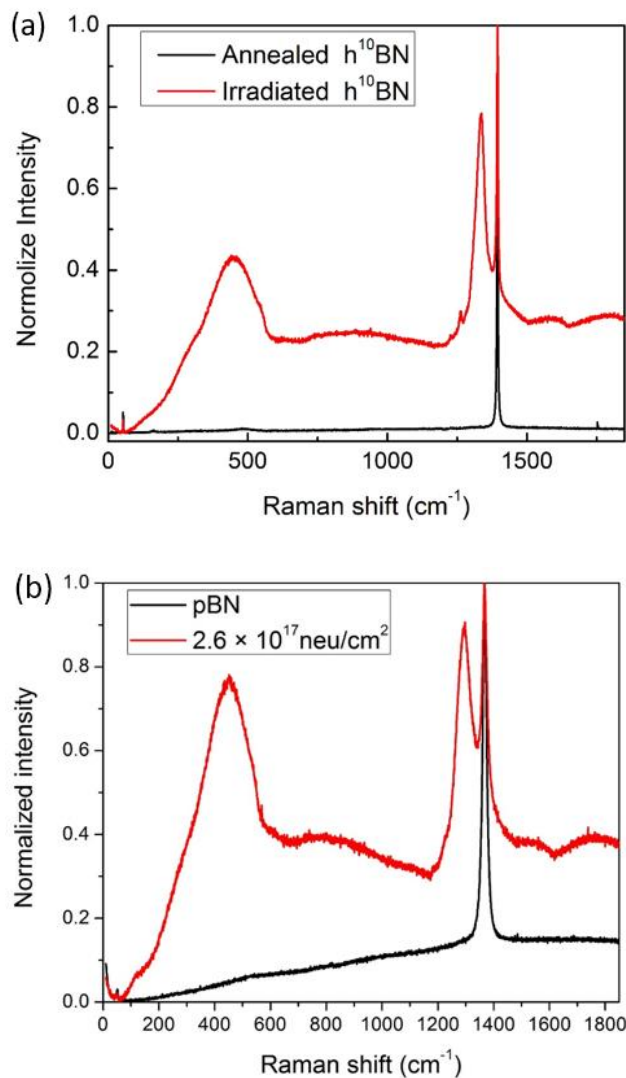
Figure 6.6 Raman spectra of h^{10}BN single crystal and pBN annealed at 1,000 ℃.

Table 6.4 Raman spectra FWHM of the E$_{2g}$ peaks for h^{10}BN single crystal and pBN before and after irradiation, then after annealing at 1,000 ℃.

	Non-irradiated	2nd irradiation	After annealing
h^{10}BN (cm^{-1})	3.06	4.2	3.6
pBN (cm^{-1})	17.0	22.4	19.3

Figure 6.6 shows Raman spectra of h^{10}BN single crystal and pBN after annealing

at 1,000 ℃. The two peaks present after irradiation disappeared upon annealing, which is

another evidence that the two peaks seen in the Raman spectra arose from point defects. The intralayer mode peak of h^{10}BN single crystal and pBN narrowed from 4.2, 22.3 cm^{-1} to 3.6, 19.3 cm^{-1}, respectively (Table 6.4). This indicates the crystallinity recovered after annealing.
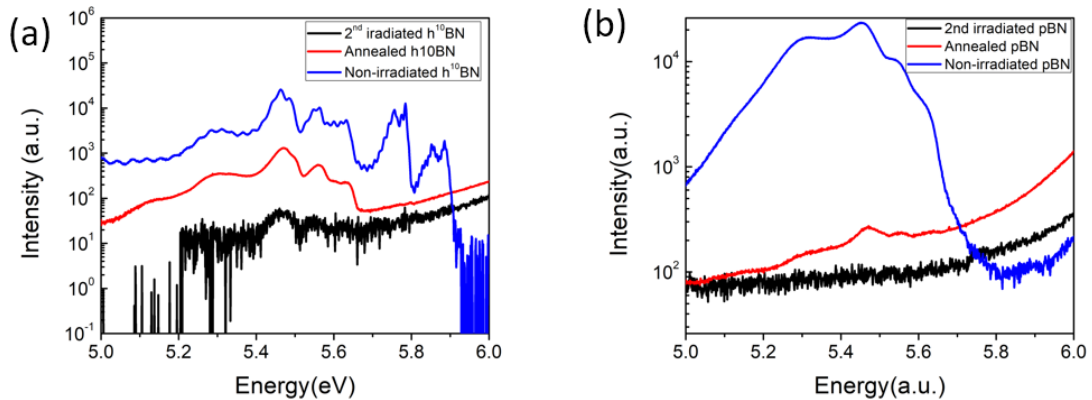
Figure 6.7. PL spectra of annealed h^{10}BN single crystal and pBN.

Figure 6.7 shows the PL spectra of the irradiated h^{10}BN single crystal and pBN after annealing at 1,000 °C. After annealing, the intervalley scattering peaks of h^{10}BN centered at 5.5 eV appear again, indicating the crystallinity was approved. However, the phonon-assistant peak ranging between 5.7 and 6 eV were not visible, suggesting the h^{10}BN crystal quality is not as good as non-irradiated h^{10}BN. For pBN, the intervalley scattering peaks were also observable after annealing.

Conclusion

In this study, monoisotopic boron hBN single crystals (h^{10}BN (99.22 at. %) and h^{11}BN (99.41 at. %), and pyrolytic BN were irradiated under neutron flux. Raman spectra

show that two different types of point defects were produced. PL spectra demonstrate that the crystallinity was slightly impacted. EPR spectra of $h^{10}BN$ flake reveal that the lines centered originated from boron vacancy, instead of one or three ^{11}B atom center. Our results demonstrate that defects engineering of monoisotopic hexagonal boron nitride single crystals have been achieved via neutron irradiation.

Experimental methods

$h^{10}BN$ and $h^{11}BN$ crystal growth. The monoisotopic hexagonal boron nitride crystals were grown from a Ni-Cr flux.[59] The starting materials, 2g ^{10}B (or ^{11}B), 24g Ni and 24g Cr powders were mixed in an alumina and heated at 1550 °C for 24h under flowing N_2 and H_2, then were cooled down to 1525 °C at a cooling rate of 0.5°C/h，which allowed the crystal precipitation. The flowing rate of the N_2 and H_2 was 125 and 5 sccm, respectively. The system was cooled down to room temperature at a cooling rate 200 °C/h. Free-standing hBN single crystal was peeled from the metal ingot surface using thermal release tape to produce free-standing hBN flakes.

Neutron irradiation. An irradiating neutron fluence was calculated by multiplying neutron flux with time. The irradiation was at 300 kW of reactor power, at which power the thermal neutron flux is $3*10^{12}$ n/cm^2/s. Thus, the thermal neutron fluence of the first and second irradiation delivered was $2.6*10^{16}$ and $2.6*10^{17}$ n/cm^2, respectively. The neutron irradiations of the first and second irradiation included a 57 and 570 Mrad and dose gamma ray, respectively.

The lithium concentration was calculated as the product of the average neutron flux, the absorption cross section, and the irradiation time.

For the $h^{10}BN$ flakes, using a 1-D, monoenergetic neutrons model, the average flux within the sample was estimated by integrating the exponentially decreasing flux over the sample thickness and dividing by the total thickness. (1) For a sample thickness of 10 microns, the average flux over the sample is 90% of the unperturbed flux. After 24.1 hours of irradiation, the lithium concentration is $4.8*10^{19}$ atoms per cc (fraction of B-10 atoms converted = 0.090%). (2) For a sample thickness of 100 microns, the average flux over the sample is 43% of the unperturbed flux. After 24.1 hours of irradiation, the lithium concentration is $2.3*10^{19}$ atoms $/cm^{-3}$ (fraction of B-10 atoms converted is 0.043%).

The thickness of pyrolytic BN was 250 microns, which results in an average flux of $1.9*10^{12}$ neutron/cm^2. Therefore, the lithium concentration at the end of the long irradiation is $6.5*10^{18}$ $/cm^{-3}$.

For the $h^{11}BN$ flakes, the very small amount of B-10 does not depress the flux at all. The starting concentration of B-10 in the sample is $3.0*10^{20}$ $/cm^{-3}$, and the irradiation was designed to convert 0.1% of the B-10 atoms, so the lithium concentration at the end of the irradiation is $3.0*10^{17}$ $/cm^{-3}$.

Raman spectra. Raman spectra were taken at room temperature using a Horiba Labram HR Raman microscope system. A 532 nm laser was used. The laser spot was focused by a 100x lens to a spot diameter of ~1 μm. By using an 1800 groove/mm grating, we achieved an instrument resolution f ~0.5 cm^{-1}. Lorentz equation was used to normalize the result.

Photoluminescence spectra. The optical properties of our samples were characterized by PL spectroscopy. The hBN crystals were held on the cold finger of a closed-cycle cryostat at a temperature of 10K. The excitation beam is the fourth harmonic

of a cw mode-locked Ti-Sa oscillator (194 nm) with a repetition frequency of 82 MHz. The beam was focused on the sample with a spot diameter of ~50μm and a power of ~35 μW. An achromatic optical system couples the emitted signal to our detection system using parabolic mirrors with a special coating for deep UV. The detection system was composed of a f = 300 mm Czerny-Turner monochromator, equipped with a 1800 grooves/mm grating blazed at 250 nm, and a back-illuminated CCD camera (Andor Newton 920), with a quantum efficiency of 50% at 210 nm, operated over integration times of 1 min.

Annealing. Neutron-irradiated $h^{10}BN$ and pBN were loaded in an alumina crucible. The crucible was heat at 1000 ℃ for 1h under flowing N_2 and forming gas (5% H_2 and 95% Ar), then were cooled down to room temperature at a cooling rate of 200℃/h. The flowing rate of the N_2 and forming gas was 125 and 5 sccm, respectively.

Acknowledgement

Chapter 7 - Conclusion and Recommendations

Large-area and low-defect bulk hBN single crystal was grown for iron flux. Iron solvent is inexpensive and available in higher purities (lower carbon concentrations) than chromium or nickel. The hBN size was 300 times larger than the hBN grown from nickel-chromium or iron-chromium fluxes what has been previously reported. Raman and photoluminescence revealed that the crystals were highly crystalline. A graphene/hBN/graphene tunneling device shows that the dielectric breakdown strength is 14 MV/cm, which is 4 times than reported result. The crystals are ideal insulating layer for 2D devices. The hBN has potential to fabricate high performance devices and investigate thermal, optical and electrical properties of hBN.

hBN crystals were also grown via temperature gradient method with an iron-chromium flux. This method produced larger crystals. Raman and photoluminescence demonstrated that the crystals were high-quality. High in-plane and out-of-plane thermal conductivity confirmed that the hBN flake had few defects.

Monoisotopic boron hBN single crystals from both Fe and Fe-Cr flux. These were both new solvents that had not previously been used with pure boron source of boron-10 and boron-11. Raman and photoluminescence spectroscopy showed that the crystal quality grown from both Fe and Fe-Cr fluxes were comparable.

Defect engineering of hBN single crystals was achieved by introducing point defects and impurities. EPR spectra of $h^{10}BN$ flake reveal that the lines centered originated from boron vacancy, instead of one or three boron-11 atom center. Raman and

photoluminescence spectroscopy showed that the crystallinity of h^{11}BN was slightly impacted.

Based on these findings, there are a few recommendations on how to further improve hBN growth by metal flux. Because the best-quality natural hBN was grown from iron flux, iron has potential to grow the best quality monoisotopic boron hBN single crystals by reacting nitrogen with pure boron source of boron-10 and boron-11. Growth parameters such as dwell temperature, cooling rate and cooling temperature range, nitrogen flow rate can be tested to improve the crystal quality. Additionally, quantitative characterization for carbon and oxygen (less than few ppm) is needed for the future study. Finally, the larger area hBN grown from iron make more potential applications such as hydrogen isotope separation, which is impossible for the small-area hBN grown from nickel-chromium or iron-chromium.

References

(1) Sajjad, M., Morell, G.; Feng, P. Advance in novel boron nitride nanosheets to nanoelectronic device applications. *ACS applied materials & interfaces* **2013,** *5,* 5051.

(2) Wang, J. I., Yang, Y., Chen, Y., Watanabe, K., Taniguchi, T., Churchill, H. O.; Jarillo-Herrero, P. Electronic transport of encapsulated graphene and WSe$_2$ devices fabricated by pick-up of prepatterned hBN. *Nano letters* **2015,** *15,* 1898.

(3) Dai, S., Tymchenko, M., Yang, Y., Ma, Q., Pita-Vidal, M., Watanabe, K., Taniguchi, T., Jarillo-Herrero, P., Fogler, M. M.; Alù, A. Manipulation and steering of hyperbolic surface polaritons in hexagonal boron nitride. *Advanced materials* **2018,** *30,* 1706358.

(4) Li, L. H., Chen, Y., Lin, M., Glushenkov, A. M., Cheng, B.; Yu, J. Single deep ultraviolet light emission from boron nitride nanotube film. *Applied physics letters* **2010,** *97,* 141104.

(5) Clark, G., Schaibley, J. R., Ross, J., Taniguchi, T., Watanabe, K., Hendrickson, J. R., Mou, S., Yao, W.; Xu, X. Single defect light-emitting diode in a van der Waals heterostructure. *Nano letters* **2016,** *16,* 3944.

(6) Martínez, L., Pelini, T., Waselowski, V., Maze, J., Gil, B., Cassabois, G.; Jacques, V. Efficient single photon emission from a high-purity hexagonal boron nitride crystal. *Physical review B* **2016,** *94,* 121405.

(7) Diguna, L. J., Tjahjana, L., Darma, Y., Zeng, S., Wang, H.; Birowosuto, M. D. Light-matter interaction of single quantum emitters with dielectric nanostructures. *Photonics* **2018,** *5,* 14.

(8) Choi, D., Poudel, N., Park, S., Akinwande, D., Cronin, S. B., Watanabe, K., Taniguchi, T., Yao, Z.; Shi, L. Large reduction of hot spot temperature in graphene electronic devices with heat-spreading hexagonal boron nitride. *ACS applied materials & interfaces* **2018,** *10,* 11101.

(9) Jacob, Z. Nanophotonics: hyperbolic phonon–polaritons. *Nature materials* **2014,** *13,* 1081.

(10) Kumar, A., Low, T., Fung, K. H., Avouris, P.; Fang, N. X. Tunable light-matter interaction and the role of hyperbolicity in graphene–hBN system. *Nano letters* **2015,** *15,* 3172.

(11) Shiue, R., Efetov, D. K., Grosso, G., Peng, C., Fong, K. C.; Englund, D. Active 2D materials for on-chip nanophotonics and quantum optics. *Nanophotonics* **2017,** *6,* 1329.

(12) Liu, C., Zheng, J., Chen, Y., Fryett, T.; Majumdar, A. Van der Waals materials integrated nanophotonic devices. *Optical materials express* **2019,** *9,* 384.

(13) Hoffman, T., Zhang, Y., Edgar, J.; Gaskill, D. Growth of hBN using metallic boron: isotopically enriched h^{10}BN and h^{11}BN. *MRS online proceedings library archive* **2014,** *1635,* 35.

(14) Blase, X., Rubio, A., Louie, S.; Cohen, M. Stability and band gap constancy of boron nitride nanotubes. *Europhysics letters* **1994,** *28,* 335.

(15) Zheng, J., Zhang, L., Kretinin, A. V., Morozov, S. V., Wang, Y. B., Wang, T., Li, X., Ren, F., Zhang, J.; Lu, C. High thermal conductivity of hexagonal boron nitride laminates. *2D materials* **2016,** *3,* 011004.

(16) Martin, J., Le Mogne, T., Chassagnette, C.; Gardos, M. N. Friction of hexagonal boron nitride in various environments. *Tribology transactions* **1992,** *35,* 462.

(17) Coan, T., Barroso, G. S., Motz, G., Bolzán, A.; Machado, R. A. F. Preparation of PMMA/hBN composite coatings for metal surface protection. *Materials research* **2013,** *16,* 1366.

(18) Kim, K. K., Kim, S. M.; Lee, Y. H. A new horizon for hexagonal boron nitride film. *Journal of the Korean physical society* **2014,** *64,* 1605.

(19) Kubota, Y., Watanabe, K., Tsuda, O.; Taniguchi, T. Deep ultraviolet light-emitting hexagonal boron nitride synthesized at atmospheric pressure. *Science* **2007,** *317,* 932.

(20) Dean, C., Young, A., Wang, L., Meric, I., Lee, G., Watanabe, K., Taniguchi, T., Shepard, K., Kim, P.; Hone, J. Graphene based heterostructures. *Solid state communications* **2012,** *152,* 1275.

(21) Wang, H., Taychatanapat, T., Hsu, A., Watanabe, K., Taniguchi, T., Jarillo-Herrero, P.; Palacios, T. BN/graphene/BN transistors for RF applications. *IEEE electron device letters* **2011,** *32,* 1209.

(22) Fiori, G., Bruzzone, S.; Iannaccone, G. Very large current modulation in vertical heterostructure graphene/hBN transistors. *IEEE transactions on electron devices* **2012,** *60,* 268.

(23) Kang, S., Prasad, N., Movva, H. C., Rai, A., Kim, K., Mou, X., Taniguchi, T., Watanabe, K., Register, L. F.; Tutuc, E. Effects of electrode layer band structure on the performance of multilayer graphene-hBN-graphene interlayer tunnel field effect transistors. *Nano letters* **2016,** *16,* 4975.

(24) Doan, T., Majety, S., Grenadier, S., Li, J., Lin, J.; Jiang, H. Fabrication and characterization of solid-state thermal neutron detectors based on hexagonal boron nitride epilayers. *Nuclear instruments and methods in physics research section a: accelerators, spectrometers, detectors and associated equipment* **2014,** *748,* 84.

(25) Zobelli, A., Ewels, C., Gloter, A., Seifert, G., Stephan, O., Csillag, S.; Colliex, C. Defective structure of BN nanotubes: from single vacancies to dislocation lines. *Nano letters* **2006,** *6,* 1955.

(26) Nishiwaki, A., Oku, T.; Narita, I. Formation and atomic structures of boron nitride nanohorns. *Science and technology of advanced materials* **2004,** *5,* 629.

(27) Wu, H., Fan, X.; Kuo, J. Metal free hydrogenation reaction on carbon doped boron nitride fullerene: a DFT study on the kinetic issue. *Journal of hydrogen energy* **2012,** *37,* 14336.

(28) Narita, I., Oku, T., Tokoro, H.; Suganuma, K. Synthesis and structures of iron nanoparticles coated with boron nitride nanomaterials. *Microscopy* **2006,** *55,* 123.

(29) Hod, O. Quantifying the stacking registry matching in layered materials. *Israel journal of chemistry* **2010,** *50,* 506.

(30) Chandni, U., Watanabe, K., Taniguchi, T.; Eisenstein, J. Evidence for defect-mediated tunneling in hexagonal boron nitride-based junctions. *Nano letters* **2015,** *15,* 7329.

(31) Kim, S. M., Hsu, A., Park, M. H., Chae, S. H., Yun, S. J., Lee, J. S., Cho, D., Fang, W., Lee, C.; Palacios, T. Synthesis of large-area multilayer hexagonal boron nitride for high material performance. *Nature communications* **2015,** *6,* 8662.

(32) Yuan, C., Li, J., Lindsay, L., Cherns, D., Pomeroy, J. W., Liu, S., Edgar, J. H.; Kuball, M. Modulating the thermal conductivity in hexagonal boron nitride via controlled boron isotope concentration. *Communications physics* **2019,** *2,* 43.

(33) Kostoglou, N., Polychronopoulou, K.; Rebholz, C. Thermal and chemical stability of hexagonal boron nitride (h-BN) nanoplatelets. *Vacuum* **2015,** *112,* 42.

(34) Caldwell, J. D., Aharonovich, I., Cassabois, G., Edgar, J. H., Gil, B.; Basov, D. Photonics with hexagonal boron nitride. *Nature* **2019,** *41578,* 019.

(35) Zhao, B.; Zhang, Z. M. Resonance perfect absorption by exciting hyperbolic phonon polaritons in 1D hBN gratings. *Optics express* **2017,** *25,* 7791.

(36) Dai, S., Quan, J., Hu, G., Qiu, C., Tao, T. H., Li, X.; Alù, A. Hyperbolic phonon polaritons in suspended hexagonal boron nitride. *Nano letters* **2018,** *19,* 1009.

(37) Liu, Z., Gong, Y., Zhou, W., Ma, L., Yu, J., Idrobo, J. C., Jung, J., MacDonald, A. H., Vajtai, R.; Lou, J. Ultrathin high-temperature oxidation-resistant coatings of hexagonal boron nitride. *Nature communications* **2013,** *4,* 1.

(38) Li, J., Majety, S., Dahal, R., Zhao, W., Lin, J.; Jiang, H. Dielectric strength, optical absorption, and deep ultraviolet detectors of hexagonal boron nitride epilayers. *Applied physics letters* **2012,** *101,* 171112.

(39) Watanabe, K., Taniguchi, T., Niiyama, T., Miya, K.; Taniguchi, M. Far-ultraviolet plane-emission handheld device based on hexagonal boron nitride. *Nature photonics* **2009,** *3,* 591.

(40) Kim, K. K., Hsu, A., Jia, X., Kim, S. M., Shi, Y., Dresselhaus, M., Palacios, T.; Kong, J. Synthesis and characterization of hexagonal boron nitride film as a dielectric layer for graphene devices. *ACS nano* **2012,** *6,* 8583.

(41) Duan, J., Wang, X., Lai, X., Li, G., Watanabe, K., Taniguchi, T., Zebarjadi, M.; Andrei, E. Y. High thermoelectricpower factor in graphene/hBN devices. *Proceedings of the National Academy of Sciences of the United States of America* **2016,** *113,* 14272.

(42) Hajian, H., Ghobadi, A., Butun, B.; Ozbay, E. Nearly perfect resonant absorption and coherent thermal emission by hBN-based photonic crystals. *Optics express* **2017,** *25,* 31970.

(43) Xue, J., Sanchez-Yamagishi, J., Bulmash, D., Jacquod, P., Deshpande, A., Watanabe, K., Taniguchi, T., Jarillo-Herrero, P.; LeRoy, B. J. Scanning tunnelling microscopy and spectroscopy of ultra-flat graphene on hexagonal boron nitride. *Nature materials* **2011,** *10,* 282.

(44) Wang, L., Meric, I., Huang, P. Y., Gao, Q., Gao, Y., Tran, H., Taniguchi, T., Watanabe, K., Campos, L. M., Muller, D. A., Guo, J., Kim, P., Hone, J., Shepard, K. L.; Dean, C. R. One-dimensional electrical contact to a two-dimensional material. *Science* **2013,** *342,* 614.

(45) Dorgan, V. E., Bae, M.; Pop, E. Mobility and saturation velocity in graphene on SiO_2. *Applied physics letters* **2010,** *97,* 082112.

(46) Tran, T. T., Zachreson, C., Berhane, A. M., Bray, K., Sandstrom, R. G., Li, L. H., Taniguchi, T., Watanabe, K., Aharonovich, I.; Toth, M. Quantum emission from defects in single-crystalline hexagonal boron nitride. *Physical review applied* **2016,** *5,* 034005.

(47) Proscia, N. V., Shotan, Z., Jayakumar, H., Reddy, P., Cohen, C., Dollar, M., Alkauskas, A., Doherty, M., Meriles, C. A.; Menon, V. M. Near-deterministic activation of room-temperature quantum emitters in hexagonal boron nitride. *Optica* **2018,** *5,* 1128.

(48) Aharonovich, I.; Toth, M. Quantum emitters in two dimensions. *Science* **2017,** *358,* 170.

(49) Ahmed, K., Dahal, R., Weltz, A., Lu, J., Danon, Y.; Bhat, I. Growth of hexagonal boron nitride on (111) Si for deep UV photonics and thermal neutron detection. *Applied physics letters* **2016,** *109,* 113501.

(50) Li, J., Dahal, R., Majety, S., Lin, J.; Jiang, H. Hexagonal boron nitride epitaxial layers as neutron detector materials. *Nuclear instruments and methods in physics research section a: accelerators, spectrometers, detectors and associated equipment* **2011,** *654,* 417.

(51) Kim, S. M., Hsu, A., Araujo, P., Lee, Y., Palacios, T., Dresselhaus, M., Idrobo, J., Kim, K. K.; Kong, J. Synthesis of patched or stacked graphene and hBN flakes: a route to hybrid structure discovery. *Nano letters* **2013,** *13,* 933.

(52) Lee, C., Rathi, S., Khan, M. A., Lim, D., Kim, Y., Yun, S. J., Youn, D., Watanabe, K., Taniguchi, T.; Kim, G. Comparison of trapped charges and hysteresis behavior in hBN encapsulated single MoS_2 flake based field effect transistors on SiO_2 and hBN substrates. *Nanotechnology* **2018,** *29,* 335202.

(53) Cong, C., Zou, C., Cao, B., Wu, L., Shang, J., Wang, H., Qiu, Z., Hu, L., Tian, P.; Liu, R. Intrinsic excitonic emission and valley Zeeman splitting in epitaxial MS_2 (M= Mo and W) monolayers on hexagonal boron nitride. *Nano research* **2018,** *11,* 6227.

(54) Wang, X., Hossain, M., Wei, Z.; Xie, L. Growth of two-dimensional materials on hexagonal boron nitride (h-BN). *Nanotechnology* **2018,** *30,* 034003.

(55) Kleiner, M. B., Kuhn, S. A.; Weber, W. Thermal conductivity measurements of thin silicon dioxide films in integrated circuits. *IEEE transactions on electron devices* **1996,** *43,* 1602.

(56) Zhang, X., Choudhury, T. H., Chubarov, M., Xiang, Y., Jariwala, B., Zhang, F., Alem, N., Wang, G., Robinson, J. A.; Redwing, J. M. Diffusion-controlled epitaxy of large area coalesced WSe_2 monolayers on sapphire. *Nano letters* **2018,** *18,* 1049.

(57) Wang, Y., Xu, L., Yang, Z., Xie, H., Jiang, P., Dai, J., Luo, W., Yao, Y., Hitz, E.; Yang, R. High temperature thermal management with boron nitride nanosheets. *Nanoscale* **2018,** *10,* 167.

(58) Ji, Y., Calderon, B., Han, Y., Cueva, P., Jungwirth, N. R., Alsalman, H. A., Hwang, J., Fuchs, G. D., Muller, D. A.; Spencer, M. G. Chemical vapor deposition growth of large single-crystal mono-, bi-, tri-layer hexagonal boron nitride and their interlayer stacking. *ACS nano* **2017,** *11,* 12057.

(59) Liu, S., He, R., Xue, L., Li, J., Liu, B.; Edgar, J. H. Single crystal growth of millimeter-sized monoisotopic hexagonal boron nitride. *Chemistry of materials* **2018,** *30,* 6222.

(60) Stehle, Y., Meyer III, H. M., Unocic, R. R., Kidder, M., Polizos, G., Datskos, P. G., Jackson, R., Smirnov, S. N.; Vlassiouk, I. V. Synthesis of hexagonal boron nitride monolayer: control of nucleation and crystal morphology. *Chemistry of materials* **2015,** *27,* 8041.

(61) Song, L., Ci, L., Lu, H., Sorokin, P. B., Jin, C., Ni, J., Kvashnin, A. G., Kvashnin, D. G., Lou, J.; Yakobson, B. I. Large scale growth and characterization of atomic hexagonal boron nitride layers. *Nano letters* **2010,** *10,* 3209.

(62) Dahal, R., Ahmed, K., Wu, J. W., Weltz, A., Lu, J. J., Danon, Y.; Bhat, I. B. Anisotropic charge carrier transport in free-standing hexagonal boron nitride thin films. *Applied physics express* **2016,** *9,* 065801.

(63) Cardona, M.; Thewalt, M. Isotope effects on the optical spectra of semiconductors. *Reviews of modern physics* **2005,** *77,* 1173.

(64) Kiowski, O., Lebedkin, S., Hennrich, F.; Kappes, M. M. Single-walled carbon nanotubes show stable emission and simple photoluminescence spectra with weak excitation sidebands at cryogenic temperatures. *Physical review B* **2007,** *76,* 075422.

(65) Valenta, J., Juhasz, R.; Linnros, J. Photoluminescence spectroscopy of single silicon quantum dots. *Applied physics letters* **2002,** *80,* 1070.

(66) Yoshikawa, M., Kunzer, M., Wagner, J., Obloh, H., Schlotter, P., Schmidt, R., Herres, N.; Kaufmann, U. Band-gap renormalization and band filling in Si-doped GaN films studied by photoluminescence spectroscopy. *Journal of applied physics* **1999,** *86,* 4400.

(67) Vanheusden, K., Seager, C., Warren, W. T., Tallant, D.; Voigt, J. Correlation between photoluminescence and oxygen vacancies in ZnO phosphors. *Applied physics letters* **1996,** *68,* 403.

(68) Okada, M., Sawazaki, T., Watanabe, K., Taniguch, T., Hibino, H., Shinohara, H.; Kitaura, R. Direct chemical vapor deposition growth of WS_2 atomic layers on hexagonal boron nitride. *ACS nano* **2014,** *8,* 8273.

(69) Cassabois, G., Valvin, P.; Gil, B. Hexagonal boron nitride is an indirect bandgap semiconductor. *Nature photonics* **2016,** *10,* 262.

(70) Cassabois, G., Valvin, P.; Gil, B. Intervalley scattering in hexagonal boron nitride. *Physical review B* **2016,** *93,* 035207.

(71) Cao, X., Clubine, B., Edgar, J., Lin, J.; Jiang, H. Two-dimensional excitons in three-dimensional hexagonal boron nitride. *Applied physics letters* **2013,** *103,* 191106.

(72) Vuong, T., Cassabois, G., Valvin, P., Ouerghi, A., Chassagneux, Y., Voisin, C.; Gil, B. Phonon-photon mapping in a color center in hexagonal boron nitride. *Physical review letters* **2016,** *117,* 097402.

(73) Coudurier, N., Chubarov, M., Boichot, R., Mercier, F., Blanquet, E., Reboud, R., Lay, S., Crisci, A., Coindeau, S., Encinas, T.; Pons, M. Growth of boron nitride films on w-AlN (0001), 4° off-cut 4H-SiC (0001), W (110) and Cr (110) substrates by chemical vapor deposition. *Crystal research and technology* **2016,** *51,* 231.

(74) Auwärter, W., Kreutz, T., Greber, T.; Osterwalder, J. XPD and STM investigation of hexagonal boron nitride on Ni (111). *Surface science* **1999,** *429,* 229.

(75) Auwärter, W., Suter, H. U., Sachdev, H.; Greber, T. Synthesis of one monolayer of hexagonal boron nitride on Ni (111) from B-trichloroborazine(ClBNH)₃. *Chemistry of materials* **2004,** *16,* 343.

(76) Goriachko, A., He, Y., Knapp, M., Over, H., Corso, M., Brugger, T., Berner, S., Osterwalder, J.; Greber, T. Self-assembly of a hexagonal boron nitride nanomesh on Ru (0001). *Langmuir* **2007,** *23,* 2928.

(77) Joshi, S., Ecija, D., Koitz, R., Iannuzzi, M., Seitsonen, A. P., Hutter, J., Sachdev, H., Vijayaraghavan, S., Bischoff, F.; Seufert, K. Boron nitride on Cu (111): an electronically corrugated monolayer. *Nano letters* **2012,** *12,* 5821.

(78) Preobrajenski, A., Vinogradov, A.; Mårtensson, N. Monolayer of h-BN chemisorbed on Cu (1 1 1) and Ni (1 1 1): The role of the transition metal 3d states. *Surface science* **2005,** *582,* 21.

(79) Müller, F., Hüfner, S., Sachdev, H., Laskowski, R., Blaha, P.; Schwarz, K. Epitaxial growth of hexagonal boron nitride on Ag (111). *Physical review B* **2010,** *82,* 113406.

(80) Chugh, D., Wong-Leung, J., Li, L., Lysevych, M., Tan, H. H.; Jagadish, C. Flow modulation epitaxy of hexagonal boron nitride. *2D materials* **2018,** *5,* 045018.

(81) Vangala, S., Siegel, G., Prusnick, T.; Snure, M. Wafer scale BN on sapphire substrates for improved graphene transport. *Scientific reports* **2018,** *8,* 8842.

(82) Sun, J., Lu, C., Song, Y., Ji, Q., Song, X., Li, Q., Zhang, Y., Zhang, L., Kong, J.; Liu, Z. Recent progress in the tailored growth of two-dimensional hexagonal boron nitride via chemical vapour deposition. *Chemical society reviews* **2018,** *47,* 4242.

(83) Lee, J. S., Choi, S. H., Yun, S. J., Kim, Y. I., Boandoh, S., Park, J. H., Shin, B. G., Ko, H., Lee, S. H., Kim, Y. M., Lee, Y. H., Kim, K. K.; Kim, S. M. Wafer-scale single-crystal hexagonal boron nitride film via self-collimated grain formation. *Science* **2018,** *362,* 817.

(84) Wang, L., Xu, X., Zhang, L., Qiao, R., Wu, M., Wang, Z., Zhang, S., Liang, J., Zhang, Z.; Zhang, Z. Epitaxial growth of a 100-square-centimetre single-crystal hexagonal boron nitride monolayer on copper. *Nature* **2019,** *570,* 91.

(85) Liu, J., Kutty, R. G.; Liu, Z. Controlled synthesis of atomically layered hexagonal boron nitride via chemical vapor deposition. *Molecules* **2016,** *21,* 1636.

(86) Maity, A., Doan, T., Li, J., Lin, J.; Jiang, H. Realization of highly efficient hexagonal boron nitride neutron detectors. *Applied physics letters* **2016,** *109,* 072101.

(87) Henry, A., Chubarov, M., Czigány, Z., Garbrecht, M.; Högberg, H. Early stages of growth and crystal structure evolution of boron nitride thin films. *Japanese journal of applied physics* **2016,** *55,* 05FD06.

(88) Cho, Y., Summerfield, A., Davies, A., Cheng, T. S., Smith, E. F., Mellor, C. J., Khlobystov, A. N., Foxon, C. T., Eaves, L.; Beton, P. H. Hexagonal boron nitride tunnel barriers grown on graphite by high temperature molecular beam epitaxy. *Scientific reports* **2016,** *6,* 34474.

(89) Vuong, T., Cassabois, G., Valvin, P., Rousseau, E., Summerfield, A., Mellor, C., Cho, Y., Cheng, T., Albar, J. D.; Eaves, L. Deep ultraviolet emission in hexagonal boron nitride grown by high-temperature molecular beam epitaxy. *2D materials* **2017,** *4,* 021023.

(90) Laleyan, D. A., Mengle, K., Zhao, S., Wang, Y., Kioupakis, E.; Mi, Z. Effect of growth temperature on the structural and optical properties of few-layer hexagonal boron nitride by molecular beam epitaxy. *Optics express* **2018,** *26,* 23031.

(91) Wang, H., Zhang, X., Liu, H., Yin, Z., Meng, J., Xia, J., Meng, X., Wu, J.; You, J. Synthesis of large-sized single-crystal hexagonal boron nitride domains on nickel foils by ion beam sputtering deposition. *Advanced materials* **2015,** *27,* 8109.

(92) Wang, H., Zhang, X., Meng, J., Yin, Z., Liu, X., Zhao, Y.; Zhang, L. Controlled growth of few-layer hexagonal boron nitride on copper foils using ion beam sputtering deposition. *Small* **2015,** *11,* 1542.

(93) Park, K., Lee, D., Kim, K.; Moon, D. Observation of a hexagonal BN surface layer on the cubic BN film grown by dual ion beam sputter deposition. *Applied physics letters* **1997,** *70,* 315.

(94) Bugaris, D. E.; Loye, H. Materials discovery by flux crystal growth: quaternary and higher order oxides. *Angewandte chemie international edition* **2012,** *51,* 3780.

(95) Hoffman, T. B., Clubine, B., Zhang, Y., Snow, K.; Edgar, J. H. Optimization of Ni-Cr flux growth for hexagonal boron nitride single crystals. *Journal of crystal growth* **2014,** *393,* 114.

(96) Liu, S., He, R., Ye, Z., Du, X., Lin, J., Jiang, H., Liu, B.; Edgar, J. H. Large-scale growth of high-quality hexagonal boron nitride crystals at atmospheric pressure from an Fe-Cr flux. *Crystal growth & design* **2017,** *17,* 4932.

(97) Zhigadlo, N. Crystal growth of hexagonal boron nitride (hBN) from Mg-B-N solvent system under high pressure. *Journal of crystal growth* **2014,** *402,* 308.

(98) Taniguchi, T.; Watanabe, K. Synthesis of high-purity boron nitride single crystals under high pressure by using Ba-BN solvent. *Journal of crystal growth* **2007,** *303,* 525.

(99) Dean, C. R., Young, A. F., Meric, I., Lee, C., Wang, L., Sorgenfrei, S., Watanabe, K., Taniguchi, T., Kim, P.; Shepard, K. L. Boron nitride substrates for high-quality graphene electronics. *Nature nanotechnology* **2010,** *5,* 722.

(100) Lee, G., Yu, Y., Lee, C., Dean, C., Shepard, K. L., Kim, P.; Hone, J. Electron tunneling through atomically flat and ultrathin hexagonal boron nitride. *Applied physics letters* **2011,** *99,* 243114.

(101) Gurram, M., Omar, S., Zihlmann, S., Makk, P., Schönenberger, C.; Van Wees, B. Spin transport in fully hexagonal boron nitride encapsulated graphene. *Physical review B* **2016,** *93,* 115441.

(102) Akinwande, D., Petrone, N.; Hone, J. Two-dimensional flexible nanoelectronics. *Nature communications* **2014,** *5,* 5678.

(103) Caldwell, J. D., Kretinin, A. V., Chen, Y., Giannini, V., Fogler, M. M., Francescato, Y., Ellis, C. T., Tischler, J. G., Woods, C. R.; Giles, A. J. Sub-diffractional volume-confined polaritons in the natural hyperbolic material hexagonal boron nitride. *Nature communications* **2014,** *5,* 5221.

(104) Wang, J., Yao, Q., Huang, C., Zou, X., Liao, L., Chen, S., Fan, Z., Zhang, K., Wu, W.; Xiao, X. High mobility MoS_2 transistor with low schottky barrier contact by using atomic thick h-BN as a tunneling layer. *Advanced materials* **2016,** *28,* 8302.

(105) Solozhenko, V. L., Turkevich, V. Z.; Holzapfel, W. B. Refined phase diagram of boron nitride. *The Journal of physical chemistry B* **1999,** *103,* 2903.

(106) Lu, G., Wu, T., Yuan, Q., Wang, H., Wang, H., Ding, F., Xie, X.; Jiang, M. Synthesis of large single-crystal hexagonal boron nitride grains on Cu–Ni alloy. *Nature communications* **2015,** *6,* 1.

(107) Tay, R. Y., Griep, M. H., Mallick, G., Tsang, S. H., Singh, R. S., Tumlin, T., Teo, E. H. T.; Karna, S. P. Growth of large single-crystalline two-dimensional boron nitride hexagons on electropolished copper. *Nano letters* **2014,** *14,* 839.

(108) Wang, L., Wu, B., Chen, J., Liu, H., Hu, P.; Liu, Y. Monolayer hexagonal boron nitride films with large domain size and clean interface for enhancing the mobility of graphene-based field-effect transistors. *Advanced materials* **2014,** *26,* 1559.

(109) Ohta, J.; Fujioka, H. Sputter synthesis of wafer-scale hexagonal boron nitride films via interface segregation. *APL materials* **2017,** *5,* 076107.

(110) Rasool, H. I., Ophus, C.; Zettl, A. Atomic defects in two dimensional materials. *Advanced materials* **2015,** *27,* 5771.

(111) Cretu, O., Lin, Y.; Suenaga, K. Evidence for active atomic defects in monolayer hexagonal boron nitride: a new mechanism of plasticity in two-dimensional materials. *Nano letters* **2014,** *14,* 1064.

(112) Majety, S., Cao, X., Li, J., Dahal, R., Lin, J.; Jiang, H. Band-edge transitions in hexagonal boron nitride epilayers. *Applied physics letters* **2012,** *101,* 051110.

(113) Dahal, R., Li, J., Majety, S., Pantha, B., Cao, X., Lin, J.; Jiang, H. Epitaxially grown semiconducting hexagonal boron nitride as a deep ultraviolet photonic material. *Applied physics letters* **2011,** *98,* 211110.

(114) Fisk, Z.; Remeika, J. Growth of single crystals from molten metal fluxes. *Handbook on the Physics and chemistry of rare earths* **1989,** *12,* 53.

(115) Yano, M., Yap, Y. K., Okamoto, M., Onda, M., Yoshimura, M., Mori, Y.; Sasaki, T. Na: a new flux for growing hexagonal boron nitride crystals at low temperature. *Japanese journal of applied physics* **2000,** *39,* L300.

(116) Kubota, Y., Watanabe, K.; Taniguchi, T. Synthesis of cubic and hexagonal boron nitrides by using Ni solvent under high pressure. *Japanese journal of applied physics* **2007,** *46,* 311.

(117) Ahmed, K., Dahal, R., Weltz, A., Lu, J. J., Danon, Y.; Bhat, I. B. Effects of sapphire nitridation and growth temperature on the epitaxial growth of hexagonal boron nitride on sapphire. *Materials research express* **2017,** *4,* 015007.

(118) Stenger, I., Schue, L., Boukhicha, M., Berini, B., Placais, B., Loiseau, A.; Barjon, J. Low frequency Raman spectroscopy of few-atomic-layer thick hBN crystals. *2D materials* **2017,** *4,* 031003.

(119) Bourrellier, R., Amato, M., Galvão Tizei, L. H., Giorgetti, C., Gloter, A., Heggie, M. I., March, K., Stéphan, O., Reining, L.; Kociak, M. Nanometric resolved luminescence in h-BN flakes: excitons and stacking order. *ACS photonics* **2014,** *1,* 857.

(120) Vuong, T., Cassabois, G., Valvin, P., Jacques, V., Cuscó, R., Artús, L.; Gil, B. Overtones of interlayer shear modes in the phonon-assisted emission spectrum of hexagonal boron nitride. *Physical review B* **2017,** *95,* 045207.

(121) Lv, R., Robinson, J. A., Schaak, R. E., Sun, D., Sun, Y., Mallouk, T. E.; Terrones, M. Transition metal dichalcogenides and beyond: synthesis, properties, and applications of single-and few-layer nanosheets. *Accounts of chemical research* **2014,** *48,* 56.

(122) Robert, C., Amand, T., Cadiz, F., Lagarde, D., Courtade, E., Manca, M., Taniguchi, T., Watanabe, K., Urbaszek, B.; Marie, X. Fine structure and lifetime of dark excitons in transition metal dichalcogenide monolayers. *Physical review B* **2017,** *96,* 155423.

(123) Zhang, X., Zhang, F., Wang, Y., Schulman, D. S., Zhang, T., Bansal, A., Alem, N., Das, S., Crespi, V. H.; Terrones, M. Defect-controlled nucleation and orientation of WSe$_2$ on hBN–a route to single crystal epitaxial monolayers. *ACS nano* **2019,**

(124) Zhang, F., Wang, Y., Erb, C., Wang, K., Moradifar, P., Crespi, V. H.; Alem, N. Full orientation control of epitaxial MoS$_2$ on hBN assisted by substrate defects. *Physical review B* **2019,** *99,* 155430.

(125) Yu, H., Yang, Z., Du, L., Zhang, J., Shi, J., Chen, W., Chen, P., Liao, M., Zhao, J.; Meng, J. Precisely Aligned Monolayer MoS$_2$ epitaxially grown on h-BN basal plane. *Small* **2017,** *13,* 1603005.

(126) Hsu, C. C.; Sah, C. T. Generation-annealing of oxide and interface traps at 150 and 298 K in oxidized silicon stressed by Fowler-Nordheim electron tunneling. *Solid-State electronics* **1988,** *31,* 1003.

(127) Forbes, R. G., Deane, J. H., Hamid, N.; Sim, H. S. Extraction of emission area from Fowler–Nordheim plots. *Journal of vacuum science & technology B: microelectronics and nanometer structures processing, measurement, and phenomena* **2004,** *22,* 1222.

(128) Mohammad, S. N., Kub, F. J.; Eddy Jr, C. R. Field-plate design for edge termination in silicon carbide high-power Schottky diodes. *Journal of vacuum science &*

technology b, nanotechnology and microelectronics: materials, processing, measurement, and phenomena **2011,** *29,* 021021.

(129) Castellanos-Gomez, A., Buscema, M., Molenaar, R., Singh, V., Janssen, L., Van der Zant, H. S. J.; Steele, G. A. Deterministic transfer of two-dimensional materials by all-dry viscoelastic stamping. *2D materials* **2014,** *1,* 011002.

(130) Cai, Q., Scullion, D., Gan, W., Falin, A., Zhang, S., Watanabe, K., Taniguchi, T., Chen, Y., Santos, E. J.; Li, L. H. High thermal conductivity of high-quality monolayer boron nitride and its thermal expansion. *Science advances* **2019,** *5,* eaav0129.

(131) Zhang, Z., Hu, S., Chen, J.; Li, B. Hexagonal boron nitride: a promising substrate for graphene with high heat dissipation. *Nanotechnology* **2017,** *28,* 225704.

(132) Wang, S., Wang, J., Zhao, W., Giustiniano, F., Chu, L., Verzhbitskiy, I., Zhou Yong, J.; Eda, G. Efficient carrier-to-exciton conversion in field emission tunnel diodes based on MIS-type van der Waals heterostack. *Nano letters* **2017,** *17,* 5156.

(133) Dai, S., Tymchenko, M., Yang, Y., Ma, Q., Pita-Vidal, M., Watanabe, K., Taniguchi, T., Jarillo-Herrero, P., Fogler, M. M.; Alù, A. Manipulation and steering of hyperbolic surface polaritons in hexagonal boron nitride. *Advanced materials* **2018,** *30,* 1706358.

(134) Li, P., Dolado, I., Alfaro-Mozaz, F., Nikitin, A. Y., Casanova, F., Hueso, L., Vélez, S.; Hillenbrand, R. Optical nanoimaging of hyperbolic surface polaritons at the edges of van der Waals materials. *Nano letters* **2016,** *17,* 228.

(135) Nguyen, M., Kim, S., Tran, T. T., Xu, Z., Kianinia, M., Toth, M.; Aharonovich, I. Nanoassembly of quantum emitters in hexagonal boron nitride and gold nanospheres. *Nanoscale* **2018,** *10,* 2267.

(136) Maity, A., Grenadier, S., Li, J., Lin, J.; Jiang, H. Toward achieving flexible and high sensitivity hexagonal boron nitride neutron detectors. *Applied physics letters* **2017,** *111,* 033507.

(137) Lozada-Hidalgo, M., Hu, S., Marshall, O., Mishchenko, A., Grigorenko, A. N., Dryfe, R. A., Radha, B., Grigorieva, I. V.; Geim, A. K. Sieving hydrogen isotopes through two-dimensional crystals. *Science* **2016,** *351,* 68.

(138) Vuong, T., Liu, S., Van der Lee, A., Cuscó, R., Artús, L., Michel, T., Valvin, P., Edgar, J., Cassabois, G.; Gil, B. Isotope engineering of van der Waals interactions in hexagonal boron nitride. *Nature materials* **2018,** *17,* 152.

(139) Li, J., Cao, X., Hoffman, T. B., Edgar, J. H., Lin, J.; Jiang, H. Nature of exciton transitions in hexagonal boron nitride. *Applied physics letters* **2016,** *108,* 122101.

(140) Zhang, C., Zhao, S., Jin, C., Koh, A. L., Zhou, Y., Xu, W., Li, Q., Xiong, Q., Peng, H.; Liu, Z. Direct growth of large-area graphene and boron nitride heterostructures by a co-segregation method. *Nature communications* **2015,** *6,* 6519.

(141) Lindsay, L., Broido, D.; Reinecke, T. Phonon-isotope scattering and thermal conductivity in materials with a large isotope effect: A first-principles study. *Physical review B* **2013,** *88,* 144306.

(142) Sichel, E., Miller, R., Abrahams, M.; Buiocchi, C. Heat capacity and thermal conductivity of hexagonal pyrolytic boron nitride. *Physical review B* **1976,** *13,* 4607.

(143) Jiang, P., Qian, X., Yang, R.; Lindsay, L. Anisotropic thermal transport in bulk hexagonal boron nitride. *Physical review materials* **2018,** *2,* 064005.

(144) Heilmann, M., Bashouti, M., Riechert, H.; Lopes, J. Defect mediated van der Waals epitaxy of hexagonal boron nitride on graphene. *2D Materials* **2018,** *5,* 025004.

(145) Schell, A. W., Svedendahl, M.; Quidant, R. Quantum emitters in hexagonal boron nitride have spectrally tunable quantum efficiency. *Advanced materials* **2018,** *30,* 1704237.

(146) Movva, H. C., Rai, A., Kang, S., Kim, K., Fallahazad, B., Taniguchi, T., Watanabe, K., Tutuc, E.; Banerjee, S. K. High-mobility holes in dual-gated WSe_2 field-effect transistors. *ACS nano* **2015,** *9,* 10402.

(147) Robertson, B., Adenwalla, S., Harken, A., Welsch, P., Brand, J. I., Dowben, P. A.; Claassen, J. A class of boron-rich solid-state neutron detectors. *Applied physics letters* **2002,** *80,* 3644.

(148) Kuthala, N., Vankayala, R., Li, Y., Chiang, C.; Hwang, K. C. Engineering novel targeted boron-10-enriched theranostic nanomedicine to combat against murine brain tumors via MR imaging‐guided boron neutron capture therapy. *Advanced materials* **2017,** *29,* 1700850.

(149) Giles, A. J., Dai, S., Vurgaftman, I., Hoffman, T., Liu, S., Lindsay, L., Ellis, C. T., Assefa, N., Chatzakis, I.; Reinecke, T. L. Ultralow-loss polaritons in isotopically pure boron nitride. *Nature materials* **2018,** *17,* 134.

(150) Canfield, P. C.; Fisk, Z. Growth of single crystals from metallic fluxes. *Philosophical magazine B* **1992,** *65,* 1117.

(151) Fountain, R.; Chipman, J. Solubility and precipitation of boron nitride in iron-boron alloys. *Transactions of the metallurgical society of AIME* **1962,** *224,* 599.

(152) Kuzuba, T., Era, K., Ishii, T.; Sato, T. A low frequency Raman-active vibration of hexagonal boron nitride. *Solid state communications* **1978,** *25,* 863.

(153) Museur, L., Feldbach, E.; Kanaev, A. Defect-related photoluminescence of hexagonal boron nitride. *Physical review B* **2008,** *78,* 155204.

(154) Silly, M., Jaffrennou, P., Barjon, J., Lauret, J., Ducastelle, F., Loiseau, A., Obraztsova, E., Attal-Tretout, B.; Rosencher, E. Luminescence properties of hexagonal boron nitride: cathodoluminescence and photoluminescence spectroscopy measurements. *Physical review B* **2007,** *75,* 085205.

(155) Vuong, T., Cassabois, G., Valvin, P., Jacques, V., Van der Lee, A., Zobelli, A., Watanabe, K., Taniguchi, T.; Gil, B. Phonon symmetries in hexagonal boron nitride probed by incoherent light emission. *2D materials* **2016,** *4,* 011004.

(156) Cao, Y., Fatemi, V., Fang, S., Watanabe, K., Taniguchi, T., Kaxiras, E.; Jarillo-Herrero, P. Unconventional superconductivity in magic-angle graphene superlattices. *Nature* **2018,** *556,* 43.

(157) Gibertini, M., Koperski, M., Morpurgo, A.; Novoselov, K. Magnetic 2D materials and heterostructures. *Nature nanotechnology* **2019,** *14,* 408.

(158) Grosso, G., Moon, H., Lienhard, B., Ali, S., Efetov, D. K., Furchi, M. M., Jarillo-Herrero, P., Ford, M. J., Aharonovich, I.; Englund, D. Tunable and high-purity room temperature single-photon emission from atomic defects in hexagonal boron nitride. *Nature communications* **2017,** *8,* 705.

(159) Itoh, K. M., Haller, E., Hansen, W., Beeman, J., Farmer, J., Rudnev, A., Tikhomirov, A.; Ozhogin, V. Neutron transmutation doping of isotopically engineered Ge. *Applied physics letters* **1994,** *64,* 2121.

(160) Seager, C.; Castner, T. Zero-bias resistance of grain boundaries in neutron-transmutation-doped polycrystalline silicon. *Journal of applied physics* **1978,** *49,* 3879.

(161) Itoh, K. M., Haller, E., Beeman, J., Hansen, W., Emes, J., Reichertz, L., Kreysa, E., Shutt, T., Cummings, A.; Stockwell, W. Hopping conduction and metal-insulator transition in isotopically enriched neutron-transmutation-doped 70 Ge: Ga. *Physical review letters* **1996,** *77,* 4058.

(162) Kabyshev, A. V., Kezkalo, V., Lopatin, V., Serikov, L., Surov, Y. P.; Shiyan, L. N. Postradiation defects in neutron-irradiated pyrolytic boron nitride. *Physica status solidi (A) applied research* **1991,** *126,* 07.1991.

(163) Cataldo, F.; Iglesias-Groth, S. Neutron damage of hexagonal boron nitride: h-BN. *Journal of radioanalytical and nuclear chemistry* **2017,** *313,* 261.

(164) Toledo, J., De Jesus, D., Kianinia, M., Leal, A., Fantini, C., Cury, L., Sáfar, G., Aharonovich, I.; Krambrock, K. Electron paramagnetic resonance signature of point defects in neutron-irradiated hexagonal boron nitride. *Physical review B* **2018,** *98,* 155203.

(165) Zhang, W.; Matsumoto, S. Investigations of crystallinity and residual stress of cubic boron nitride films by Raman spectroscopy. *Physical review B* **2001,** *63,* 073201.

(166) Polishchuk, I. Y., Maksimov, L.; Burin, A. Localization and propagation of phonons in crystals with heavy impurities. *Physics reports* **1997,** *288,* 205.

(167) Gaur, S., Vetelino, J.; Mitra, S. Localized mode frequency for substitutional impurities in zinc blende type crystals. *Journal of physics and chemistry of solids* **1971,** *32,* 2737.

(168) Katzir, A., Suss, J., Zunger, A.; Halperin, A. Point defects in hexagonal boron nitride. I. EPR, thermoluminescence, and thermally-stimulated-current measurements. *Physical review B* **1975,** *11,* 2370.

(169) Andrei, E., Katzir, A.; Suss, J. Point defects in hexagonal boron nitride. III. EPR in electron-irradiated BN. *Physical review B* **1976,** *13,* 2831.